

Numerical Simulations of Metal-Oxides

Numerische Simulationen von Metalloxiden

Von der Fakultät für Mathematik und Physik der
Universität Stuttgart zur Erlangung der Würde eines Doktors der
Naturwissenschaften (Dr. rer. nat.) genehmigte Abhandlung

Vorgelegt von

Andreas Chatzopoulos

aus Ludwigsburg

Hauptberichter:	Prof. Dr. H.-R. Trebin
Mitberichter	Prof. Dr. C. Holm
Tag der mündlichen Prüfung:	30.03.2015

Institut für Theoretische und Angewandte Physik
der Universität Stuttgart

2015

Meinen Eltern.

Contents

Summary in English	xiii
Zusammenfassung in deutscher Sprache	xix
1 Introduction	1
2 Atomistic Computer Simulations	3
2.1 Ab-initio Methods	4
2.2 Classical Molecular Dynamics	5
2.3 Molecular Dynamics with Long-Range Interactions	8
2.3.1 Ewald Summation Technique	8
2.3.2 The Model of Streitzi and Mintmire	16
2.3.3 Beyond Streitzi and Mintmire	21
2.3.4 The Model of Tangney and Scandolo	29
3 Methodological Progresses	31
3.1 Iterative Solvers	32
3.1.1 Minimization of a Quadratic Form	32
3.1.2 Implementation	41
3.2 Wolf Summation Method	41
3.2.1 Charge Optimization with Wolf	49
3.2.2 Wolf Summation for Dipoles	51
3.3 Potentials for Oxides	54
3.3.1 Simulations with ReaxFF	59
3.3.2 CuSiO ₂ with COMB	60
3.3.3 Variable Charges for Dipoles	61
4 Flexoelectricity	67
4.1 MD Simulations	69
4.1.1 Displacement Modes	70
4.1.2 Primary Polarization	72

4.1.3	Induced Polarization	75
4.2	The Flexoelectric Constant μ_{11}	77
4.3	The Resulting Flexoelectric Constants	79
5	Conclusion and Outlook	85
A	The Software Package IMD	87
B	Interactions Integrals	89
C	Transformation of the Flexoelectric Tensor	91
	Literaturverzeichnis	93
	Bibliography	93

List of Symbols

E_{es}	Electrostatic energy, page 16
r_c	real space cut-off, page 8
COMB	Charge Optimized Many-Body, page 25
CTIP	Charge Transfer Ionic Potential, page 21
DCT-BOP	Dynamic Charge Transfer Bond Order Potential, page 24
EAM	Embedded Atom Method, page 8
EIM	Embedded Ion Method, page 23
HV	Hong and Vanderbilt, page 68
IMD	ITAP Molecular Dynamics, page 5
LCP	Local Chemical Potential, page 24
MD	Molecular Dynamics, page 3
MPI	Message Passing Interface, page 85
ReaxFF	Reactive Force Field, page 28
SM	Streitz and Mintmire, page 16
TS	Tangney and Scandolo, page 29
TTM	Two-Temperature Model, page 85

List of Figures

2.1	Motion of a single particle during a MD step.	7
2.2	The main idea of the EWALD summation method.	11
3.1	Path to the minimum via the method of steepest descent. . .	34
3.2	Error terms for \mathbf{A} -orthogonal search directions.	36
3.3	Using conjugate search directions for reaching the minimum. . .	38
3.4	Spherical truncation and charge neutralization.	43
3.5	The MADELUNG energy in case of charge neutralization. . .	45
3.6	Energy oscillations are additionally damped.	48
3.7	Charge optimization with the modified model of SM.	50
3.8	Charge distribution of an $\text{Al}_2\text{O}_3/\text{Al}$ -interface structure. . .	51
3.9	The dipole structure scalar of liquid silica.	53
3.10	Equation of state for liquid silica at 3100 K.	54
3.11	Tensile test of bulk AlO along the $\langle 1\bar{2}10 \rangle$ -direction.	55
3.12	Tensile test of bulk AlO along the $\langle 10\bar{1}0 \rangle$ -direction.	56
3.13	Tensile test of bulk AlO along the $\langle 0001 \rangle$ -direction.	57
3.14	Al/ Al_2O_3 relaxed by ab-initio and MD simulation.	58
3.15	Charge difference across the Cu/ α -quartz interafce	61
3.16	Crack propogation with variable charges.	63
3.17	Visualizing the crack propogation with MegaMol	64
4.1	Visualization of the crack tip with MegaMol	68
4.2	Different displacements modes for periclase.	71
4.3	Convergence behavior of the polarization.	74
4.4	Orientation of the TS dipoles.	76
4.5	The direction of the electric field.	76
4.6	Convergence behavior of the polarization for mode (a') . . .	78
4.7	Both parts of polarization as a function of strain gradient. .	80

List of Tables

3.1	Adhesion energies of the Al/Al ₂ O ₃ -interface system.	60
4.1	Values of flexoelectric constants	83

Numerical Simulations of Metal-Oxides

Summary in English

Oxides like silicates (SiO_2), alumina (Al_2O_3) or periclase (MgO), are materials with significant properties and are therefore investigated extensively in experiment and in theory. The aim of this PhD thesis was to propose and further to develop methods, which make molecular dynamic simulations of oxides with large particle numbers and for long simulation times possible.

The work consists of three parts. In the first one the already existing methods for simulating oxides will be discussed, while in the second one their methodological progress will be presented. The third chapter is solely reserved for the phenomenon of flexoelectricity, which has been discovered during the visualization of the crack propagation in alumina (Al_2O_3).

Introduction

Oxides are ionic materials with charged and polarizable atoms. Thus, the interaction between the atoms is of long-range nature. The molecular dynamics (MD) of such systems is quite problematic, since the forces do not fall quickly to zero within the usual cut-off radii. This can be only ensured by applying special methods.

Methods

One of them is the summation method by EWALD. Originally, it proposes a solution of the conditionally convergent sum of the electrostatic energy for N point charges, the so-called problem of MADELUNG in solid state physics. The main idea is to smear the charges by an additional charge

density of opposite sign, making the resulting sum converging rapidly. The most common choice for the smearing function is a GAUSSIAN shape. At the same time this GAUSSIAN part is subtracted again, so that physics remains unaltered. By solving the POISSON equation with this modified charge density the electrostatic energy splits into three contributions: one in direct space, one self-energy part and one in reciprocal space. The last part follows from the GAUSSIAN charge distribution, since in that space the corresponding sum converges much faster. How fast the convergence is taking place, depends on the EWALD parameter κ and the two cut-off radii r_c (direct space) and k_c (reciprocal space). They have to be chosen in such a way as to keep the error minimal. In that case the summation method of EWALD scales with $\mathcal{O}(N^{3/2})$.

The pure metal is covered in nature by oxide layers. Thus, metal-oxide systems have to be simulated. The valences of the metal atoms increase from zero to a finite value as one approaches the interface from the pure metal side. There are different methods describing the charge distribution of such combined systems in the simulation correctly. One of them is the method of Streitzi and Mintmire (SM). In their model the electrostatic energy is expressed as a quadratic function of the charges. By minimizing this function with the constraint of net-charge neutrality the desired valences of the system are obtained. For this purpose a linear system of equations has to be solved by inversion of the corresponding matrix. The non-diagonal elements of the matrix contain the long-range term $1/r_{ij}$, with r_{ij} being the distance between the atoms i and j . SM treated it by the method of EWALD. For the non-electrostatic interaction an EAM potential is used. This method has been firstly applied for the Al/Al₂O₃-system.

An alternative model for simulating oxides has been proposed by Tangney and Scandolo (TS). The oxygen atoms have an additional property, namely the polarizability and, thus, they have a dipole moment. In addition to the original COULOMB-interaction between charges, also charge-dipole and dipole-dipole forces occur. For these long-range interactions the summation technique of EWALD is used. A MORSE-stretch potential is assumed for the short-range pair interactions of the ions. The dipole of each oxygen atom splits into a short-range and induced part. The last one is the product of polarizability and local electric field, which depends on the locally arranged charges and dipole moments. The solution has to be therefore self-consistently. TS developed their model for silica.

Developments and Improvements

SM introduced their model in 1994 for the system of alumina. Since then, it has been transferred to other oxides and optimized at different points. In this work these alternative models are shown and are tested, whether are suitable for large-particle simulations. In summary, all these methods eliminate some problems of the origin SM model, but are less efficient.

For the purpose of this work, namely the simulation of metal-oxides with large number of atoms and for long simulations times, the computation of the long-range forces has been executed in a more efficient way. Instead of using the EWALD-sum as mentioned above, a reduced version has been applied. This summation method named by Wolf is a direct one, which incorporates the physical observation that charges can screen each other in ionic systems. Such a net-charge neutrality within a cut-off radius r_c is equivalent to a continuous truncation of the COULOMB potential at r_c . The Wolf-method has no reciprocal space part and, thus, needs no periodic boundary conditions in the simulation. It scales linear with the number of particles, which makes it to an efficient method for big systems.

For determining the valences by the SM model a linear system of equations has to be solved, which is done in this work by the conjugate gradient method. In contrast to the method of steepest descent it does not use search directions, which are orthogonal to each other, but as the name suggests, conjugated ones. Another optimization of the SM model is to apply the Wolf-summation method also to the non-diagonal entries of the interaction matrix, since they contain the long-range term $1/r_{ij}$. In such a way the charge computation during the MD is accelerated by the factor 60. Charge values, which have been determined by the EWALD- and the Wolf summation method differ about 1.1%.

After the successful implementation of the SM model in IMD (ITAP Molecular Dynamics), simulations have been executed both on pure alumina and on the Al/Al₂O₃-interface system. Unfortunately, the EAM potential proposed by SM was not appropriate for the stabilization of the interface. Also other attempts to stabilize the combined system failed.

Since the model of TS has been transferred to other oxide systems like periclase (MgO) and alumina (Al₂O₃) it was obvious to connect it with the model of SM. Dipoles with variable charges are the result. It has been applied on the crack propagation in Al₂O₃. The computed charge values, which follow from the SM model correspond to the valences of the

system. However, at TS the charge q_i is an optimization parameter, as the other quantities of the model. A further improvement of the original approach was to execute a new optimization routine in `potfit` with the range of q_i limited to +3 and -2. Unfortunately, the TS potential parameters were only successful optimized with adjusted charge values +2 and -1.4. This compromise one has to make if both models are merged. Nevertheless, the combined model is about two orders faster than methods like the *Charge Optimized Many Body* (COMB) potential or the *Reactive Force Field* (ReaxFF). By use of it charge fluctuations have been observed during the crack propagation, which have been visualized by the visualization tool `MegaMol`.

Flexoelectricity

Flexoelectricity is the phenomenon, where a polarization arises by applying non-uniform stress on a material. In contrast to piezoelectricity it appears also in systems, which are inversion symmetric. By visualizing the crack propagation in Al_2O_3 with `MegaMol`, domains with an anti-ferroelectric dipole arrangement have been observed. For a better understanding of the phenomenon the simple cubic system of periclase MgO was regarded. MgO has sodium chloride structure and three flexoelectric constants. As a first step three different deformation modes (bending, inhomogeneous elongation, shearing) with different strengths of the strain gradient have been executed on a system of about 120,000 atoms. Two of the coefficients have been determined by a relaxation of 60,000 MD steps, after the deformation has been kept by fixing the first atomic layers of the sample. The result was a homogeneous polarization, which consisted of two parts: the primary one, which resulted from the asymmetric displacement of the ionic charges due to the strain gradient after relaxation, and an induced one due to the deformation of the electronic orbits of the oxygen atoms, since here the potential model of TS for MgO has been applied. As expected, polarization and strain gradient showed a linear dependence. From the slope of the lines two of the flexoelectric constants have been determined. For the third one (longitudinal mode) no surface stabilization was possible. The atoms would have relaxed to their initial undeformed positions. For this purpose the sample was firstly rotated by 45° and then bent. The flexoelectric constant from this modified geometry was expressed by the other three. Since

two of them were already known, the third could be determined.

Résumé

The model of SM has been implemented in a modified form in IMD. The improvements were the use of an iterative method for solving the appearing linear system of equations and the computation of the long-range interactions by the summation method of Wolf. Concerning the computation of the charge values a significant acceleration by the factor 60 was achieved. For the non-electrostatic potential, which describes the short-ranged interaction of the atoms SM proposed an EAM potential. For the crack propagation in Al_2O_3 and for the stabilization of the Al/ Al_2O_3 -interface this potential was inappropriate. Attempts with other potentials also failed. The TS-potential, which has been successfully transferred to other oxide systems like Al_2O_3 and is available in IMD was combined with the SM model. In such a way the crack propagation in Al_2O_3 was simulated with variable charges.

In a visualization of the crack tip in alumina the phenomenon of flexoelectricity was observed. It was reproduced in the simple cubic system of periclase by applying three different deformation modes. By increasing the strength of the strain gradient linearly, fixing the surfaces and executing a relaxation a homogeneous polarization was achieved and, thus, it was possible to determine all three flexoelectric constants of MgO for the first time by MD simulations.

Numerische Simulationen von Metalloxiden

Zusammenfassung in deutscher Sprache

Oxide, wie z.B. Silikate (SiO_2), Korund (Al_2O_3) oder Periklas (MgO), sind bedeutende Funktionswerkstoffe und werden daher experimentell wie theoretisch intensiv untersucht. Ziel dieser Dissertation war es, Verfahren vorzustellen und derart zu optimieren, dass sie Molekulardynamiksimulationen von Oxiden mit großen Teilchenzahlen und über lange Zeiten ermöglichen.

Die Arbeit gliedert sich dabei in drei Bereiche. Im ersten Teil wird auf die einzelnen bereits vorhandenen Methoden zur Simulation von Oxiden eingegangen, im zweiten Kapitel deren Verbesserung vorgestellt. Der dritte Bereich widmet sich ausschließlich dem Phänomen der Flexoelektrizität, welche durch die geschickte Visualisierung der Rissausbreitung in Korund (Al_2O_3) entdeckt wurde.

Einleitung

Oxide sind ionische Substanzen mit geladenen und polarisierbaren Atomen. Die dabei auftretenden interatomaren Wechselwirkungen sind somit von weitreichender Natur. Die Molekulardynamik (MD) solcher Systeme ist problematisch, da diese Kräfte innerhalb der gängigen und effizienten Abschneideradien nicht schnell genug gegen Null abfallen. Es müssen daher Verfahren herangezogen werden, die dies gerade sicherstellen.

Methoden

Eines davon ist die Summationsmethode nach EWALD. Ursprünglich wurde sie für die bedingt konvergente Summe der elektrostatischen Energie einer Ansammlung von N Punktladungen entwickelt. Sie lieferte somit eine Lösung für das sogenannte MADELUNG-Problem im Festkörper. Die Vorgehensweise ist die, dass die Ladungen mit einer GAUSSSchen Ladungsverteilung entgegengesetzten Vorzeichens ausgeschmiert werden, damit die resultierende Summe schneller konvergiert. Gleichzeitig wird dieser GAUSSSche Anteil wieder abgezogen, um die Physik unverändert zu lassen. Mit dieser neuen Ladungsverteilung löst man dann die POISSON-Gleichung und erhält die elektrostatische Energie in drei Beiträge aufgeteilt. Einen im direkten Raum, einen Selbstenergie-Term und einen Anteil im reziproken Raum. Letzterer rührt von der GAUSSSchen Ladungsverteilung her, konvergiert doch die entsprechende Summe dort um einiges schneller. Wie schnell die einzelnen Beiträge tatsächlich konvergieren, wird durch den EWALD-Parameter κ und zwei Abschneideradien r_c (direkter Raum) und k_c (reziproker Raum) festgelegt. Die Wertewahl erfolgt dabei so, dass der Fehler möglichst minimal wird. In diesem Fall skaliert die EWALD-Summe mit $\mathcal{O}(N^{3/2})$.

Das reine Metall ist in der Natur in der Regel mit Oxidschichten bedeckt. In der Molekulardynamiksimulation hat man es somit mit Metall-Oxid-Systemen zu tun. Dabei bauen sich die Valenzladungen im Oxid zur Grenzschicht zum Metall hin ab. Es gibt dazu verschiedene Verfahren, welche diese Ladungsverteilung an der Grenzschicht während der Simulation korrekt wiedergeben. Eines davon ist das von Streit und Mintmire (SM). In diesem Modell wird die elektrostatische Energie als quadratische Funktion in den Ladungen aufgestellt. Minimiert man diese unter der Nebenbedingung der Ladungsneutralität, erhält man die gewünschten Valenzen des Systems. Dabei muss ein lineares Gleichungssystem durch Inversion der entsprechenden Matrix gelöst werden. Die Nicht-Diagonalelemente der Matrix enthalten den weitreichenden $1/r_{ij}$ -Term, wobei r_{ij} der Abstand zwischen den Atomen i und j ist. Dieser wird bei SM mit der EWALD-Methode behandelt. Für die nicht-elektrostatische Wechselwirkung wird ein EAM-Potenzial herangezogen. Diese Methode wurde erstmals für das System Al/Al₂O₃ entwickelt.

Ein alternatives Modell, um Oxide in der Simulation korrekt zu beschreiben, ist das von Tangney und Scandolo (TS). Die Sauerstoffato-

me bekommen als zusätzliche Teilcheneingeschaft eine Polarisierbarkeit zugeschrieben und können demnach ein Dipolmoment ausbilden. Neben der COULOMB-Wechselwirkung treten somit Ladungs-Dipol- und Dipol-Dipol-Wechselwirkungen auf. Diese weitreichende Kräfte werden mit dem EWALDSchen Summationsverfahren behandelt. Für die kurzreichende Paar-Wechselwirkung wird ein MORSE-stretch Potenzial angesetzt. Die Dipolmomente selber werden in einen kurzreichenden und induzierten Beitrag aufgeteilt. Letzterer ergibt sich als Produkt aus Polarisierbarkeit und lokalem elektrischen Feld, welches wiederum von allen umliegenden Ladungen und Dipolmomenten abhängt. Eine selbstkonsistente Bestimmung der Dipolmomente ist somit nötig. TS entwickelten und präsentierten ihr Modell für Siliziumdioxid.

Weiterentwicklungen und Verbesserungen

SM stellten ihr Modell 1994 für Aluminiumoxid vor. Seitdem wurde es auf weitere Oxide übertragen und an der einen oder anderen Stelle weiterentwickelt bzw. optimiert. In dieser Arbeit werden die meisten alternativen Modelle aufgezeigt und bzgl. ihres Einsatzes auf große Teilchenzahlen geprüft. Als Resümee lässt sich sagen, dass viele dieser Verfahren zwar Schwachstellen des ursprünglichen SM Modells beseitigen, aber hinsichtlich ihrer Effizienz einen Schritt nach hinten bedeuten.

Für das Vorhaben dieser Dissertation, Metalloxide mit großen Teilchenzahlen und über längere Zeiten zu simulieren, wurde zunächst die Berechnung der weitreichenden Wechselwirkungen wirkungsvoller gestaltet. Anstatt wie oben beschrieben die EWALD-Summe heranzuziehen, wurde eine verkürzte Version davon verwendet. Dieses nach Wolf benannte Summationsverfahren ist ein direktes, welches die physikalische Beobachtung berücksichtigt, dass sich Ladungen in ionischen System gegenseitig abschirmen können. Diese Ladungsneutralität innerhalb eines gegebenen Abschneideradius r_c ist äquivalent zu einem stetigen Abscheiden des COULOMB-Potentials. Die Wolf-Methode kommt dabei ohne reziproken Anteil aus und benötigt somit keine periodische Randbedingungen mehr in der Simulation. Die Skalierung ist dadurch linear in der Anzahl der Teilchen, was sie zu einem effizienten Verfahren gerade für große Systeme macht.

Für die Bestimmung der Valenzen bei SM wird ein lineares Gleichungssystem aufgestellt, welches in dieser Arbeit durch das iterative Conjugate-

Gradient (CG) Verfahren gelöst wird. Als Nachfolger der Methode des steilsten Abstiegs verwendet dieses nicht zueinander orthogonale Suchrichtungen, sondern, wie der Name schon verrät, konjugierte. Eine weitere Optimierung des SM Modells, die hier durchgeführt wurde, ist, die weitreichenden Terme, die innerhalb der oben erwähnten Nicht-Diagonalelemente der Wechselwirkungsmatrix vorkommen, auch mit der Wolf-Summe zu behandeln. Dadurch erfolgt die Ladungsberechnung innerhalb der MD um den Faktor 60 schneller. Vergleicht man die Ladungswerte einmal mit dem EWALD- und anderndmal mit dem Wolf-Verfahren berechnet, so unterscheiden sich diese lediglich um 1.1%.

Nach erfolgreicher Implementierung des SM Verfahrens im hauseigenen Code IMD (ITAP-Molekulardynamik) wurden damit Simulationen sowohl an reinem Aluminiumoxid, als auch am Al/Al₂O₃-Grenzflächensystem durchgeführt. Leider stellte sich heraus, dass das von SM vorgeschlagene EAM-Potenzial nicht geeignet ist, die Grenzfläche korrekt darzustellen. Es wurden andere Versuche vorgenommen das zusammengesetzte System zu stabilisieren, jedoch ohne Erfolg.

Da das Modell von TS bereits erfolgreich auf andere Oxide wie Magnesia (MgO) und Alumina (Al₂O₃) übertragen worden war, war es naheliegend, dieses herzunehmen, und mit dem von SM zu verknüpfen. Das Ergebnis sind Dipole mit variablen Ladungen. Angewandt wurde es auf die Rissausbreitung in Al₂O₃. Während beim SM-Modell die berechneten Ladungswerte den experimentell bestimmten Valenzen des System entsprechen, hier +3 und -2 für die Al- bzw. O-Atome, stellt die Ladung q_i bei TS, neben den anderen Größen des Modells einen reinen Optimierungsparameter dar. Als weitere Verbesserung des Verfahrens wurde nun `potfit` herangezogen und eine erneute Optimierung aller TS-Potenzialparameter durchgeführt, wobei sich q_i nun im Wertebereich von +3 bis -2 bewegen durfte. Eine erfolgreiche Optimierung stellte sich hingegen nur bei angepassten Ladungswerten von +2 und -1.4 ein. Diesen Kompromiss musste man bei der Verbindung beider Modelle eingehen. Das Verfahren ist aber um zwei Größenordnungen schneller als Methoden wie *Charge Optimized Many Body* (COMB)-Potenzial oder das *Reactive Force Field* (ReaxFF). Es konnten damit Ladungsfuktuationen beobachtet werden, während sich der Riss ausbreitet. Diese wurden mit Hilfe des Visualisierungstools `MegaMol` sichtbar gemacht.

Flexoelektrizität

Als Flexoelektrizität bezeichnet man das Phänomen, dass sich bei einer inhomogenen Deformation eines Materials eine Polarisierung einstellt. Anders als bei der Piezoelektrizität, tritt diese auch bei Systemen mit Inversionssymmetrie auf. Bei der Visualisierung der Rissausbreitung von Al_2O_3 mit **MegaMol** konnte man Domänen antiferroelektrischer Dipolanordnungen erkennen. Um die Erscheinung genauer zu verstehen, wurde zunächst das einfache kubische System von Magnesia (MgO) betrachtet. Es besitzt Natriumchlorid-Struktur und drei flexoelektrische Konstanten. Zunächst wurden drei verschiedene inhomogene Deformationen (Biegung, inhomogene Dehnung und Scherung) mit jeweils unterschiedlich starken Gradienten der Verzerrung auf ein System von rund 120.000 Atomen ausgeführt. Zwei der Konstanten konnten bestimmt werden, indem man die Deformation durch Fixieren der Oberflächenatome aufrecht erhielt und eine Relaxation von 60.000 MD-Schritten durchführte. Es stellte sich eine homogene Polarisierung ein. Die Polarisierung selber wies dabei zwei Anteile auf. Einmal den primären Beitrag, der sich durch die Verschiebung der Atomkerne ergab und den induzierten Beitrag. Letzterer folgt aus der gleichmäßigen Ausrichtung der Dipolmomente der Sauerstoffatome. Verwendet wurde hierbei das Potenzialmodell von TS für MgO . Polarisierung und Gradient der Deformation folgten, wie zu erwarten, einem linearen Verlauf. Aus der Steigung der Kurven konnten die Konstanten ermittelt werden. Die longitudinale Mode erwies sich als problematisch, da hier keine Oberflächenstabilisierung möglich war. Die Atome fallen bei der Relaxation sofort wieder auf ihre Gleichgewichtspositionen zurück. Daher wurde die Probe in ein 45° -gedrehtes Koordinatensystem betrachtet und dann anschließend gebogen. Die sich dabei ergebende flexoelektrische Konstante konnte durch alle anderen drei ausgedrückt werden. Da zwei davon bereits bekannt waren, konnte somit die dritte und fehlende Konstante bestimmt werden.

Resümee

Das Modell von SM wurde in verbesserter Form in IMD implementiert. Die Verbesserungen waren die Verwendung eines iterativen Gleichungssystemslösers sowie die Berechnung der weitreichenden Wechselwirkung mit dem Wolf'schen Summationsverfahren. Damit konnte, was die Ladungsbe-

rechnung betrifft, eine deutliche Beschleunigung hinsichtlich der Simulationsdauer erzielt werden. Neben der elektrostatischen Energie gibt es noch ein nicht-elektrostatisches Potenzial, welches die kurzreichende Wechselwirkung der Atome wiedergibt. SM schlugen dazu ein EAM-Potenzial vor, welches sich aber für die Rissausbreitung in Al_2O_3 und für die stabile Simulation der $\text{Al}/\text{Al}_2\text{O}_3$ -Grenzfläche, als ungeeignet erwies. Es wurden andere Potenziale herangezogen, die leider auch nicht zum Erfolg führten. Das TS-Potenzial, welches in IMD mit Wolf-Behandlung der weitreichenden Wechselwirkungen vorliegt, wurde erfolgreich auf andere Oxide übertragen, u.a. Al_2O_3 . Durch die Verknüpfung mit dem SM-Modell, konnte man die Rissausbreitung in Al_2O_3 mit variablen Ladungen simulieren.

Bei der Visualisierung des Risses in Alumina ergab sich das Phänomen der Flexoelektrizität. Anhand von Magnesia konnte dieses gezielter reproduziert werden. Dabei wurden drei unterschiedliche Verschiebungsfelder auf dieses kubische System angewendet und eine homogene Polarisierung erzielt. Indem man die Stärke der Verzerrung variierte, die Oberflächen festhielt und das System lange relaxierte, ließen sich die flexoelektrischen Konstanten für MgO bestimmen.

Chapter 1

Introduction

Metal-oxide systems play a decisive role in electronic industry. There is a wide application of such combined systems with different and special properties. Perovskite oxides are one example for next-generation electronic materials. This is because of their high T_c superconductivity, their giant magnetoresistance, their multiferroic and catalytic behavior and their colossal thermoelectric and magnetocaloric effects [29, 74, 82, 87]. Also quantum states of matter can be generated and manipulated by creating quantum wells from nanostructured transition metal-oxides [76]. Furthermore, thin films of oxides and interface structures exhibit a new kind of magnetism in solid matter. The magnetic order at their interfacial region can be affected, if their electronic structure is changed as a consequence of broken symmetry, strain, and atomic or electronic reconstruction to ensure local charge neutrality [14]. Therefore, it is essential to describe such systems in molecular dynamics simulations correctly.

Oxides or metal-oxide interfaces contain electric charges and dipole moments and, hence, the atoms interact by long-range forces. For this purpose suitable interaction potentials must be established and implemented in the molecular dynamics code IMD (ITAP-Molekulardynamik) [75], used in this work. With this tool the behavior of the materials under mechanical and thermal loads can be studied.

The thesis is organized in three parts. In the first one a detailed introduction of atomistic computer simulations is given. The main focus is there on molecular dynamics with long-range interactions. One method how they can be treated is the summation technique by EWALD [25]. An extensive derivation of the EWALD sum is presented. For the correct treatment of the charge distribution on a metal-oxide interface the variable charge model of Streitzi and Mintmire (SM) [78] is considered and alternative approaches are shown and discussed. Tangney and Scandolo suggested a method based on the polarizability of the oxygen atoms, which therefore exhibit dipole

moments [81]. This dipole model is also explained here. In the second part of the work methodological improvements of the SM method are worked out. Using a conjugate gradient solver and the summation method of Wolf [88] for the long-range interactions are the major ones. The differences between Wolf and EWALD are also presented explicitly. These developments are applied to pure alumina (Al_2O_3) and to the Al/ Al_2O_3 -interface structure. For studying the crack propagation in Al_2O_3 with variable charges both models of SM and TS have been combined.

In the last part the phenomenon of flexoelectricity [41] is illustrated, since it has been observed at the crack analysis of alumina [34]. The flexoelectric effect of generating a polarization by a strain grained was reproduced in the simple cubic oxide periclase (MgO) by use of three well defined displacement modes. In such a way all three flexoelectric constants of MgO could be determined by molecular dynamics for the first time. A summary of the thesis is given at the end.

Chapter 2

Atomistic Computer Simulations

Computer simulations have become a powerful tool in all natural sciences and in engineering. In addition to experiment and theory they nowadays represent a separate discipline, which provides insights and answers to many problems from a different angle of view.

Especially in physics, simulations are applied on a broad basis. From solid state physics to astrophysics they cover a wide range of different branches and length scales.

For simulations on an atomistic level two approaches exist. The system can be either described quantum mechanically or classically. In the first case the computation of the system properties are done *from first principles* or *ab-initio*, while in the second one the interaction between the particles is governed by *effective potentials*, which have been fitted to empirical or ab-initio data [24]. The classical description is called *molecular dynamics* (MD) and is used for the atomistic simulation of metal-oxide systems in this thesis. It is presented here in detail, while for the ab-initio calculations only a brief introduction is given.

Metal-oxide systems need a special treatment in the molecular dynamics simulation, since their atoms are charged and exhibit dipole moments. Thus, the interatomic forces are of long-range nature and have to be handled by methods like the EWALD summation technique [25].

Also variable charge methods have to be introduced, since the values of the charges usually change during the simulation. This has a dramatic effect on the electrostatic interaction, which controls the main properties of the oxide. Such a charge transfer model was proposed by Streitz and Mintmire [78]. The main idea of it and its improvements in the last years will be discussed in detail in this chapter in combination with the summation method of EWALD mentioned above.

An alternative model for describing oxides in the MD correctly was suggested by Tangney and Scandolo [81]. They introduce the polarizability as

an additional particle property for the oxygen atoms. Therefore, dipole moments can arise, which govern the behavior of the oxide in the simulation. This model is illustrated at the end of the present chapter.

2.1 Ab-initio Methods

The state of a quantum mechanical system consisting of N atoms is described by the many-atom wave function $\Psi(\mathbf{r}_i, \mathbf{R}_j, t)$, with \mathbf{r}_i being the coordinates of the electrons and \mathbf{R}_j indicating the positions of the nuclei. For the dynamics of Ψ the time-dependent SCHRÖDINGER equation is considered:

$$\hat{\mathcal{H}}\Psi = i\hbar\frac{\partial}{\partial t}\Psi, \quad (2.1)$$

depending only on natural constants and the space coordinates of nuclei and electrons. Applying ab-initio calculations in atomistic simulations means to solve the above equation for a many-body system without the use of external parameters and empirical data. That is the reason, why they are called *first principles* calculations. A solution for Eq. (2.1) can be only obtained for a few 100 or 1000 atoms. This solution, which is an approximate one, follows from different assumptions, like the one suggested by BORN and OPPENHEIMER. Since nucleus and electron largely differ in mass, their motion can be regarded separately. The electronic problem, which is the main task of the ab-initio method, is then solved [67]. Also other approaches for the same issue exist, e.g. the HARTREE-FOCK method or the *density functional theory* (DFT).

In the work presented here ab-initio methods have been only used for the fitting procedure of effective potentials. These are potentials, which introduce an empirical interaction between the atoms, based on ab-initio data and are able to simulate systems with a larger number of particles [24]. They are trained to different modifications and conditions of the atomic structure one is interested for, like under high stress or in the molten state. For these *reference structures* the forces are calculated with an ab-initio code, e.g. VASP [43–46]. A set of parameters $\{p_i\}$, which characterizes the potential has to reproduce these forces, including in this optimization also experimental data such as cohesive energies, elastic constants and lattice parameters. The best set minimizes the mean square error. The idea of this *force matching method* is simple, but the execution is rather compli-

cated and time-consuming. A software tool named `potfit`, which is freely available, has been developed for this purpose and has been applied to the creation of different oxide potentials [9].

2.2 Classical Molecular Dynamics

Since the interatomic interaction is replaced by effective potentials, the atoms are not considered any more as a quantum mechanical system of nucleus and electron, but they are reduced to classical point particles. Computing the trajectory of these particles in the simulation is the main task of molecular dynamics. Hence, NEWTONS equation of motion,

$$\mathbf{F}_j = m_j \frac{d^2 \mathbf{r}_j}{dt^2} = -\nabla_j U_{\text{eff}}(\mathbf{r}_1, \dots, \mathbf{r}_N), \quad (2.2)$$

has to be solved for N interacting atoms numerically. The force \mathbf{F}_j , which acts on atom j , is written as gradient of the effective potential, because in that description U_{eff} is equal to the total potential energy of the system. Above equation is integrated in a recursive way by discretizing the time into small steps δt . By knowledge of the particles positions and velocities at a particular time t_0 , a specific algorithm is used to calculate them at the later time $t_0 + \delta t$. The most prominent numerical approaches for this purpose are the methods of GAUSS, RUNGE-KUTTA and VERLET. In the MD software package IMD the latter one is implemented [75]. How the implementation can be realized is illustrated for instance in *Numerical Recipes* [61]. One of the different versions of this algorithm of VERLET is the so-called *velocity VERLET method*. In addition to the position also the velocity of the atom j at the time $t_0 + \delta t$ is explicitly computed via a simple TAYLOR expansion:

$$\mathbf{r}_j(t_0 + \delta t) = \mathbf{r}_j(t_0) + \mathbf{v}_j(t_0) \delta t + \frac{\mathbf{F}_j(t_0)}{2m_j} \delta t^2 \quad (2.3)$$

$$\mathbf{v}_j(t_0 + \delta t) = \mathbf{v}_j(t_0) + \frac{\mathbf{F}_j(t_0) + \mathbf{F}_j(t_0 + \delta t)}{2m_j} \delta t. \quad (2.4)$$

In general the choice of the time step δt is essential for the correct simulation of the system one is interested for. It has to be in the same range as the typical time scales, which appear in the system. Since atomic motions are in the order of some femtoseconds, δt takes for atomistic simulations

values between 0.1 and 2 fs. How the position of a single atom during a MD step changes and how its trajectory can be calculated in the simulation is shown in Fig. 2.1.

MD calculations are performed either in the microcanonical or canonical ensemble, since the number of particles N is fixed. The corresponding simulations are called NVE or NVT simulations, with V being the volume, E the energy and T the temperature, respectively [58, 59]. The last quantity is controlled by an external heat bath, which is coupled to the system. It is realized by a thermostat. Also a barostat can be added controlling the pressure P for the case that the volume varies. This would be then a NPT ensemble. The solution of the equation of motion given by the Eqs. (2.3) and (2.4) is only applicable for the simulation of a NVE ensemble, since NVT and NPT simulations modify the original form of Eq. (2.2). An additional friction term is necessary for the thermostat, while the pressure control, which requires a rescaling of the box size, also affects NEWTONS equation of motion.

The main idea of the effective potential has been already pointed out in the previous section. It characterizes the simultaneous interaction of each atom with all other ones and thus depends on the positions of all particles. This many-body interaction can be split into the single contributions of one, two, three or more directly interacting atoms, so that U_{eff} can be written as a sum of one-, two-, three-body etc. potentials:

$$U_{\text{eff}}(\{\mathbf{r}_l\}) = \sum_i \phi_i(\mathbf{r}_i) + \frac{1}{2} \sum_{\substack{i,j \\ i \neq j}} \phi_{ij}(\mathbf{r}_i, \mathbf{r}_j) + \frac{1}{6} \sum_{\substack{i,j,k \\ i \neq j \neq k \\ i \neq k}} \phi_{ijk}(\mathbf{r}_i, \mathbf{r}_j, \mathbf{r}_k) + \dots \quad (2.5)$$

The first term corresponds to an external potential and can be omitted, since it causes only a shift. The second one specifies the pairwise interaction between the particles, while the three-body interaction is given by the third term and so on. In general, the higher order terms can be ignored, because they do not affect the effective potential as much as the leading ones. Anyway, from a certain distance of interaction the value of U_{eff} is set by definition equal to zero, as it will be discussed in the next section.

For the description of most systems it is sufficient to consider only the interaction between atom pairs. Such a *pair potential* is normally isotropic

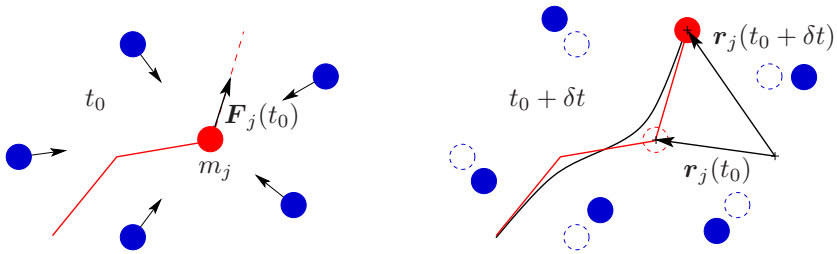


Figure 2.1: Schematic illustration of a MD step. At t_0 the net-force on atom j is computed (left side). After a time step δt this particle moved a certain distance along the action line of $\mathbf{F}_j(t_0)$. The positions of all other atoms also changed accordingly (right side). This procedure is done simultaneously for all particles at each δt , determining in such a way for longer times their trajectories.

and homogeneous and thus a function of the pair distance $r_{ij} = |\mathbf{r}_i - \mathbf{r}_j|$:

$$U_{\text{eff}}(r_{ij}) = \frac{1}{2} \sum_{\substack{i,j \\ i \neq j}} \phi_{t_i t_j}(r_{ij}), \quad i, j = 1, \dots, N. \quad (2.6)$$

ϕ is solely determined by the different combinations of the types t_i and t_j of the two atoms i and j . Pair potentials are well applied on liquids or solids of noble gases [2], to name only two examples. However, there are systems for which a pair potential would be a bad choice. Especially for metals or metallic alloys another sort of potential is preferred [19, 27].

Embedded Atom Method Potentials

Effective potentials for metals are usually proposed to be the sum of a pair term ϕ , which describes the direct core-core interaction of the ions and an additional cohesive contribution F . The latter part follows from the energy, which is released by *embedding* an ion core into the *sea of electrons*. The local electron density n determines the value of this embedding energy, which in turn depends on the contributions of the surrounding atoms. This kind of potential, originally developed by Daw and Baskes [18], is called *embedded atom method* (EAM) potential. It is related to the Finnis-Sinclair

model [26], so that for the potential energy the following form can be assumed:

$$U_{\text{eff}}(r_{ij}) = \frac{1}{2} \sum_{\substack{i,j \\ i \neq j}} \phi_{ij}(r_{ij}) + \sum_i F_i(n_i), \quad (2.7)$$

$$\text{with } n_i = \sum_{j \neq i} \rho_j(r_{ij}), \quad i, j = 1, \dots, N, \quad (2.8)$$

where the *transfer function* ρ_j specifies the single contribution of each other atom j to the electron density n of atom i . A review of theory and applications of the EAM potential is given in Ref. [20].

2.3 Molecular Dynamics with Long-Range Interactions

Calculating the interaction of each atom with all other ones, becomes in the simulation inefficient above a certain number of particles, since the computational effort scales with N^2 . A *space cut-off* r_c has to be introduced, which limits the distance of the interaction. For each atom only the force contributions of the those atoms are added, which are not further than r_c . Such a spherical truncation is not applicable for every kind of potential. The interaction has to be short-ranged. This is not the case for charge-charge or charge-dipole interactions. The corresponding potentials decay with r^{-1} and r^{-2} , so that non-negligible force and energy contributions further than r_c arise. To handle these long-range interactions, special methods have been developed. The most used is the method of EWALD [25], which is implemented in many MD-codes as a default option.

2.3.1 Ewald Summation Technique

For the electrostatic energy E of \mathcal{N} interacting point charges, the direct, pairwise summation of the COULOMB potential has to be carried out. The resulting sum:

$$E = \frac{1}{2} \sum_{i=1}^{\mathcal{N}} \sum_{j \neq i=1}^{\mathcal{N}} \frac{q_i q_j}{r_{ij}}, \quad (2.9)$$

with $r_{ij} = |\mathbf{r}_i - \mathbf{r}_j|$ being the distance between the charges q_i and q_j , is conditionally convergent and has to be treated in a different way. An efficient method was suggested by EWALD. It ensures the rapid convergence of E , also referred to as MADELUNG energy, by firstly forcing periodicity on the usually non-periodic system. Therefore, the vector $\mathbf{n} = (n_x, n_y, n_z)^t$ is introduced. Its components n_x , n_y and n_z are integers and build up the periodic image cells of the cubic simulation box with edge length L . Eq. (2.9) becomes to

$$E = \frac{1}{2} \sum_{i=1}^N \sum_{j=1}^N \sum_{\mathbf{n}=\mathbf{0}}^{\infty}{}' \frac{q_i q_j}{|\mathbf{r}_{ij} + \mathbf{n}L|}, \quad (2.10)$$

where the case $i = j$ for $\mathbf{n} = \mathbf{0}$ is not considered, which is indicated by the prime after the sum over \mathbf{n} . N specifies the number of charges within one single box. The next step of the EWALD summation technique would be to split the sum in Eq. (2.10) into two short-range parts. For understanding the main idea of this splitting and how it is realized physically, one has to look at the derivation of the electrostatic energy from Eq. (2.10). It results by solving the POISSON equation

$$\Delta\Phi(\mathbf{r}) = -4\pi\rho(\mathbf{r}), \quad (2.11)$$

subject to the constraint of net-charge neutrality:

$$\sum_{i=1}^N q_i = 0, \quad (2.12)$$

for the charge density:

$$\rho(\mathbf{r}) = \sum_{i=1}^N \sum_{\mathbf{n}=\mathbf{0}}^{\infty} q_i \delta(\mathbf{r} - \mathbf{r}_i + \mathbf{n}L). \quad (2.13)$$

As expected for point charges, the solution takes the form of the COULOMB potential:

$$\Phi(\mathbf{r}_j) = \sum_{i=1}^N \sum_{\mathbf{n}=\mathbf{0}}^{\infty}{}' \frac{q_i}{|\mathbf{r}_{ij} + \mathbf{n}L|}, \quad (2.14)$$

where Φ is regarded at the position of atom j . From the potential the electrostatic energy for the charges of one box follows as

$$E = \frac{1}{2} \sum_{j=1}^N q_j \Phi(\mathbf{r}_j). \quad (2.15)$$

The convergence behavior of this sum can be influenced by a different form of the charge density $\rho(\mathbf{r})$. This is the physical concept of the EWALD method [40]. An additional charge density is added, which smears the point charges in Eq. (2.13) and therefore makes the resulting sum converging rapidly. At the same time this contribution of opposite sign is subtracted from $\rho(\mathbf{r})$, affecting in no case the solution from Eq. (2.14). Concretely, $\rho(\mathbf{r})$ is modified to

$$\rho(\mathbf{r}) = \sum_{i=1}^N \sum_{\mathbf{n}=\mathbf{0}}^{\infty} [q_i \delta(\mathbf{r} - \mathbf{r}_i + \mathbf{n}L) - q_i \sigma_i(\mathbf{r} - \mathbf{r}_i + \mathbf{n}L) + q_i \sigma_i(\mathbf{r} - \mathbf{r}_i + \mathbf{n}L)], \quad (2.16)$$

with the smearing function σ_i . For σ_i any arbitrary function can be chosen, which falls quickly to zero for large distances $|\mathbf{r} - \mathbf{r}_i|$. The most common choice is to take a GAUSSIAN shape:

$$\sigma_i(\mathbf{r}) = \left(\frac{\kappa}{\sqrt{\pi}} \right)^3 e^{-\kappa^2 |\mathbf{r}|^2}. \quad (2.17)$$

Above charge density is splitted now into the parts:

$$\rho_{\text{dir}}(\mathbf{r}) = \sum_{i=1}^N \sum_{\mathbf{n}=\mathbf{0}}^{\infty} [q_i \delta(\mathbf{r} - \mathbf{r}_i + \mathbf{n}L) - q_i \sigma_i(\mathbf{r} - \mathbf{r}_i + \mathbf{n}L)], \quad (2.18)$$

and

$$\rho_{\text{rec}}(\mathbf{r}) = \sum_{i=1}^N \sum_{\mathbf{n}=\mathbf{0}}^{\infty} q_i \sigma_i(\mathbf{r} - \mathbf{r}_i + \mathbf{n}L), \quad (2.19)$$

with $\rho(\mathbf{r}) = \rho_{\text{dir}}(\mathbf{r}) + \rho_{\text{rec}}(\mathbf{r})$. The first one describes the overlapping of the point charges by σ_i , which effects a screening between distant charges, while $\rho_{\text{rec}}(\mathbf{r})$ is a simple correction term. For both charge densities the

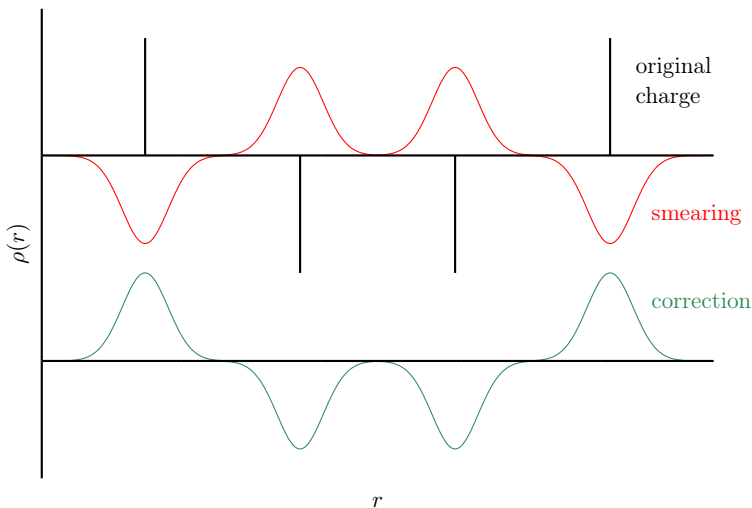


Figure 2.2: The original point charges screen each other, since they are overlapped by GAUSSIAN charge densities of opposite sign. This additional contribution is subtracted, so that physics remains unaltered.

POISSON equation has to be solved separately again. This is done for $\rho_{\text{dir}}(\mathbf{r})$ in direct space, however for the smearing functions it is carried out in FOURIER space. The reason for this is that in \mathbf{k} -space the convergence of the associated sum is achieved much easier, since long-range contributions of the physical space there become short-ranged ones. The sums of the corresponding energies E_{dir} and E_{rec} , which are then obtained are both of short-range nature compared to E from Eq. (2.10). The realization of this aim of the EWALD summation is also illustrated in Fig. 2.2.

Reciprocal Space Part

The POISSON equation is reconsidered for the GAUSSIAN charge distribution given by Eq. (2.19):

$$\Delta\Phi_{\text{rec}}(\mathbf{r}) = -4\pi\rho_{\text{rec}}(\mathbf{r}), \quad (2.20)$$

Since the potential $\Phi_{\text{rec}}(\mathbf{r})$ is searched as a function of the reciprocal space vector \mathbf{k} , $\Phi_{\text{rec}}(\mathbf{r})$ and $\rho_{\text{rec}}(\mathbf{r})$ are expanded in a FOURIER series:

$$\Phi_{\text{rec}}(\mathbf{r}) = \sum_{\mathbf{k}} \varphi_{\mathbf{k}} e^{i\mathbf{k}\cdot\mathbf{r}}, \quad (2.21)$$

$$\rho_{\text{rec}}(\mathbf{r}) = \sum_{\mathbf{k}} c_{\mathbf{k}} e^{i\mathbf{k}\cdot\mathbf{r}}. \quad (2.22)$$

The FOURIER coefficients are connected via Eq. (2.20):

$$\varphi_{\mathbf{k}} = \frac{4\pi}{k^2} c_{\mathbf{k}}, \quad (2.23)$$

where $c_{\mathbf{k}}$ is obtained from the integral:

$$c_{\mathbf{k}} = \frac{1}{V} \int_V \rho_{\text{rec}}(\mathbf{r}) e^{-i\mathbf{k}\cdot\mathbf{r}} d^3\mathbf{r}. \quad (2.24)$$

V denotes the volume of the box, which is equal to L^3 . The evaluation of the above integral is carried out as follows:

$$\begin{aligned} c_{\mathbf{k}} &= \frac{1}{V} \sum_{i=1}^N \sum_{\mathbf{n}=\mathbf{0}}^{\infty} \int_V q_i \left(\frac{\kappa}{\sqrt{\pi}} \right)^3 e^{-\kappa^2 |\mathbf{r}-\mathbf{r}_i+\mathbf{n}L|^2} e^{-i\mathbf{k}\cdot\mathbf{r}} d^3\mathbf{r} \\ &= \frac{1}{V} \sum_{i=1}^N \int q_i \left(\frac{\kappa}{\sqrt{\pi}} \right)^3 e^{-\kappa^2 |\mathbf{r}-\mathbf{r}_i|^2} e^{-i\mathbf{k}\cdot\mathbf{r}} d^3\mathbf{r} \\ &= \frac{1}{V} \sum_{i=1}^N q_i e^{-i\mathbf{k}\cdot\mathbf{r}_i} \exp\left(-\frac{k^2}{4\kappa^2}\right), \end{aligned} \quad (2.25)$$

where at the second step the replacement

$$\sum_{\mathbf{n}=\mathbf{0}}^{\infty} \int_V \rightarrow \int, \quad (2.26)$$

has been executed. From this and Eq. (2.23) the electrostatic potential of the GAUSSIAN smearing functions results as

$$\begin{aligned}\Phi_{\text{rec}}(\mathbf{r}) &= \sum_{\mathbf{k} \neq \mathbf{0}} \varphi_{\mathbf{k}} e^{i\mathbf{k} \cdot \mathbf{r}}, \\ &= \frac{1}{V} \sum_{\mathbf{k} \neq \mathbf{0}} \sum_{i=1}^N \frac{4\pi}{k^2} q_i e^{i\mathbf{k} \cdot (\mathbf{r} - \mathbf{r}_i)} \exp\left(-\frac{k^2}{4\kappa^2}\right).\end{aligned}\quad (2.27)$$

The corresponding energy takes the form:

$$\begin{aligned}E_{\text{rec}} &= \frac{1}{2} \sum_{j=1}^N q_j \Phi_{\mathbf{k}}(\mathbf{r}_j), \\ &= \frac{2\pi}{L^3} \sum_{\mathbf{k} \neq \mathbf{0}} S(k) \frac{\exp\left(-\frac{k^2}{4\kappa^2}\right)}{k^2},\end{aligned}\quad (2.28)$$

with the charge structure factor $S(k)$ defined as:

$$S(k) = \left| \sum_{j=1}^N q_j e^{i\mathbf{k} \cdot \mathbf{r}_j} \right|^2, \quad (2.29)$$

and $k = |\mathbf{k}|$. As expected, the result in Eq. (2.28) shows, that the reciprocal space part of the energy converges quickly.

In some cases the charge structure factor $S(k)$ becomes small for \mathbf{k} -vectors near zero, so that the contribution of $E_{\mathbf{k}}$ to the total energy is negligible. Wolf took regard of this and proposed an alternative summation method, which will be discussed in detail in Sec. 3.2.

The energy for $\mathbf{k} = \mathbf{0}$ is excluded from the expression of E_{rec} in Eq. (2.28) and is given in [88] by the following expression:

$$E_{\text{rec}}^{(\mathbf{k}=\mathbf{0})} = \frac{2\pi}{3V} \left(\sum_{i=1}^N q_i \mathbf{r}_i \right)^2. \quad (2.30)$$

It is related to the total dipole moment of the system. In general, systems of infinite size do not have a net dipole moment, so that $E_{\text{rec}}^{(\mathbf{k}=\mathbf{0})} = 0$. As an

example an ionic melt, which is of infinite size will not show a net dipole moment. This changes, if the system is finite and periodicity is artificially forced, as it is done here for easily applying the FOURIER transformation. As a consequence, $E_{\text{rec}}^{(\mathbf{k}=0)}$ is unequal zero and the dynamics of the system is modified by these finite-size effects. Thus, for the correct simulation of the infinite system, $E_{\text{rec}}^{(\mathbf{k}=0)}$ is usually omitted [88].

Another part of the energy E_{rec} , which can not be neglected is the self-energy of the GAUSSIAN charge distributions, which arises from the case $\mathbf{r}_i = \mathbf{r}_j$. To extract this contribution from Eq. (2.28), a separate examination of the corresponding potential is necessary.

Self-Energy Part

For one single GAUSSIAN charge distribution

$$\sigma(r) = \left(\frac{\kappa}{\sqrt{\pi}} \right)^3 e^{-\kappa^2 r^2}, \quad (2.31)$$

only the radial part of the POISSON equation has to be solved:

$$\frac{1}{r} \frac{\partial^2}{\partial r^2} (r\Phi_\sigma(r)) = -4\pi q\sigma(r). \quad (2.32)$$

Integrating twice, $\Phi_\sigma(r)$ results:

$$\Phi_\sigma(r) = \frac{q \operatorname{erf}(\kappa r)}{r} + \frac{c_1}{r} + c_2, \quad (2.33)$$

with the error function being the antiderivative of the GAUSSIAN:

$$\operatorname{erf}(\kappa r) = \frac{2\kappa}{\sqrt{\pi}} \int_0^r d\tau e^{-\kappa^2 \tau^2}, \quad (2.34)$$

and the two constants c_1 and c_2 . Arbitrarily $\Phi_\sigma(\infty) = 0$ can be set, so that $c_2 = 0$ follows. Because of the factor r in Eq. (2.32) the above solution contains the term c_1/r , which corresponds to a point charge at $r = 0$. Since there is no charge, c_1 is equal zero. At the limit $r \rightarrow 0$, which is identical to $\mathbf{r}_i = \mathbf{r}_j$, the potential of $\sigma(r)$ simplifies to

$$\Phi_\sigma(0) = \frac{2\kappa}{\sqrt{\pi}} q_i, \quad (2.35)$$

and the energy $E_{\mathbf{k}}$ has to be corrected by the term:

$$\begin{aligned} E_{\sigma} &= \frac{1}{2} \sum_{i=1}^N q_i \Phi_{\sigma}(0), \\ &= \frac{\kappa}{\sqrt{\pi}} \sum_{i=1}^N q_i^2. \end{aligned} \quad (2.36)$$

Real Space Part

The second part of the energy is gained by solving the POISSON equation for $\rho_{\text{dir}}(\mathbf{r})$ from Eq. (2.18) in real space:

$$\Delta \Phi_{\text{dir}}(\mathbf{r}) = -4\pi \rho_{\text{dir}}(\mathbf{r}). \quad (2.37)$$

For this charge density of the smeared point charges no integration has to be carried out, since the potential $\Phi_{\text{dir}}(\mathbf{r})$ can be specified immediately from the previous results given by the Eqs. (2.14) and (2.33):

$$\begin{aligned} \Phi_{\text{dir}}(\mathbf{r}_j) &= \sum_{i=1}^N \sum_{\mathbf{n}=0}^{\infty} ' \frac{q_i}{|\mathbf{r}_{ij} + \mathbf{n}L|} [1 - \text{erf}(\kappa|\mathbf{r}_{ij} + \mathbf{n}L|)], \\ &= \sum_{i=1}^N \sum_{\mathbf{n}=0}^{\infty} ' \frac{q_i \text{erfc}(\kappa|\mathbf{r}_{ij} + \mathbf{n}L|)}{|\mathbf{r}_{ij} + \mathbf{n}L|}. \end{aligned} \quad (2.38)$$

The complementary error function has been used, which is identical to:

$$\text{erfc}(\kappa r) = 1 - \text{erf}(\kappa r). \quad (2.39)$$

Finally, the energy E_{dir} takes the form:

$$\begin{aligned} E_{\text{dir}} &= \frac{1}{2} \sum_{j=1}^N q_j \Phi_{\mathbf{r}}(\mathbf{r}_j), \\ &= \frac{1}{2} \sum_{i=1}^N \sum_{j=1}^N \sum_{\mathbf{n}=0}^{\infty} ' \frac{q_i q_j \text{erfc}(\kappa|\mathbf{r}_{ij} + \mathbf{n}L|)}{|\mathbf{r}_{ij} + \mathbf{n}L|}. \end{aligned} \quad (2.40)$$

Total Energy

Hence, the total energy E from Eq. (2.10) has been split by this procedure of EWALD into three contributions:

$$E = E_{\text{dir}} + E_{\text{rec}} - E_{\sigma}. \quad (2.41)$$

How fast the sums of E_{dir} and E_{rec} converge, depends on the value of the EWALD parameter κ and on the two cut-off radii r_c and k_c , which are added in the simulation. How to choose these parameters correctly is discussed in [42]. In general, for a large r_c -value it makes sense to take a small κ and vice versa. The error, which follows from the truncation has to be kept in an acceptable range. In that case the EWALD summation method scales for a N particle system with $\mathcal{O}(N^{3/2})$.

2.3.2 The Model of Streit and Mintmire

Metals are as a rule found in nature as oxides. The pure metal is covered by oxide layers, which determine the adhesive properties of the real metal surfaces. For describing them in the MD simulation accurately, they have to be considered as *metal-oxide* systems. Essential for such combined systems is the correct treatment of the charge distribution on the metal-oxide interface. The valences of the metal atoms increase from zero to a finite value as one approaches the interface from the pure metal side. To model this change different methods have been developed, among them the one of Streit and Mintmire (SM) [78]. Firstly introduced for the aluminium-alumina system it allows a dynamic charge transfer between the atoms, since their charge values are supposed to be variable.

Electrostatic Energy

A description of the total electrostatic energy of an array of atoms as a function of atomic charges (valences) and position is needed. At first, the energy of a neutral atom i is expanded to second order as a TAYLOR series in the partial charge q_i :

$$E_i(q_i) = E_i(0) + \chi_i^0 q_i + \frac{1}{2} J_i^0 q_i^2, \quad (2.42)$$

where $\chi_i^0 = \partial E_i / \partial q_i$ denotes the *electronegativity*. It specifies how the energy varies, if the value of the charge changes. The second order term

J_i^0 is named as *atomic hardness* or *self-COULOMB repulsion*. For a set of N interacting atoms with total atomic charges q_i the electrostatic energy can be written as the sum of the single energies E_i :

$$E_{\text{es}} = \sum_{i=1}^N E_i(q_i) + \frac{1}{2} \sum_{i=1}^N \sum_{j \neq i=1}^N V_{ij}(\mathbf{r}_{ij}; q_i, q_j), \quad (2.43)$$

with the electrostatic or COULOMB pair interaction:

$$V_{ij}(\mathbf{r}_{ij}; q_i, q_j) = \int d^3 \mathbf{r}_1 \int d^3 \mathbf{r}_2 \frac{\rho_i(\mathbf{r}_1; q_i) \rho_j(\mathbf{r}_2; q_j)}{r_{12}}. \quad (2.44)$$

According to the suggestion of Rappé and Goddard [63], SM take for the atomic charge density ρ_i the distribution of a nuclear point charge plus an additional radial distribution, given by the function $f_i(\mathbf{r} - \mathbf{r}_i)$:

$$\rho_i(\mathbf{r}; q_i) = \mathcal{Z}_i \delta(\mathbf{r} - \mathbf{r}_i) + (q_i - \mathcal{Z}_i) f_i(\mathbf{r} - \mathbf{r}_i). \quad (2.45)$$

Only the valences are considered, so that \mathcal{Z}_i is equal to an *effective core charge* with $0 < \mathcal{Z}_i < Z_i$, where Z_i indicates the total nuclear charge of atom i . f_i takes the form of an exponential, since it is assumed to describe the atomic charge distribution of a spherically symmetric $1s$ orbital:

$$f_i(|\mathbf{r} - \mathbf{r}_i|) = \frac{\zeta_i^3}{\pi} e^{-2\zeta_i |\mathbf{r} - \mathbf{r}_i|}. \quad (2.46)$$

Inserting the expression of ρ_i into Eq. (2.44) and carrying out the integration leads to the final form of the electrostatic energy:

$$E_{\text{es}} = E_0 + \sum_{i=1}^N \chi_i q_i + \frac{1}{2} \sum_{i=1}^N \sum_{j=1}^N \tilde{V}_{ij} q_i q_j, \quad (2.47)$$

with the electronegativity:

$$\chi_i = \chi_i^0 + \sum_{j \neq i} Z_j \{ [j|f_i] - [f_i|f_j] \}, \quad (2.48)$$

and the interaction matrix \tilde{V}_{ij} :

$$\tilde{V}_{ij} = \begin{cases} J_i^0, & i = j \\ [f_i|f_j], & i \neq j. \end{cases} \quad (2.49)$$

$[j|f_i]$ and $[f_i|f_j]$ are short cuts for the solutions of the *nuclear attraction integral*:

$$[j|f_i] = \int d^3\mathbf{r}_1 \frac{f_i(\mathbf{r}_1 - \mathbf{r}_i)}{|\mathbf{r}_1 - \mathbf{r}_j|}, \quad (2.50)$$

and the COULOMB *repulsive integral*:

$$[f_i|f_j] = \int d^3\mathbf{r}_1 \int d^3\mathbf{r}_2 \frac{f_i(\mathbf{r}_1 - \mathbf{r}_i) f_j(\mathbf{r}_2 - \mathbf{r}_j)}{r_{12}}. \quad (2.51)$$

The corresponding expressions of this potentials as a function of r_{ij} are listed in App. B. Both contain the $1/r_{ij}$ long-range term. In Eq. (2.48) it is to be omitted, because of the difference of the two potentials, while for the non-diagonal parts of \tilde{V}_{ij} it has been treated by the summation method of EWALD [25]. χ_i^0 is now the initial electronegativity. The energy E_0 depends only on the nuclear coordinates of the atoms, not on their charges q_i .

Minimization of the Electrostatic Energy

The physically correct charge values q_i are those, which minimize the electrostatic energy E_{es} from Eq. (2.47). This is mathematically equivalent to solving the following system of linear equations:

$$\sum_{j=1}^N \tilde{V}_{ij} q_j = \mu - \chi_i. \quad (2.52)$$

A LAGRANGE multiplier μ has been introduced to ensure the constraint of net-charge neutrality:

$$\sum_{i=1}^N q_i = 0. \quad (2.53)$$

At the same time this condition implies a global equalization of the μ , which is identical to the electrostatic chemical potential of the charged system. It will be then equal for all atoms at the minimum of E_{es} :

$$\mu = \mu_i = \frac{\partial E_{\text{es}}}{\partial q_i}. \quad (2.54)$$

A corresponding charge transfer will occur between the atoms. In the work of SM the charge values q_i are obtained by inversion of the matrix \tilde{V}_{ij} :

$$q_i = \sum_{j=1}^N \tilde{V}_{ij}^{-1} (\mu - \chi_i). \quad (2.55)$$

By applying the summation from Eq. (2.53) on this expression, μ results as:

$$\mu = \sum_{i,j} \tilde{V}_{ij}^{-1} \chi_j / \sum_{i,j} \tilde{V}_{ij}^{-1}. \quad (2.56)$$

Executing MD simulations with this model of SM for alumina or pure aluminium firstly requires the implementation of the above charge optimization procedure. The charges will be adjusted every n MD steps. Choosing n right primarily depends on how strongly the interatomic distances and thus $\chi_i(r_{ij})$ and $\tilde{V}_{ij}(r_{ij})$ change between each charge update. Typical values of n are in the range from 5 to 10. In addition to the electrostatic energy, a force field has to be introduced, which is able to describe the atomic interactions in this oxide system correctly. This is especially the case for pure aluminium, where no contributions from electrostatics occur.

Non-Electrostatic Energy

For the non-electrostatic interactions in α -alumina and pure aluminium SM proposed an EAM potential, as it is given by Eqs. (2.7) and (2.8). A simple pair potential is in general not able to warrant the physical properties of a metal-oxide system. The pair part is suggested to take the form:

$$\phi_{ij}(r_{ij}) = 2B_{ij} e^{-\beta_{ij}/2(r_{ij}-r_{ij}^*)} - C_{ij} [1 + \alpha_{ij}(r_{ij} - r_{ij}^*)] e^{\alpha_{ij}(r_{ij}-r_{ij}^*)}, \quad (2.57)$$

while for the embedding energy a function of the Finnis-Sinclair type is chosen:

$$F_i(n_i) = -A_i \sqrt{\frac{n_i}{\xi_i}}. \quad (2.58)$$

The electron transfer $\rho_j(r_{ij})$ between atom i and j is well described by an exponential. By adding the contributions of all atoms $j \neq i$ the local electron density n_i of atom i follows:

$$n_i = \sum_{j \neq i} \rho_j(r_{ij}) = \sum_{j \neq i} \xi_j e^{-\beta_j(r_{ij}-r_j^*)}. \quad (2.59)$$

The parameters B_{ij} , β_{ij} , r_{ij}^* , C_{ij} , α_{ij} , A_i and ξ_i depend only on the species of the atoms i and j and are listed in the article of SM [78].

Force Computation

The effective potential in Eq. (2.2) is identical to the total potential energy of the corresponding system. In this model of SM the total potential energy named as E_{tot} is the sum of electrostatic and non-electrostatic part:

$$E_{\text{tot}} = E_{\text{es}}(\mathbf{q}(\mathbf{r}), \mathbf{r}) + E_{\text{EAM}}(\mathbf{r}), \quad (2.60)$$

with E_{EAM} being the EAM potential energy. The force on atom i follows from the spatial derivative of E_{tot} :

$$\begin{aligned} -F_{ix} = \frac{dE_{\text{tot}}}{dx_i} &= \sum_{j=1}^N \frac{\partial E_{\text{es}}}{\partial q_j} \frac{\partial q_j}{\partial x_i} + \frac{\partial E_{\text{es}}}{\partial x_i} + \frac{\partial E_{\text{EAM}}}{\partial x_i}, \\ (2.54) \quad &= \mu \frac{\partial}{\partial x_i} \sum_{j=1}^N q_j + \frac{\partial E_{\text{es}}}{\partial x_i} + \frac{\partial E_{\text{EAM}}}{\partial x_i}, \\ (2.53) \quad &= \frac{\partial E_{\text{es}}}{\partial x_i} + \frac{\partial E_{\text{EAM}}}{\partial x_i}, \end{aligned} \quad (2.61)$$

illustrated here for the x component. Because of the charge neutrality condition the spatial derivative of the charges, which is usually difficult to determine, has no effect on the force computation.

The force contributions, which arise from the electrostatic energy E_{es} can be separated into two parts, concerning the gradients of the potentials of nuclear attraction and COULOMB repulsion:

$$\mathbf{F}_{\text{es}} = \mathbf{F}_{\text{na}} + \mathbf{F}_{\text{cr}}. \quad (2.62)$$

They are explicitly given by the expressions:

$$F_{ix}^{\text{na}} = - \sum_{j \neq i} \left\{ Z_j q_i \frac{\partial}{\partial x_i} [j|f_i] + Z_i q_j \frac{\partial}{\partial x_i} [i|f_j] \right\}, \quad (2.63)$$

and

$$F_{ix}^{\text{cr}} = - \sum_{j \neq i} \left\{ -Z_j q_i - Z_i q_j + q_i q_j \right\} \frac{\partial}{\partial x_i} [f_i|f_j]. \quad (2.64)$$

As it has been already mentioned for the electronegativity from Eq. (2.48), the long-range term $1/r_{ij}$ appears also in \mathbf{F}_{es} only once and is handled as well by the EWALD method presented in detail in the previous section.

Note, that since in this work the original notation of SM (GAUSSIAN units) is used, for SI-units the factor $e^2/4\pi\epsilon_0 = 14.4\text{eV}\text{\AA}$ is missing at the potentials $[i|f_j]$ and $[f_i|f_j]$. For getting the correct SI-units of E_{es} and thus the correct charge values in the simulation, it has to be added, when implementing this model.

2.3.3 Beyond Streitz and Mintmire

The model of SM was one of the first variable charge models making MD simulations of oxides possible. Since 1994 this approach has been used in many cases and for different applications, mainly for studying the oxidation of aluminium. Starting from alumina, it has been later applied also to other oxide systems, like zirconia or titania, requiring the creation of the corresponding interaction potentials. At the same time this model showed some drawbacks, so that extensions of the original SM approach were necessary. The major improvements of the last years are discussed here.

At first, the problems are mentioned, which can occur in the simulation with charge optimization. Since there is no restriction concerning the valences, non-physical values can arise. As a consequence, the interaction between the atoms can become stronger, the interatomic distances shorter and finally the simulated system unstable.

Second, the model of SM is only applicable to oxides with one single metal, not to an oxygen-more metal system. Thus, for a pure metal alloy the charges are not predicted correctly. Their values will differ from zero.

The third problem is the minimization process itself. Since it is a global minimization, for the calculation of the charges each atom is taken into account, also each metallic one. Especially for systems with a large number of particles, this global charge optimization causes a significant computational effort.

Additionally, the potential energy is always reduced at each minimization step. Hence, the total energy of the system decays over time. This is a general problem of all kinds of minimization processes [91]. The missing energy part is balanced by the thermostat or barostat if running a NVT or NPT simulation. However, in case of a NVE simulation the energy is not conserved and the system normally shows an instability.

For all the problems listed above different solutions have been proposed. Zhou *et al.* suggested a different form of the electrostatic energy for avoiding the charge instability [92]. Since E_{es} is also called as *charge transfer ionic potential* (CTIP), his model was named as *modified CTIP*.

Modified CTIP

The values of the valences can be kept in a physical reasonable range by introducing a lower and an upper bound for them. This is realized in the charge optimization process by adding two more terms to the original electrostatic energy $E_{\text{es}}^{\text{SM}}$ from Eq. (2.47):

$$E_{\text{es}}^{\text{Zhou}} = E_{\text{es}}^{\text{SM}} + \sum_{i=1}^N \omega \left(1 - \frac{q_i - q_{\min,i}}{|q_i - q_{\min,i}|} \right) (q_i - q_{\min,i})^2 + \sum_{i=1}^N \omega \left(1 - \frac{q_i - q_{\max,i}}{|q_i - q_{\max,i}|} \right) (q_i - q_{\max,i})^2. \quad (2.65)$$

The bounds are given by $q_{\min,i}$ and $q_{\max,i}$. Each charge value q_i has to satisfy the constraint $q_{\min,i} < q_i < q_{\max,i}$. This is controlled by the *penalty coefficients* ω . They determine how strong the charge is bounded. Physically it is equal to an energy penalty. Metal atoms do usually not receive electrons or lose them from the inner-shells, just as oxygen atoms do not emit electrons or obtain more than two of them.

Two of the main problems of the original SM model, the charge instability and all its implications along with non-vanishing charge values in the heterogeneous metallic regions can be avoided by this at first view slight modification of the electrostatic energy. Looking at the minimization of $E_{\text{es}}^{\text{Zhou}}$ concretely, one will realize, that a non-linear system of equations results. The additional computational cost is high, essentially for systems with a large number of atoms. The question thus arises if the above enhancement is really necessary, since in the most cases the charges take physically reasonable values and the other problems of the SM model still remain unsolved with this modified CTIP. Therefore, it has not been included, when implementing the SM model in IMD.

Embedded Ion Method

Zhou proposed also an alternative model for the energy reduction problem [91]. The atomic valences q_i are not determined directly by a minimization process, but depend on the local ionic environment, which is characterized by the quantity σ , called *ion propensity*. This is an approach similar to the EAM potential from Sec. 2.2. By embedding an atom into an arrangement of ions a certain amount of energy is released. The sum of all of this embedding energies $E_{\text{emb},i}$ is equal to the electrostatic energy of the system:

$$E_{\text{es}} = \sum_{i=1}^N E_{\text{emb},i}(\sigma_i). \quad (2.66)$$

Looking at the embedding energies F_i of the EAM potential, it is obvious, that the quantity σ plays the same role in this model as the electron density n there. Also adding the non-electrostatic pair interactions to the above expression, the total energy is written in this *embedded ion method* (EIM) as

$$E_{\text{EIM}} = \frac{1}{2} \sum_{\substack{i,j \\ i \neq j}} \phi_{ij}(r_{ij}) + \sum_i E_{\text{emb},i}(\sigma_i). \quad (2.67)$$

For the desired charge values, denoted here with p_i , $E_{\text{emb},i}$ has to be minimized only once:

$$\left. \frac{\partial E_{\text{emb},i}}{\partial q_i} \right|_{q_i=p_i} = 0, \quad (2.68)$$

obtaining the relation:

$$p_i = -\frac{\sigma_i}{J_i^0}, \quad (2.69)$$

with J_i^0 being the self-COULOMB repulsion from Eq. (2.42).

Also for this model Zhou assumed bounds for the charges. p_i is therefore rescaled to a new equilibrium charge $q_{i,0}$, which is within the range of $q_{\text{min},i}$ and $q_{\text{max},i}$. Thus, not only the energy conservation problem is solved by EIM, but also the drawbacks of the SM model, which have been handled by the modified CTIP mentioned before. Unfortunately, the EIM potential was originally developed for the La-Br system and has not been transferred to other systems like oxides yet. That is the main reason, why it has found a limited application until now.

Local Chemical Potential

At the dilute oxygen limit a different approach concerning the problem of global minimization has been chosen by Elsener *et al.* [22, 23]. Only the charges of those atoms are optimized, which are supposed to be ionic. This means for a oxide system with a dilute concentration of oxygen atoms, that only those metal atoms are considered, which are at a spatial region around the single O-atoms. Typically, this sub-region is a sphere of radius R_o . Since the charge neutrality condition has to be satisfied within R_o , local LAGRANGE multipliers are introduced, defining a *local chemical potential* (LCP). In summary, this alternative optimization takes the form:

$$\min \sum_i \chi_i q_i + \frac{1}{2} \sum_{i,j} \tilde{V}_{ij} q_i q_j \quad \text{subject to} \quad \begin{cases} \sum_i q_i = 0 & \forall \text{ sub-regions } o, \\ q_b = 0 & b \in \{\text{buffer region}\}, \end{cases} \quad (2.70)$$

with the Eqs. (2.47) and (2.53) being now valid locally. The buffer region ends at the radius R_b and is the annulus between both radii R_o and R_b . The charge values of the metal atoms beyond R_b are set to zero from the beginning and are excluded from the optimization process, avoiding charge fluctuations in the pure metallic regions.

Since the above linear system of equations is solved locally, the computational effort scales with the number of O-atoms. This makes the LCP approach an efficient method not for usual oxides, but only for dilute systems. In that case one order of magnitude of computational time can be saved. An additional saving can be achieved, if a direct summation instead of the EWALD method is applied.

Dynamic Charge Transfer Bond Order Potential

Another charge transfer model is the one by Albe *et al.* called *dynamic charge transfer bond order potential* (DCT-BOP) [1]. The main idea is, that charge is only transferred between nearest neighbours, more precisely, between two atoms, which are connected by a bond. Depending on the distance of both atoms and on their electronegativity, each atom receives that amount of charge, which was released by the other one. If the atoms are from the same type no charge is transferred. This symmetric charge transfer involves charge neutrality and is described by an anti-symmetric

function $\rho(r_{ij}) = -\rho(r_{ji})$:

$$\rho(r_{ij}) = A e^{-\frac{r_{ij}-r_c}{\lambda}-1} (\delta_{m_i m_j} - 1)^{m_i}. \quad (2.71)$$

From the adjustable parameters A , r_c and λ , the transfer is limited by r_c . Each atom is indexed by the integer m , which is for cations even and for anions odd. Whether a charge transfer occurs or not, is controlled by the KRONECKER delta $\delta_{m_i m_j}$. For the electronegativity of the local environment a function P_{ij} is introduced:

$$P_{ij} = \left(1 + \sum_{k \neq i, j} \frac{\rho(r_{ik})}{\rho(r_{ij})} \right)^{-\frac{1}{2n}}, \quad (2.72)$$

with n being an additional parameter. The charges are weighted by this function and follow as

$$q_i = \sum_{j \neq i} \frac{P_{ij} + P_{ji}}{2} \rho(r_{ij}), \quad (2.73)$$

depending here on the interatomic distances. Thus, the force calculation becomes much more difficult and quite time consuming, since the additional force contributions are handled together with the long-range interactions via neighbour lists in a complex way. A specific feature of this model is that the energy is conserved, because no minimization is done. Furthermore, compared to the previous models the forces are adjusted in this DCT-BOP in a self-consistent manner. Unfortunately, this model also has not been developed for an oxide system, but for gallium nitride (GaN), making it for our simulations less attractive.

Charge Optimized Many-Body Potential

The last enhancement of the original SM model is the *charge optimized many-body* (COMB) potential proposed by Yu *et al.* [90]. Out of all the previous models shown until now, it is the most suitable one for the applications of this thesis, since it has been developed for oxide systems and interface structures [21, 68, 69].

The main difference of this method is that for the charge determination

no minimization is executed, but a LAGRANGian approach is applied, solving in such a manner the energy conservation problem. The charge values are assumed to be time-dependent, just as the spatial coordinates \mathbf{r}_i and velocities $\dot{\mathbf{r}}_i$ of the atoms. An additional dynamic quantity also implies an extra contribution to the kinetic energy T of the system:

$$T = \frac{1}{2} \sum_i m_i \dot{r}_i^2(t) + \frac{1}{2} \sum_i s_i \dot{q}_i^2(t), \quad (2.74)$$

where s_i specifies how inertially the charge of the atom i changes. From the LAGRANGian $L = T - E_T$ with E_T being the total energy of the system the EULER-LAGRANGE equations can be derived:

$$m_i \ddot{r}_i = - \frac{\partial}{\partial r_i} E_T (\{r_i\}, \{q_i\}), \quad (2.75)$$

$$s_i \ddot{q}_i = \frac{\partial}{\partial q_i} E_T (\{r_i\}, \{q_i\}). \quad (2.76)$$

For the solution of these generalized equations of motion a standard VERLET approach can be used, as it has been already suggested for the Eqs. (2.3) and (2.4). Without any matrix operation the computational effort of this model scales with $\mathcal{O}(N)$. This is essential especially for the simulation of systems with large particle numbers N . At each time step δt the charges will adjust their values according to the constraint of net-charge neutrality:

$$\sum_{i=1}^N q_i = 0, \quad (2.77)$$

satisfying at the new time $t_0 + \delta t$ the condition of equal chemical potential μ for all atoms. From the definition of μ given by Eq. (2.54):

$$\mu_i = \frac{\partial E_T}{\partial q_i}, \quad (2.78)$$

the above electronegativity equalization condition can be formulated as

$$\mu_i = \bar{\mu} = \frac{1}{N} \sum_i \mu_i, \quad (2.79)$$

where $\bar{\mu}$ is the average chemical potential of the system. Thus, the dynamic evolution of the charges can be expressed by the equation:

$$-m_q \ddot{q}_i = \mu_i - \bar{\mu}, \quad (2.80)$$

with the inertia being equal for all atoms: $s_i = m_q$. The interpretation of this equation is that the force $\mu_i - \bar{\mu}$ will cause a charge transfer between the atoms until the equalization of $\bar{\mu}$ is completed. Similar to the usual equations of motion an obvious modification of the original LAGRANGIAN approach would be to introduce a damping parameter η_d :

$$-m_q \ddot{q}_i = \mu_i - \bar{\mu} + \eta_d \dot{q}_i, \quad (2.81)$$

which helps the charges to converge faster to their right values and makes the system also more resistant against instabilities. However, as a consequence of η_d the total energy is not conserved any more during the simulation.

In addition to the different charge transfer models, which have been discussed so far, also the effective potentials for the system one is interested for have to be created. As already mentioned, the COMB potential is the only one developed for oxide systems. It is a Tersoff potential [83] involving charge optimization, as the name *charge optimized many-body* potential implies. Firstly suggested by Yasukawa [89] the total energy in this potential model takes the form:

$$E_T = \sum_i E_i = \sum_i \left[E_i^S + \frac{1}{2} \sum_{j \neq i} V_{ij}(r_{ij}; q_i, q_j) \right], \quad (2.82)$$

where E_i^S is the self-energy of atom i from Eq. (2.42):

$$E_i^S(q_i) = \chi_i^0 q_i + \frac{1}{2} J_i^0 q_i^2. \quad (2.83)$$

The interaction matrix V_{ij} is now split into a repulsive part U_{ij}^R , into a short-range attractive potential U_{ij}^A , into a ionic bond energy U_{ij}^I and into a energy contribution U_{ij}^V , which arises from the VAN DER WAALS interaction between the atoms i and j :

$$V_{ij}(r_{ij}; q_i, q_j) = U_{ij}^R + U_{ij}^A + U_{ij}^I + U_{ij}^V. \quad (2.84)$$

In the article of Yasukawa these energy contributions are given as:

$$U_{ij}^R(r_{ij}) = f_{s_{ij}} A_{ij} e^{-\lambda_{ij} r_{ij}}, \quad (2.85)$$

$$U_{ij}^A(r_{ij}; q_i, q_j) = -f_{s_{ij}} b_{ij} B_{ij} e^{-\alpha_{ij} r_{ij}}, \quad (2.86)$$

$$U_{ij}^I(r_{ij}; q_i, q_j) = f_{L_{ij}} \eta_i \eta_j \frac{q_i q_j}{4\pi\epsilon_0 r_{ij}}, \quad (2.87)$$

$$U_{ij}^V(r_{ij}) = f_{L_{ij}} \frac{(C_{VDW_i} C_{VDW_j})^{1/2}}{r_{ij}^6}, \quad (2.88)$$

with all parameters also listed and explained in detail there. This kind of potential includes many-body interactions just as the original one of Tersoff. Hence, COMB is suitable for the investigation of chemical problems by MD, since in addition to the charge optimization it allows the creation and breaking of bonds while the simulation is running. Besides the reactive force field (ReaxFF) methods this makes it a powerful tool for reactive MD. Unfortunately, compared to pair potentials the simulation time increases in case of many-body interactions by about two orders of magnitude.

The implementation of the COMB potential is a demanding task and rather complicated. For the simulations with COMB the software package LAMMPS (large-scale atomic molecular massively parallel simulator) [60] can be used, since the Yasukawa potential has been implemented successfully there.

Reactive Force Field

The ReaxFF method [13, 86] should be also presented here. It is a force field created for describing reactive processes. Bonds can break and formed during the MD simulation. Its total system energy splits into following parts:

$$\begin{aligned} E_{\text{ReaxFF}} = & E_{\text{self}} + E_{\text{Coul}} + E_{\text{vdW}} + E_{\text{angle}} + E_{\text{torsion}} + E_{\text{conjugation}} \\ & + E_{\text{H-bond}} + E_{\text{bond}} + E_{\text{Ione-pair}} + E_{\text{over}} + E_{\text{under}} + E_{\text{others}}. \end{aligned} \quad (2.89)$$

For different charge states of an atom the self-energy E_{self} is introduced, while the electrostatic attraction and repulsion between ions is given by E_{Coul} . In case of nonbonded atoms the VAN DER WAALS energy E_{vdW} is relevant. E_{angle} and E_{torsion} are energies, which follow from valence and

torsion angle distortion. The three- and four-body conjugation is captured by $E_{\text{conjugation}}$. For systems with polar molecules $E_{\text{H-bond}}$ describes the hydrogen bonds, which arise from the weak X-H-X interaction. However, much more complicate bond-order is incorporated in E_{bond} . The number of valence electrons around an atom is also included in ReaxFF by the three energy terms $E_{\text{Ione-pair}}$, E_{over} and E_{under} . Other energy contributions to describe C_2 species, allene-type and triple-bond are contained within E_{others} . If the bond dissociates all above energy terms vanish, except the COULOMB and VAN DER WAALS energy. The ReaxFF is able to describe with these many-body potentials covalent, partially or completely ionic systems. For a more detailed explanation see [48, 71].

Conclusion

Most of the enhancements of the original version of the SM model shown in this section have not been developed for oxides (EIM, DCT-BOP) and are not efficient enough for large-scale simulations, as the modified CTIP, since a non-linear system of equation has to be solved. In case of the LCP only dilute oxygen systems have been regarded. What kind of developments have been realized, when implementing the SM model in IMD will be discussed extensively in the next chapter.

Parallel to all of these charge optimization procedures and modifications of the SM model an alternative method for the simulation of oxide systems, the model of Tangney and Scandolo (TS), was pursued and implemented also in IMD [96]. The charges are not optimized during the simulation. They are treated as point charges, while their values do usually not correspond to the valences of the system. The main focus in this approach is on the dipoles of the oxygen atoms.

2.3.4 The Model of Tangney and Scandolo

Oxide systems are not only described in the simulation correctly by including the electrostatics of charges, but also if the polarizability of the oxygen atoms is taken into account. Tangney and Scandolo suggested a model, which allows each oxygen atom to be polarizable and to have a dipole moment [81]. The charges are kept fixed. In addition to the COULOMB potential, charge-dipole and dipole-dipole interactions arise. Their long-range behavior is also handled by the EWALD summation method. For

the short-range pair interactions of the ions a MORSE-stretch potential is assumed:

$$U_{ij} = D_{ij} \left\{ e^{\gamma_{ij} [1 - (r_{ij}/r_{ij}^0)]} - 2 e^{\gamma_{ij}/2 [1 - (r_{ij}/r_{ij}^0)]} \right\}. \quad (2.90)$$

The dipole moments of the oxygen atoms are computed iteratively in a self-consistent manner, since the electric field, which induces them, in turn depends on all charges and dipole moments. For the atom i at the iteration step n the dipole moment \mathbf{p}_i^n is splitted into a short-range and induced part:

$$\mathbf{p}_i^n = \mathbf{p}_i^{\text{sr}} + \mathbf{p}_i^{\text{ind}}. \quad (2.91)$$

\mathbf{p}_i^{sr} is caused by the local charges and takes the form:

$$\mathbf{p}_i^{\text{sr}} = \alpha \sum_{j \neq i} \frac{q_j \mathbf{r}_{ij}}{r_{ij}^3} f_{ij}(r_{ij}), \quad (2.92)$$

with α being the polarizability and the function f_{ij} modelling the short-range repulsive interaction:

$$f_{ij}(r_{ij}) = c \sum_{k=0}^4 \frac{(b r_{ij})^k}{k!} e^{-b r_{ij}}. \quad (2.93)$$

The induced contribution $\mathbf{p}_i^{\text{ind}}$ results from the electric field \mathbf{E} of all N dipole moments and charges at the atomic position \mathbf{r}_i :

$$\mathbf{p}_i^{\text{ind}} = \alpha \mathbf{E} \left(\mathbf{r}_i; \left\{ \mathbf{p}_j^{n-1} \right\}_{j=1, N}, \left\{ \mathbf{r}_j \right\}_{j=1, N} \right). \quad (2.94)$$

\mathbf{E} is calculated by extrapolation of an initial value of the electric field \mathbf{E}^0 from the previous three time steps. At each MD step so many iterations of Eq. (2.91) are done, that the value of \mathbf{p}_i^n converges. Convergence means that \mathbf{p}_i^n slightly differs from the dipole moment of the previous iteration step, being within the allowed tolerance.

The potential model of TS was first developed for silica. By use of the tool `potfit` it has been also extended on the systems of magnesia and alumina [6, 34]. The parameters D_{ij} , γ_{ij} , r_{ij}^0 , q_j , α , b and c had to be optimized for this purpose on reference structures of these oxides. For the implementation of TS in `potfit` and also in `IMD` the same improvements have been realized, as for the SM model, namely applying the summation method of Wolf instead of EWALD. This development is one of the main topics of the next chapter.

Chapter 3

Methodological Progresses

Some of the approaches from Sec. 2.3.3 (CTIP and LCP) use the conjugate gradient method for determining the valence charges. When implementing the SM model in IMD this iterative solver has been also applied for the system of linear equations given by Eq. (2.52). Its mathematical concept is illustrated compactly [70].

The second improvement is a different treatment of the long-range interactions as presented in Sec. 2.3.1. For metal oxides the reciprocal space part of the EWALD sum can be neglected, since in such systems the charges screen each other. Thus, the summation is carried out only in direct space and periodic boundary conditions are not necessary any more. The main advantage of this reduced summation method called Wolf summation is that it scales linearly with the number of particles N [88]. By handling the long-range terms in the model of SM with Wolf, not only computing time for the force calculation can be saved, but also during the charge optimization. For the COMB potential the Wolf summation method has been applied [21, 68], too, which is an additional reason to present this technique in this chapter in detail.

In the same way as for the charges, the Wolf summation has been transferred to dipole interactions [96]. How this development of the original TS model affects the MD simulations with silica is also discussed in this chapter.

As it has been specified in Sec. 2.3.2, in the model of SM the total energy consists of the contributions of the electrostatic energy and a non-electrostatic potential. For the latter one SM suggested an EAM potential, which had been firstly fitted on alumina [78]. Since one simulation goal of this work had been the investigation of how oxides behave under mechanical loads, the potential of SM had been aimed to be able to describe the material failure caused by cracks correctly. However, by performing simulations with this EAM potential it turned out that the surface relaxation

of bulk alumina provided inadequate results for crack propagation. Also interface structures of alumina and pure aluminium become instable during the simulation. Therefore, as an alternative force field the TS potential was considered, since it has been made applicable also for the systems of magnesia and alumina [6, 34]. But this requires the combination of the two methods of SM and TS, involving some modifications of the original models which are also topic of this chapter.

3.1 Iterative Solvers

For the minimization of the electrostatic energy E_{es} given by Eq. (2.47) a system of linear equations has to be solved iteratively. Iterative methods provide approximate solutions, approaching the exact solution by an algorithm step by step. In this kind of solvers the specific form of the matrix, which describes the system, is taken regard of. Especially for dense matrices this means a significant saving in memory and computing time [56]. Looking at E_{es} as a function of the charges q_i , the minimization of a quadratic form has to be realized.

3.1.1 Minimization of a Quadratic Form

A quadratic form

$$f(\mathbf{x}) = \frac{1}{2} \mathbf{x}^t \mathbf{A} \mathbf{x} - \mathbf{b}^t \mathbf{x} + c, \quad (3.1)$$

is minimized by the solution to $\mathbf{A} \mathbf{x} = \mathbf{b}$, if \mathbf{A} is symmetric and positive-definite. The main idea is to take specific *search directions* $\mathbf{u}_0, \mathbf{u}_1, \dots \in \mathbb{R}^n \setminus \{\mathbf{0}\}$ for finding the global minimum \mathbf{x} . Starting from an arbitrary point \mathbf{x}_0 the minimum of f is approached along the line

$$\mathbf{x}_1 = \mathbf{x}_0 + \alpha_0 \mathbf{u}_0. \quad (3.2)$$

α_0 specifies how big the step in direction of \mathbf{u}_0 should be until reaching the new local minimum \mathbf{x}_1 . The values of f along this line are given by $f(\mathbf{x}_1) = f(\mathbf{x}_0 + \alpha_0 \mathbf{u}_0)$. Finding \mathbf{x}_1 means to minimize this function with

respect to α_0 :

$$\begin{aligned} \frac{df(\mathbf{x}_1(\mathbf{x}_0, \alpha_0))}{d\alpha_0} &= (\nabla f(\mathbf{x}_1))^t \frac{d\mathbf{x}_1}{d\alpha_0} \\ &\stackrel{(3.2)}{=} (\nabla f(\mathbf{x}_1))^t \mathbf{u}_0 \\ &= 0. \end{aligned} \quad (3.3)$$

Thus, the directional derivative has to be equal to zero. Since $\nabla f(\mathbf{x}_1) = \mathbf{A}\mathbf{x}_1 - \mathbf{b}$ the step size results with Eq. (3.2) as

$$\alpha_0 = \frac{(\mathbf{b} - \mathbf{A}\mathbf{x}_0)^t \mathbf{u}_0}{\mathbf{u}_0^t \mathbf{A} \mathbf{u}_0}. \quad (3.4)$$

This *line search* procedure is repeated for each iteration step $i = 0, 1, 2, \dots$ until one comes close enough to the global minimum. Only an initial value \mathbf{x}_0 and a set of search directions are needed. The general algorithm takes the form:

$$\mathbf{r}_i = \mathbf{b} - \mathbf{A}\mathbf{x}_i, \quad (3.5)$$

$$\alpha_i = \frac{\mathbf{r}_i^t \mathbf{u}_i}{\mathbf{u}_i^t \mathbf{A} \mathbf{u}_i}, \quad (3.6)$$

$$\mathbf{x}_{i+1} = \mathbf{x}_i + \alpha_i \mathbf{u}_i, \quad (3.7)$$

where the vector \mathbf{r} is defined as *residual*. The problem is how to choose the search directions \mathbf{u}_i .

The Method of Steepest Descent

Since one looks for the global minimum of f , the most intuitive approach is to step from each point \mathbf{x}_i to the direction of steepest descent. In this case the search directions are identical to the residuals:

$$\mathbf{u}_i = -\nabla f(\mathbf{x}_i) = -(\mathbf{A}\mathbf{x}_i - \mathbf{b}) = \mathbf{r}_i. \quad (3.8)$$

The directional derivative in Eq. (3.3) then becomes:

$$(\nabla f(\mathbf{x}_{i+1}))^t \mathbf{r}_i = 0, \quad (3.9)$$

and determines not only the position of the local minimum \mathbf{x}_{i+1} on the line, but also the new search direction $\mathbf{r}_{i+1} = -\nabla f(\mathbf{x}_{i+1})$. It has to be

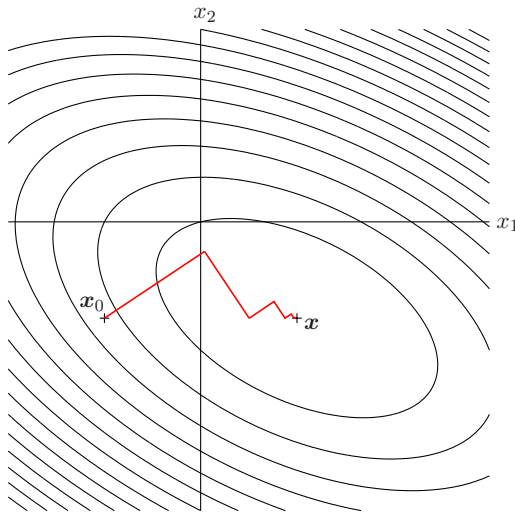


Figure 3.1: The method of steepest descent for a quadratic form in two dimensions. The isocontours around the global minimum \mathbf{x} are illustrated. From the initial point \mathbf{x}_0 a zigzag path to \mathbf{x} results.

orthogonal to the previous one. Modifying the general algorithm for this special search directions, the *method of steepest descent* follows:

$$\mathbf{r}_i = \mathbf{b} - \mathbf{A}\mathbf{x}_i, \quad (3.10)$$

$$\alpha_i = \frac{\mathbf{r}_i^t \mathbf{r}_i}{\mathbf{r}_i^t \mathbf{A} \mathbf{r}_i}, \quad (3.11)$$

$$\mathbf{x}_{i+1} = \mathbf{x}_i + \alpha_i \mathbf{r}_i. \quad (3.12)$$

The iteration is stopped, if $\mathbf{r}_i = 0$. Then, the minimum \mathbf{x} is reached and the system is solved. The computational effort of the two matrix-vector products above can be reduced, if Eq. (3.12) is premultiplied by $-\mathbf{A}$ and the vector \mathbf{b} is added. The result takes the form:

$$\mathbf{r}_{i+1} = \mathbf{r}_i - \alpha_i \mathbf{A} \mathbf{r}_i, \quad (3.13)$$

where only one matrix-vector multiplication remains. Nevertheless, Eq. (3.10) still is required for calculating the initial residual \mathbf{r}_0 . A resulting path to the minimum via this method of steepest descent is shown in Fig. 3.1. Also the main drawback can be seen there. One is moving for several times to the same direction. Therefore, the search directions have to be chosen in a more efficient way.

The Method of Conjugate Directions

The idea is to take only one step in each search direction \mathbf{u}_i . After n steps the minimum \mathbf{x} should be reached, where n is the dimension of the problem. Such a set of search directions can be found, if the minimization condition from Eq. (3.3):

$$\mathbf{r}_{i+1}^t \mathbf{u}_i = 0, \quad (3.14)$$

is reconsidered. Defining firstly the *error* as the difference between approximate and correct solution: $\mathbf{e}_i = \mathbf{x}_i - \mathbf{x}$, the residual is equal to $\mathbf{r}_i = -\mathbf{A}\mathbf{e}_i$. Above equation takes then the form:

$$\mathbf{u}_i^t \mathbf{A}\mathbf{e}_{i+1} = 0. \quad (3.15)$$

This is another interpretation of how to determine the minimum point along the line. The search direction and the error have to be at that point not orthogonal, but *A-orthogonal* or *conjugated*. Not to step to the same direction again, means to choose \mathbf{u}_{i+1} in direction of \mathbf{e}_{i+1} . Thus, the search directions have to be *A-orthogonal*:

$$\mathbf{u}_i^t \mathbf{A}\mathbf{u}_{i+1} = 0. \quad (3.16)$$

An immediate consequence of this orthogonality condition is, that the global minimum is hit after n steps. For the corresponding proof, the initial error \mathbf{e}_0 has to be expressed as a linear combination of the search directions:

$$\mathbf{e}_0 = \sum_{j=0}^{n-1} \beta_j \mathbf{u}_j. \quad (3.17)$$

Also the error at step i is built up by \mathbf{e}_0 and almost all \mathbf{u}_j :

$$\mathbf{e}_i = \mathbf{e}_0 + \sum_{j=0}^{i-1} \alpha_j \mathbf{u}_j. \quad (3.18)$$

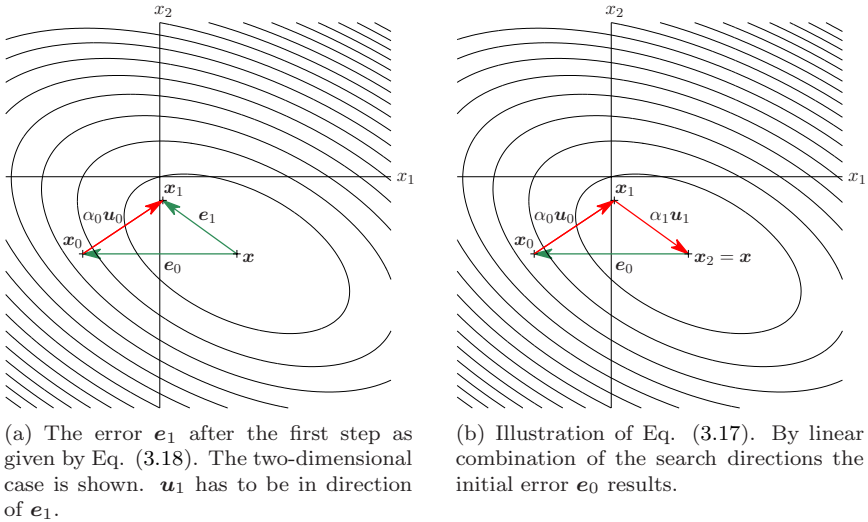


Figure 3.2: The choice and properties of \mathbf{A} -orthogonal search directions follow immediately by looking at the error terms.

For $n = 2$ these linear combinations are illustrated in Fig. 3.2. By premultiplying Eq. (3.17) by $\mathbf{u}_i^t \mathbf{A}$ only the coefficient β_i remains, since the search directions are \mathbf{A} -orthogonal:

$$\mathbf{u}_i^t \mathbf{A} \mathbf{e}_0 = \sum_{j=0}^{n-1} \beta_j \mathbf{u}_i^t \mathbf{A} \mathbf{u}_j = \beta_i \mathbf{u}_i^t \mathbf{A} \mathbf{u}_i. \quad (3.19)$$

Thus, β_i is given by the expression:

$$\beta_i = \frac{\mathbf{u}_i^t \mathbf{A} \mathbf{e}_i}{\mathbf{u}_i^t \mathbf{A} \mathbf{u}_i} \stackrel{(3.6)}{=} -\alpha_i, \quad (3.20)$$

where \mathbf{e}_0 has been replaced by \mathbf{e}_i according to Eq. (3.18). This can be done because of the \mathbf{A} -orthogonality of the \mathbf{u}_j . Using this result, Eq. (3.18) can

be written as

$$\begin{aligned}
 \mathbf{e}_i &= \mathbf{e}_0 + \sum_{j=0}^{i-1} \alpha_j \mathbf{u}_j \\
 &\stackrel{(3.17)}{=} \sum_{j=0}^{n-1} \beta_j \mathbf{u}_j - \sum_{j=0}^{i-1} \beta_j \mathbf{u}_j \\
 &= \sum_{j=i}^{n-1} \beta_j \mathbf{u}_j.
 \end{aligned} \tag{3.21}$$

It is obvious, that after each iteration step one component of the error term \mathbf{e}_i is eliminated. After n steps $\mathbf{e}_n = 0$ results and, as it has been predicted, the solution \mathbf{x} is reached (see Fig. 3.2).

Thus, to find the ideal set of search directions, \mathbf{A} -orthogonal vectors have to be created. This can be done in the same way as for generating orthogonal vectors from a set of n linear independent vectors $\mathbf{v}_0, \mathbf{v}_1, \dots, \mathbf{v}_{n-1}$ using a GRAM-SCHMIDT process. In this case a *conjugate* one is applied. The vector \mathbf{v}_i is split for all previous search directions into a conjugate and non-conjugate part, where the non-conjugate components are subtracted from \mathbf{v}_i . The remaining vector is the new search direction \mathbf{u}_i , which is then \mathbf{A} -orthogonal to all previous \mathbf{u} vectors. The corresponding equation takes the form:

$$\mathbf{u}_i = \mathbf{v}_i - \sum_{j=0}^{i-1} (\mathbf{v}_i^t \mathbf{A} \hat{\mathbf{u}}_j) \hat{\mathbf{u}}_j, \tag{3.22}$$

for $i > j$ and with the initial value $\mathbf{u}_0 = \mathbf{v}_0$. The non-conjugate parts of \mathbf{v}_i follow from the above inner product. They are parallel to the unit vector $\hat{\mathbf{u}}_j = \mathbf{u}_j / \|\mathbf{u}_j\|_{\mathbf{A}}$. The absolute value of \mathbf{u}_j is given in this \mathbf{A} -norm by $\|\mathbf{u}_j\|_{\mathbf{A}}^2 = \mathbf{u}_j^t \mathbf{A} \mathbf{u}_j$. From this definition a better understanding of the \mathbf{A} -orthogonality condition in Eq. (3.16) is gained. If two vectors are \mathbf{A} -orthogonal, then they are orthogonal in that space, which is scaled by the matrix \mathbf{A} . An appropriate illustration is given by Fig. 3.3. By defining GRAM-SCHMIDT coefficients λ_{ij} as

$$\lambda_{ij} = -\frac{\mathbf{v}_i^t \mathbf{A} \mathbf{u}_j}{\mathbf{u}_j^t \mathbf{A} \mathbf{u}_j}, \tag{3.23}$$

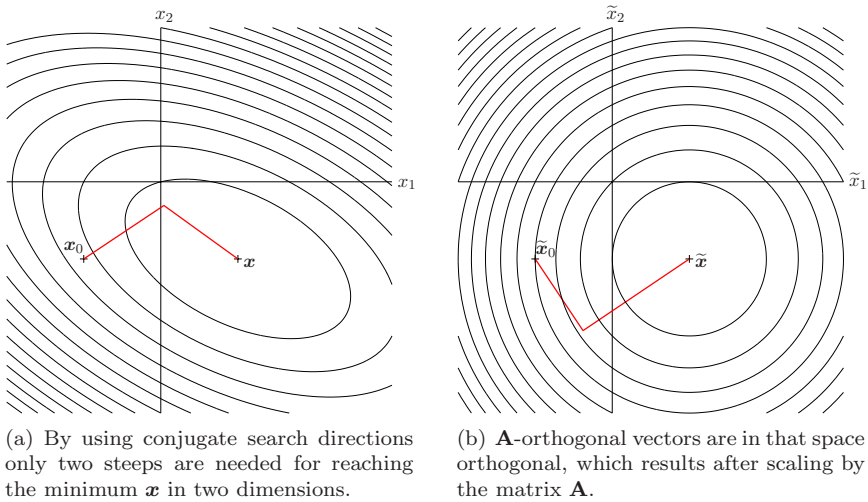


Figure 3.3: If the method of conjugate directions is applied, then at the same time the method of orthogonal directions is performed in a stretched space.

Eq. (3.22) becomes:

$$\mathbf{u}_i = \mathbf{v}_i + \sum_{j=0}^{i-1} \lambda_{ij} \mathbf{u}_j. \quad (3.24)$$

The main disadvantage of this conjugate GRAM-SCHMIDT process and also of the *method of conjugate directions* can be already seen in Eq. (3.22). All old search directions are needed and have to be stored for creating each new one. To generate a full set $\mathcal{O}(n^3)$ operations are required. The only way to reduce them, is to choose a special set of n linear independent vectors for the \mathbf{v}_i .

The Method of Conjugate Gradients

By taking the residuals for the construction of the search directions the *method of conjugate gradients* results. It is a reasonable choice, since the vectors \mathbf{r}_i have many pleasing properties. First, they are orthogonal to all

previous search directions according to Eq. (3.14). Thus, every new search direction, which is generated by conjugation of them, is always a linear independent one. The second property follows from Eq. (3.22). Because $\mathbf{v}_i = \mathbf{r}_i$ is set, the subspace $\text{span}\{\mathbf{r}_0, \mathbf{r}_1, \dots, \mathbf{r}_{i-1}\}$ is identical to that one, which is built up by the search directions. It is called \mathcal{U}_i :

$$\mathcal{U}_i = \text{span}\{\mathbf{u}_0, \mathbf{u}_1, \dots, \mathbf{u}_{i-1}\}. \quad (3.25)$$

As a consequence, the \mathbf{r}_i are not only orthogonal to the previous \mathbf{u} vectors, but also to the previous residuals:

$$\mathbf{r}_i^t \mathbf{r}_j = 0, \quad (3.26)$$

for $i \neq j$. However, the main reason to choose the \mathbf{r}_i follows from another property.

Similar to Eq. (3.13), the computation of the vector \mathbf{r} can be expressed as a recursion:

$$\mathbf{r}_i = -\mathbf{A}\mathbf{e}_i \stackrel{(3.18)}{=} -\mathbf{A}(\mathbf{e}_{i-1} + \alpha_{i-1}\mathbf{u}_{i-1}) = \mathbf{r}_{i-1} - \alpha_{i-1}\mathbf{A}\mathbf{u}_{i-1}, \quad (3.27)$$

depending on the previous residual and $\mathbf{A}\mathbf{u}_{i-1}$. The corresponding subspaces are \mathcal{U}_i and $\mathbf{A}\mathcal{U}_i$. By merging them the new subspace \mathcal{U}_{i+1} results. As given by Eq. (3.14), the next residual \mathbf{r}_{i+1} is orthogonal to \mathcal{U}_{i+1} . Since \mathcal{U}_{i+1} contains the subspace $\mathbf{A}\mathcal{U}_i$, \mathbf{r}_{i+1} is \mathbf{A} -orthogonal to \mathcal{U}_i . Thus, a conjugate GRAM-SCHMIDT process is no more necessary, because the residuals are already *conjugated gradients*. This essential property in combination with the others mentioned above, makes the residuals so important. By premultiplying Eq. (3.27) by \mathbf{r}_j^t the inner product simplifies to

$$\mathbf{r}_j^t \mathbf{A}\mathbf{u}_{i-1} = \begin{cases} \frac{1}{\alpha_{i-1}} \mathbf{r}_{i-1}^t \mathbf{r}_{i-1}, & j = i - 1 \\ -\frac{1}{\alpha_{i-1}} \mathbf{r}_i^t \mathbf{r}_i, & j = i \\ 0, & \text{otherwise.} \end{cases} \quad (3.28)$$

Hence, most of the GRAM-SCHMIDT coefficients from Eq. (3.23) are to be omitted:

$$\lambda_{ij} = \begin{cases} \frac{1}{\alpha_{i-1}} \frac{\mathbf{r}_i^t \mathbf{r}_i}{\mathbf{u}_{i-1}^t \mathbf{A}\mathbf{u}_{i-1}}, & i = j + 1 \\ 0, & i > j + 1. \end{cases} \quad (3.29)$$

The main disadvantage of the method of conjugate directions does not exist anymore. New \mathbf{A} -orthogonal search directions can be created, without

having to keep the old ones in memory. At each iteration step a significant saving in space and time complexity from $\mathcal{O}(n^2)$ to $\mathcal{O}(m)$ is achieved. m denotes the number of entries of \mathbf{A} , which are nonzero. That is why the method of conjugate gradients is the most prominent iterative solver. Using Eq. (3.6) the coefficients λ_{ij} become:

$$\lambda_i = \frac{\mathbf{r}_i^t \mathbf{r}_i}{\mathbf{u}_{i-1}^t \mathbf{r}_{i-1}} = \frac{\mathbf{r}_i^t \mathbf{r}_i}{\mathbf{r}_{i-1}^t \mathbf{r}_{i-1}}, \quad (3.30)$$

depending only on the index i . The last step follows from the identity

$$\mathbf{u}_{i-1}^t \mathbf{r}_{i-1} = \mathbf{r}_{i-1}^t \mathbf{r}_{i-1}, \quad (3.31)$$

which is an implication of the orthogonality properties of the vector \mathbf{r} . In summary, the method of conjugate gradients takes the form:

$$\mathbf{u}_0 = \mathbf{r}_0 = \mathbf{b} - \mathbf{A}\mathbf{x}_0, \quad (3.32)$$

$$\alpha_i = \frac{\mathbf{r}_i^t \mathbf{r}_i}{\mathbf{u}_i^t \mathbf{A}\mathbf{u}_i}, \quad (3.33)$$

$$\mathbf{x}_{i+1} = \mathbf{x}_i + \alpha_i \mathbf{u}_i, \quad (3.34)$$

$$\mathbf{r}_{i+1} = \mathbf{r}_i - \alpha_i \mathbf{A}\mathbf{u}_i, \quad (3.35)$$

$$\lambda_{i+1} = \frac{\mathbf{r}_{i+1}^t \mathbf{r}_{i+1}}{\mathbf{r}_i^t \mathbf{r}_i}, \quad (3.36)$$

$$\mathbf{u}_{i+1} = \mathbf{r}_{i+1} + \lambda_{i+1} \mathbf{u}_i. \quad (3.37)$$

Applying these equations for two dimensions, the same path to the minimum results as shown in Fig. 3.3. The method of conjugate gradients is the method of conjugate directions, except for the fact, that for the generation of the search directions the residuals are used.

Considering Eq. (3.27) again, the subspace \mathcal{U}_i is built up by applying the matrix \mathbf{A} overall $i - 1$ -times on the initial search direction \mathbf{u}_0 :

$$\mathcal{U}_i = \text{span}\{\mathbf{u}_0, \mathbf{A}\mathbf{u}_0, \mathbf{A}^2\mathbf{u}_0, \dots, \mathbf{A}^{i-1}\mathbf{u}_0\}. \quad (3.38)$$

Since $\mathbf{u}_0 = \mathbf{r}_0$, the initial residual can be used in the same way. Above equation is the definition of a KRYLOV subspace. Therefore, the method of conjugate gradients is often called as a KRYLOV subspace method.

3.1.2 Implementation

The conjugate gradient method can be now applied to the computation of the charges q_i by splitting the linear system of equations from Eq. (2.52) into two systems [23]:

$$\sum_{j=1}^N \tilde{V}_{ij} s_j = -\chi_i \quad \text{and} \quad \sum_{j=1}^N \tilde{V}_{ij} t_j = -1, \quad (3.39)$$

where the constraint of net-charge neutrality is included. The chemical potential is then given by

$$\mu = \sum_{i=1}^N s_i / \sum_{i=1}^N t_i, \quad (3.40)$$

with the charges $q_i = s_i - \mu t_i$.

An alternative version for implementation, which is numerically more efficient can be realized by writing Eq. (2.52) via block matrix notation as

$$\begin{pmatrix} \tilde{\mathbf{V}} & \mathbf{C} \\ \mathbf{C}^t & 0 \end{pmatrix} \begin{pmatrix} \mathbf{q} \\ -\mu \end{pmatrix} = \begin{pmatrix} -\boldsymbol{\chi} \\ 0 \end{pmatrix}. \quad (3.41)$$

The block vector \mathbf{C} has all elements equal to unity. Both versions have been implemented in `IMD`, but only the last one has been used in the simulations presented in this work.

3.2 Wolf Summation Method

At each simulation a cut-off radius has to be specified, which limits the number of interacting particles. The computational effort of the force calculation is therefore kept within an acceptable range. For systems with long-range interactions a cut-off radius can be also introduced by applying, e.g. the EWALD summation technique from Sec. 2.3.1.

An alternative method was suggested by Wolf [88]. It incorporates the observation, that in many charged systems the charges screen each other. As a consequence, no long-range charge fluctuations occur. For small wave vectors \mathbf{k} the charge structure factor from Eq. (2.29) then becomes also

small, since it is identical to the FOURIER transform of the charge-charge autocorrelation function:

$$S(k) = \left| \sum_{j=1}^N q_j e^{i\mathbf{k}\cdot\mathbf{r}_j} \right|^2 = \rho(\mathbf{k})\rho(-\mathbf{k}), \quad (3.42)$$

with

$$\rho(\mathbf{k}) = \sum_{i=1}^N q_i e^{-i\mathbf{k}\cdot\mathbf{r}_i}. \quad (3.43)$$

The reciprocal space part of the EWALD sum given by Eq. (2.28) includes the charge structure factor and can thus be neglected. No periodic boundary conditions are required any more and the summation has to be carried out only in direct space.

Wolf builds up his method in three steps:

1. A spherical truncation with the cut-off radius r_c is realized. The total amount of charge within r_c is screened by the same value of opposite sign at r_c .
2. This input from physics makes a modification of the electrostatic potential necessary.
3. The remaining energy oscillations around the correct value of the MADELUNG energy are reduced by an additional damping.

The three steps are now illustrated for a system of N charges.

Spherical Truncation and Charge Neutralization

The net charge Δq within the sphere of radius r_c is equal to the sum of all charges q_j with interatomic distances r_{ij} smaller than r_c :

$$\Delta q = \sum_{\substack{j=1 \\ r_{ij} < r_c}}^N q_j, \quad (3.44)$$

where the charge q_i is located at the center of the sphere, see Fig. 3.4. By setting $-\Delta q$ at r_c , the compensation of all q_j is achieved. Looking at the

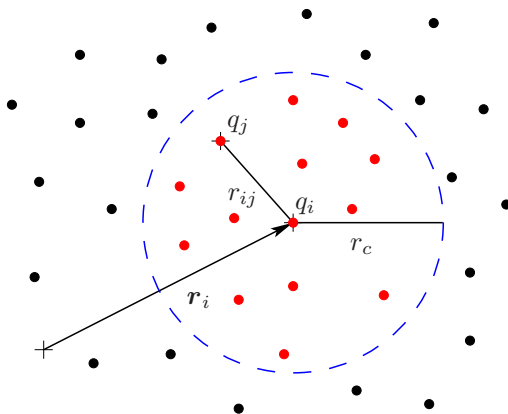


Figure 3.4: In the method of Wolf the physical observation that charges screen each other is realized by locating $-\Delta q$ at the surface of the sphere, where Δq is the total amount of charge within r_c .

electrostatic potential of these charges:

$$\Phi(\mathbf{r}_i) = \sum_{\substack{j \neq i=1 \\ r_{ij} < r_c}}^N \frac{q_j}{r_{ij}}, \quad (3.45)$$

the above *charge neutralization* causes a *shift*:

$$\begin{aligned} \tilde{\Phi}(\mathbf{r}_i) &= \sum_{\substack{j \neq i \\ r_{ij} < r_c}} \frac{q_j}{r_{ij}} + \frac{-\Delta q}{r_c} \\ &= \sum_{\substack{j \neq i \\ r_{ij} < r_c}} \frac{q_j}{r_{ij}} - \sum_{\substack{j=1 \\ r_{ij} < r_c}}^N \frac{q_j}{r_c}. \end{aligned} \quad (3.46)$$

The corresponding electrostatic energy \tilde{E} can be written as follows:

$$\begin{aligned}
 \tilde{E} &= \frac{1}{2} \sum_{i=1}^N q_i \tilde{\Phi}(\mathbf{r}_i) \\
 &= \frac{1}{2} \sum_{i=1}^N \sum_{\substack{j \neq i \\ r_{ij} < r_c}} \frac{q_i q_j}{r_{ij}} - \frac{1}{2} \sum_{i=1}^N \sum_{\substack{j=1 \\ r_{ij} < r_c}}^N \frac{q_i q_j}{r_c} \\
 &= \frac{1}{2} \sum_{i=1}^N \sum_{\substack{j \neq i \\ r_{ij} < r_c}} \phi_{ij}^{\text{sh}}(r_{ij}) - \frac{1}{2r_c} \sum_{i=1}^N q_i^2, \tag{3.47}
 \end{aligned}$$

with the shifted pair potential:

$$\begin{aligned}
 \phi_{ij}^{\text{sh}}(r_{ij}) &= q_i q_j \left(\frac{1}{r_{ij}} - \frac{1}{r_c} \right) \\
 &= \frac{q_i q_j}{r_{ij}} - \lim_{r_{ij} \rightarrow r_c} \left\{ \frac{q_i q_j}{r_{ij}} \right\}. \tag{3.48}
 \end{aligned}$$

The above limit is necessary for the force calculation. It has to be carried out after the spatial derivative. Alternatively, the charge neutralization is not included and the result therefore physically not correct. The x -component of the force on particle i is given by the following expression:

$$F_{ix} = -\frac{d\tilde{E}}{dx_i} = -\sum_{i=1}^N \sum_{\substack{j \neq i \\ r_{ij} < r_c}} \frac{d\phi_{ij}^{\text{sh}}(r_{ij})}{dx_i} = -\sum_{i=1}^N \sum_{\substack{j \neq i \\ r_{ij} < r_c}} \frac{d\phi_{ij}^{\text{sh}}(r_{ij})}{dr_{ij}} \frac{x_{ij}}{r_{ij}}, \tag{3.49}$$

where $d\phi_{ij}^{\text{sh}}/dr_{ij}$ takes the form:

$$\frac{d\phi_{ij}^{\text{sh}}(r_{ij})}{dr_{ij}} = -q_i q_j \left(\frac{1}{r_{ij}^2} - \frac{1}{r_c^2} \right), \tag{3.50}$$

and thus F_{ix} results as

$$F_{ix} = \sum_{\substack{j \neq i \\ r_{ij} < r_c}} q_i q_j \left(\frac{1}{r_{ij}^2} \frac{x_{ij}}{r_{ij}} - \frac{1}{r_c^2} \frac{x_{ij}}{r_c} \Big|_{x_{ij}=x_c} \right). \tag{3.51}$$

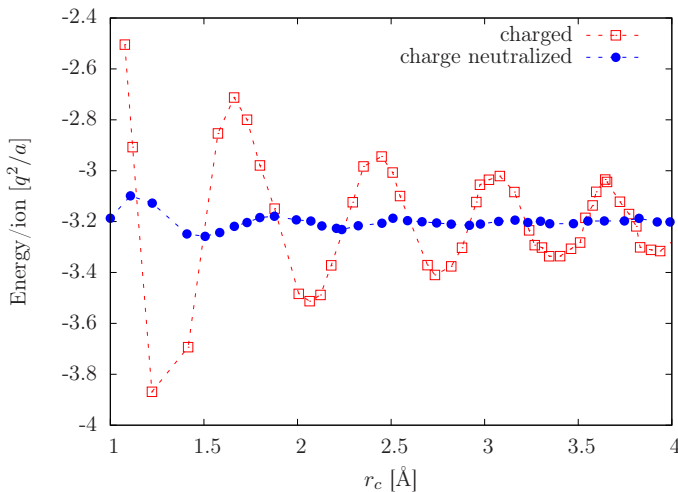


Figure 3.5: The effect of charge neutralization is illustrated for the MADELUNG energy of magnesia [88]. A remarkable reduction of the oscillations around the correct value is achieved.

It is obvious from the above results that by adding a neutralizing charge at the surface of the sphere a smooth cut-off of the pair potential at r_c is realized. The discontinuity of the forces at r_c is also eliminated. Furthermore, the strong oscillations of the energy around its correct value in consequence of the truncation are significantly reduced (see Fig. 3.5). An additional reduction can be achieved by introducing a damping function.

Damping

First, the unshifted electrostatic energy

$$E = \frac{1}{2} \sum_{i=1}^N \sum_{j \neq i} \frac{q_i q_j}{r_{ij}}, \quad (3.52)$$

is considered. For historical reasons the complementary error function is used for the damping. Also any other function is suitable for this purpose, which falls rapidly to zero within the cut-off radius r_c . Inserting into the

above equation a decomposition of unity of the form

$$1 = \operatorname{erfc}(\kappa r) + \operatorname{erf}(\kappa r), \quad (3.53)$$

the energy splits into the following parts:

$$\begin{aligned} E &= \frac{1}{2} \sum_{i=1}^N \sum_{j \neq i}^N \frac{q_i q_j}{r_{ij}} [\operatorname{erfc}(\kappa r_{ij}) + \operatorname{erf}(\kappa r_{ij})] \\ &= \frac{1}{2} \sum_{i=1}^N \sum_{j \neq i}^N \frac{q_i q_j \operatorname{erf}(\kappa r_{ij})}{r_{ij}} + \frac{1}{2} \sum_{i=1}^N \sum_{j \neq i}^N \frac{q_i q_j \operatorname{erfc}(\kappa r_{ij})}{r_{ij}} \\ &= \frac{1}{2} \sum_{i=1}^N \sum_{j=1}^N \frac{q_i q_j \operatorname{erf}(\kappa r_{ij})}{r_{ij}} - \frac{\kappa}{\sqrt{\pi}} \sum_{i=1}^N q_i^2 + \frac{1}{2} \sum_{i=1}^N \sum_{j \neq i}^N \frac{q_i q_j \operatorname{erfc}(\kappa r_{ij})}{r_{ij}} \end{aligned} \quad (3.54)$$

At the last step the limit

$$\lim_{r_{ij} \rightarrow 0} \left\{ \frac{1}{2} \sum_{i=1}^N \frac{q_i^2 \operatorname{erf}(\kappa r_{ij})}{r_{ij}} \right\} = \frac{\kappa}{\sqrt{\pi}} \sum_{i=1}^N q_i^2, \quad (3.55)$$

has been executed. The first term is the inverse FOURIER transformed energy E_{rec} from Eq. (2.28), illustrated here in direct space. Looking at the EWALD summation method from Sec. 2.3.1, one can also identify the second expression as the self-energy term E_{σ} and the third one as the real space part E_{dir} of the total energy. Both are given there by the Eqs. (2.36) and (2.40). In that way the EWALD sums can be derived without the use of the POISSON equation. Note that, since $\operatorname{erf}(\kappa r)/r$ is long-range, it has to be regarded in reciprocal space. E_{dir} and E_{σ} can be now combined to a new energy, noted as E_1 :

$$E_1 = \frac{1}{2} \sum_{i=1}^N \sum_{j \neq i}^N \frac{q_i q_j \operatorname{erfc}(\kappa r_{ij})}{r_{ij}} - \frac{\kappa}{\sqrt{\pi}} \sum_{i=1}^N q_i^2, \quad (3.56)$$

while $E_{\mathbf{k}}$ is redefined as E_2 :

$$E_2 = \frac{1}{2} \sum_{i=1}^N \sum_{j=1}^N \frac{q_i q_j \operatorname{erf}(\kappa r_{ij})}{r_{ij}}, \quad (3.57)$$

with $E = E_1 + E_2$. At this point the Wolf summation method is identical to the one of EWALD. However, in the case of charge neutralization E_2 is negligible, so that only the energy E_1 remains. In the same way as for the undamped potential, Wolf firstly introduces a cut-off radius r_c . E_1 can be then rewritten as:

$$E_1 = \frac{1}{2} \sum_{i=1}^N \sum_{\substack{j \neq i \\ r_{ij} < r_c}} \frac{q_i q_j \operatorname{erfc}(\kappa r_{ij})}{r_{ij}} - \frac{\kappa}{\sqrt{\pi}} \sum_{i=1}^N q_i^2. \quad (3.58)$$

The electrostatic energy at r_c involves also the damping function:

$$\begin{aligned} E_{\text{neutr}} &= \frac{1}{2} \sum_{i=1}^N \frac{q_i \Delta q \operatorname{erfc}(\kappa r_c)}{r_c} \\ &= \frac{1}{2} \sum_{i=1}^N \sum_{\substack{j=1 \\ r_{ij} < r_c}}^N \frac{q_i q_j \operatorname{erfc}(\kappa r_c)}{r_c}, \end{aligned} \quad (3.59)$$

with Δq from Eq. (3.44). By subtracting this energy from E_1 the new energy \tilde{E} results:

$$\begin{aligned} \tilde{E} &= E_1 - E_{\text{neutr}} \\ &= \frac{1}{2} \sum_{i=1}^N \sum_{\substack{j \neq i \\ r_{ij} < r_c}} \phi_{\text{sh}}^D(r_{ij}) - E_{\text{self}}, \end{aligned} \quad (3.60)$$

where ϕ_{sh}^D is now the *shifted* and *damped* pair potential:

$$\phi_{\text{sh}}^D = \frac{q_i q_j \operatorname{erfc}(\kappa r_{ij})}{r_{ij}} - \lim_{r_{ij} \rightarrow r_c} \left\{ \frac{q_i q_j \operatorname{erfc}(\kappa r_{ij})}{r_{ij}} \right\}. \quad (3.61)$$

The only difference to Eq. (3.48) is the complementary error function. It seems that above procedure for obtaining ϕ_{sh}^D can be avoided, if the COULOMB potential $1/r$ is simple replaced by its damped version $\operatorname{erfc}(\kappa r)/r$. However, one has to keep the self-energy part E_{self} in mind, which takes the following form:

$$E_{\text{self}} = \left(\frac{\operatorname{erfc}(\kappa r_c)}{2r_c} + \frac{\kappa}{\sqrt{\pi}} \right) \sum_{i=1}^N q_i^2. \quad (3.62)$$

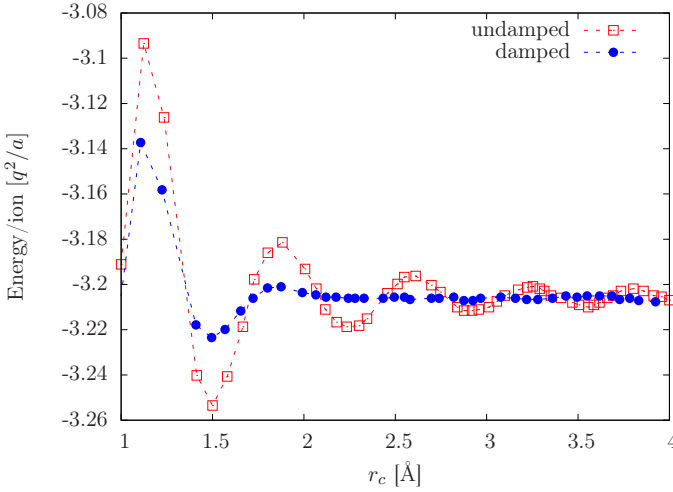


Figure 3.6: In addition to the charge neutralization the energy oscillations can be also reduced by a damping function [88]. Traditionally, the complementary error function is chosen.

The effect of damping is shown for the energy of liquid magnesia in Fig. 3.6. From the pair potential the force on particle i can be calculated:

$$\begin{aligned}
 F_{ix} &= - \sum_{\substack{j \neq i \\ r_{ij} < r_c}} \frac{d\phi_{\text{sh}}^D(r_{ij})}{dr_{ij}} \frac{x_{ij}}{r_{ij}} \\
 &= \sum_{\substack{j \neq i \\ r_{ij} < r_c}} q_i q_j \left[\left(\frac{\text{erfc}(\kappa r_{ij})}{r_{ij}^2} + \frac{2\kappa}{\sqrt{\pi}} \frac{e^{-\kappa^2 r_{ij}^2}}{r_{ij}} \right) \right. \\
 &\quad \times \frac{x_{ij}}{r_{ij}} - \left. \left(\frac{\text{erfc}(\kappa r_c)}{r_c^2} + \frac{2\kappa}{\sqrt{\pi}} \frac{e^{-\kappa^2 r_c^2}}{r_c} \right) \frac{x_{ij}}{r_c} \right]_{x_{ij}=x_c}.
 \end{aligned} \tag{3.63}$$

In summary, the summation method by Wolf is equal to the one by EWALD, if the reciprocal space term is omitted and the potential shift, as a consequence of the charge neutralization, is incorporated. For $r_c \rightarrow \infty$ the shifted potential by Wolf becomes to the real space part of the EWALD

sum. In contrast to EWALD and to other methods, which handle long-range interactions like P3M or tree-based approaches the Wolf summation scales linearly with the number of particles N . Thus, it becomes a powerful tool especially for systems with large N . In addition, simulations with Wolf do not require periodic boundary conditions any more, since they have been necessary only for the FOURIER transformation of the reciprocal space part.

The Wolf summation technique is now applied to the model of SM, as a second improvement of it. There, the charge optimization is affected and has to be reconsidered.

3.2.1 Charge Optimization with Wolf

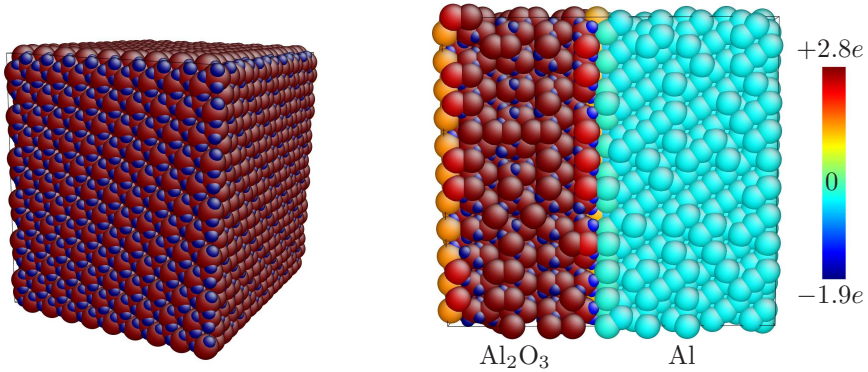
The interaction matrix \tilde{V}_{ij} from Eq. (2.49) contains the long-range term $1/r_{ij}$ in its non-diagonal elements, which are identical to the COULOMB repulsive potential $[f_i|f_j]$. By using the Wolf method $1/r_{ij}$ is replaced by its damped version $\text{erfc}(\kappa r_{ij})/r_{ij}$ plus the self-energy term for the case $i = j$. The matrix \tilde{V}_{ij} takes then the following form:

$$\tilde{V}_{ij} = \begin{cases} J_i^0 - \frac{2\kappa}{\sqrt{\pi}}, & i = j \\ [f_i|f_j] = \frac{\text{erfc}(\kappa r_{ij})}{r_{ij}} + [f_i|f_j]', & i \neq j, \end{cases} \quad (3.64)$$

with $[f_i|f_j]'$ being the rest of the repulsive potential without the long-range term (see App. B).

By implementing the SM model with the modifications discussed until now an initial charge optimization is executed before the actual MD simulation starts. Afterwards, every 1-10 MD steps the charge values are updated. Firstly, a configuration of pure alumina with about 13000 atoms is regarded. The result after the initial charge calculation is illustrated in Fig. 3.7(a). It can be seen there, that the average charge of an aluminium atom is given by $+2.8e$, while for an oxygen atom it takes the value of $-1.9e$ with e being the elementary charge. These values are close to the expected valences $+3e$ and $-2e$ of α -alumina also written as Al_2O_3 . Thus, net-charge neutrality is satisfied with the total charge being equal to $1.16 \cdot 10^{-15}e$.

The model of SM has been implemented in IMD with both summation techniques, EWALD and Wolf. One can now compare the charge values if



(a) An α -alumina structure consisting of nearly 13000 atoms. The resulting charges are close to the expected valences of $+3e$ and $-2e$.

(b) Charge optimization of an interface structure with about 13000 atoms. The atoms in the metallic region have no charge.

Figure 3.7: SM developed their model for the Al/Al₂O₃-system. The charges of the pure oxide and an interface structure have been computed with the modifications of the original approach presented in Sec. 2.3.2.

the reciprocal space term is included or not. For the above system only a difference of about 1.1% results. Looking at the same time at the computing time, a speed up by the factor 60 occurs. Since the Wolf method neglects the reciprocal space part, no \mathbf{k} -vectors have to be built up during the simulation, which leads to a remarkable reduction of the computational effort.

The main reason for choosing a variable charge model is that the charge distribution of a combined system is described correctly. Such an interface structure consisting of alumina and pure aluminium is shown in Fig. 3.7(b). In alumina the charges take the same values as already mentioned above, namely $+2.8e$ and $-1.9e$. However, in the metallic region the atoms have no charge. Thus, the atomic valences are reduced as one approaches the interface from the pure oxide side. The resulting charge distribution is illustrated in Fig. 3.8.

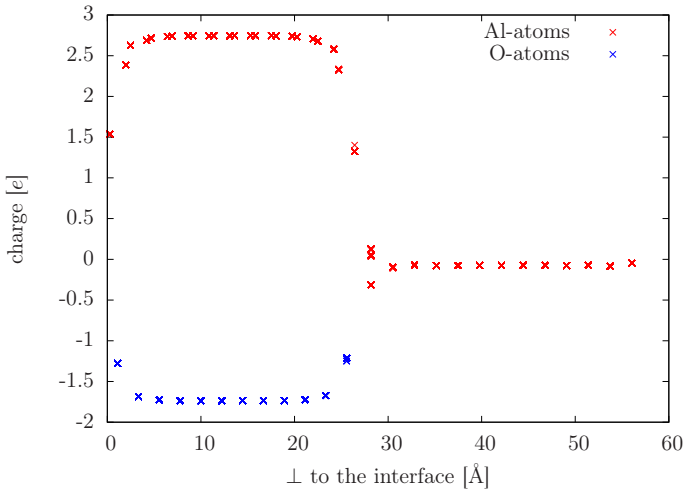


Figure 3.8: The atomic charges of the combined system from Fig. 3.7(b) are shown perpendicular to the interface with different colors for each atom type. The charge values decline if one approaches the metal from the oxide side.

Up to this point, we have improved the SM model by implementing the Wolf method in the charge optimization process. As we combined SM with the model of TS from Sec. 2.3.4, we also have to deal with the long-range forces due to the induced oxygen dipoles. For these terms the Wolf method also will be applied, as it has been done in [96].

3.2.2 Wolf Summation for Dipoles

The procedure is the same as for the electrostatic energy of charges. The total interaction energy of N dipole moments \mathbf{p}_i at positions \mathbf{r}_i has to be considered. It is given by the following expression

$$E^{\text{tot}} = \frac{1}{2} \sum_{\substack{i,j \\ i \neq j}}^N \mathbf{p}_i^t (\nabla \otimes \nabla) \left(\frac{1}{r_{ij}} \right) \mathbf{p}_j. \quad (3.65)$$

with $r_{ij} = |\mathbf{r}_i - \mathbf{r}_j|$ being the distance between the atoms i and j . A splitting of the energy can be now realized, if the same decomposition of unity is used as in Eq. (3.53):

$$1 = \operatorname{erfc}(\kappa r) + \operatorname{erf}(\kappa r), \quad (3.66)$$

where κ is again the EWALD parameter. Additionally, imposing structural periodicity above equation can be rewritten as

$$E^{\text{tot}} = \frac{1}{2} \sum_{i,j}^N \sum_{\mathbf{n}=\mathbf{0}}^{\infty}{}' \mathbf{p}_i^t (\nabla \otimes \nabla) \times \left(\frac{\operatorname{erfc}(\kappa |\mathbf{r}_{ij} + \mathbf{n}L|) + \operatorname{erf}(\kappa |\mathbf{r}_{ij} + \mathbf{n}L|)}{|\mathbf{r}_{ij} + \mathbf{n}L|} \right) \mathbf{p}_j, \quad (3.67)$$

or divided into a real- and a reciprocal-space part:

$$E^{\text{tot}} = E_{\text{dir}}^{\text{tot}} + E_{\text{rec}}^{\text{tot}}. \quad (3.68)$$

Since for the Wolf summation the reciprocal-space term is neglected, the contribution of $E_{\text{rec}}^{\text{tot}}$ has to be examined. For its \mathbf{k} -behavior the FOURIER transform of

$$E_{\text{rec}}^{\text{tot}} = \frac{1}{2} \sum_{i,j}^N \sum_{\mathbf{n}=\mathbf{0}}^{\infty} \mathbf{p}_i^t (\nabla \otimes \nabla) \left(\frac{\operatorname{erf}(\kappa |\mathbf{r}_{ij} + \mathbf{n}L|)}{|\mathbf{r}_{ij} + \mathbf{n}L|} \right) \mathbf{p}_j, \quad (3.69)$$

has to be taken. The prime has been omitted, since the self term (for $\mathbf{n} = \mathbf{0}$ and $i = j$) is now finite. Because of the threedimensional periodicity the above expression can be expanded into a FOURIER series:

$$\tilde{E}_{\text{rec}}^{\text{tot}} = \frac{2\pi N e^2}{V} \sum_{\mathbf{k} \neq \mathbf{0}}^{\infty} \mathbf{k}^t \mathbf{Q}(\mathbf{k}) \mathbf{k} \frac{\exp(-k^2/4\kappa^2)}{k^2}, \quad (3.70)$$

where V is the volume of the simulation cell and $\mathbf{Q}(\mathbf{k})$ the dipole structure factor:

$$\mathbf{Q}(\mathbf{k}) = \frac{1}{N e^2} \sum_{i,j}^N \mathbf{p}_i \otimes \mathbf{p}_j e^{i\mathbf{k} \cdot \mathbf{r}_{ij}}, \quad (3.71)$$

with the normalization factor $1/Ne^2$ and e being the elementary charge. As it can be seen from Eq. (3.70), the large \mathbf{k} contributions to $\tilde{E}_{\text{rec}}^{\text{tot}}$ tend

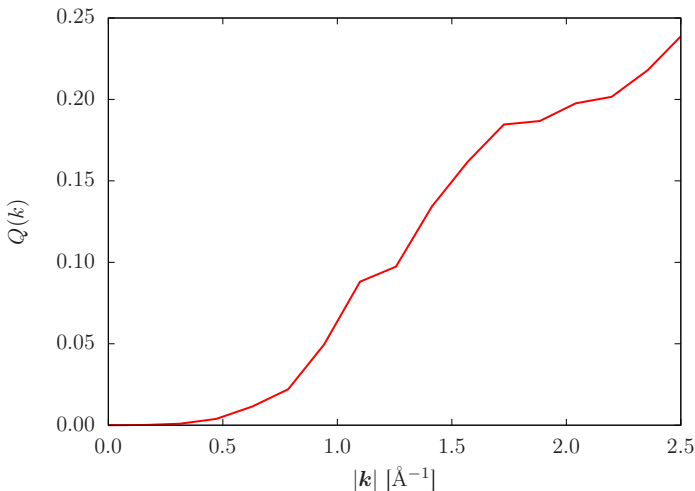


Figure 3.9: The dipole structure scalar of liquid silica as a function of k . $Q(k)$ can be neglected for small k [96].

to zero rapidly, whereas the small \mathbf{k} contributions are governed by the behavior of $\mathbf{Q}(\mathbf{k})$, which is expected to vanish as $k \rightarrow 0$. For this purpose the dipole structure scalar

$$Q(k) = \langle \mathbf{k}^t \mathbf{Q}(\mathbf{k}) \mathbf{k} \rangle_S, \quad (3.72)$$

of liquid silica with 4896 atoms has been regarded in [96]. Since $\mathbf{Q}(\mathbf{k})$ is a discrete function of all reciprocal space vectors, an average over a spherical shell S has to be calculated. This is denoted in the above equation by the angular brackets. The center of S is located at $k = |\mathbf{k}|$. Fig. 3.9 illustrates the resulting k -dependence of $Q(k)$, going to zero for small k -values.

By applying the Wolf method on the original TS potential from 2.3.4, a damped and smoothly cutoff TS potential results. As a comparison between these two potentials the same thermodynamic properties have been studied in [96] as in the original work of TS. One example is the equation of state for liquid silica at 3100 K shown in Fig. 3.10. The new TS potential is compared with the EWALD-summed one, with experimental and ab-initio

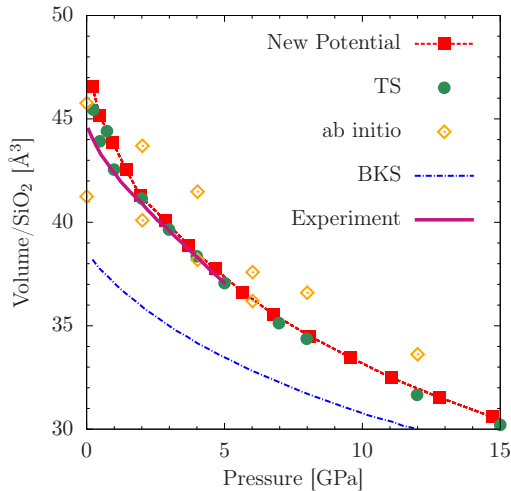


Figure 3.10: The equation of state of liquid silica for the Wolf-summed TS potential [96] compared with the original TS potential [81], experimental [28] and ab-initio data [84] and simulations with BKS [85].

data [28, 84]. It can be seen, that both the full TS potential and its damped and smoothly cutoff version fit better with experiment than the ab-initio data. The latter ones show a large scatter, since the complete equilibration of the system is not possible for low pressures, as consequence of the system size and time restrictions of this first principles method. The potential of van Beest, Kramer, and van Santen (BKS) [85], which is a simple pair potential is also plotted in Fig. 3.10. It does not estimate the volume correctly. There is a systematic deviation of about 13%. Thus, a better description of oxide systems in the simulation is achieved, if dipoles are included.

3.3 Potentials for Oxides

The charge optimization with Wolf in Sec. 3.2.1 has been done statically, without any movement of the atoms. The next step is to determine the charges during the MD simulation. SM proposed an EAM potential for

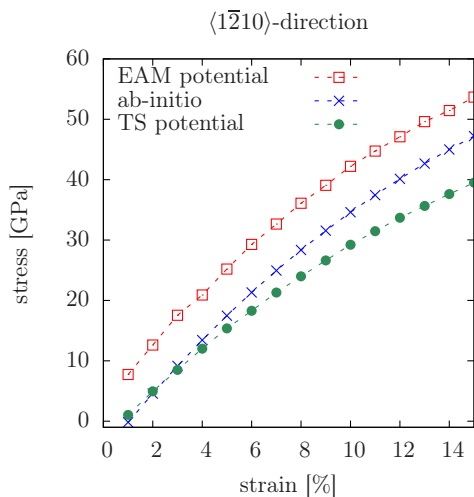


Figure 3.11: Tensile test of bulk Al_2O_3 along the $\langle 1\bar{2}10 \rangle$ -direction. The resulting graphs using the EAM and TS potential are shown and compared with ab-initio data.

the non-electrostatic interactions, which has been already presented in Sec. 2.3.2.

Bulk Al_2O_3

As a first application of it, tensile tests of bulk Al_2O_3 along the directions $\langle 1\bar{2}10 \rangle$, $\langle 10\bar{1}0 \rangle$ and $\langle 0001 \rangle$ have been executed. The results, which are illustrated in figures 3.11, 3.12 and 3.13 have been compared with corresponding ab-initio calculations and the damped and smoothly cutoff TS potential generated by Hocker et al. for alumina [34].

For all directions $\langle 1\bar{2}10 \rangle$, $\langle 10\bar{1}0 \rangle$ and $\langle 0001 \rangle$ the EAM potential of SM shows an unphysical behavior: at low strain relatively high values of stress occur. Along the $\langle 0001 \rangle$ -direction the SM potential matches much better with the ab-initio data than the TS potential. The reason for that is the remarkable change of the charge values while the configuration is stretched. At 2% strain the average charges of Al and O are $+2.76e$ and $-1.84e$ re-

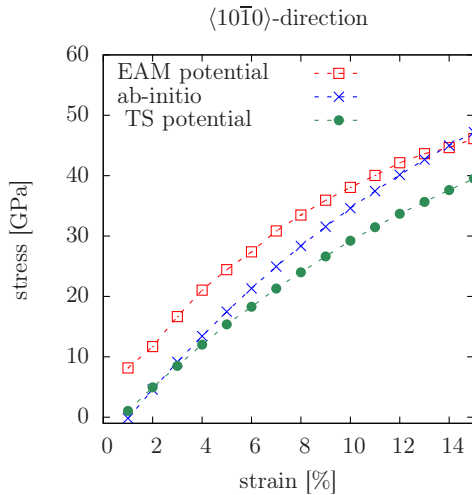


Figure 3.12: Results of the tensile test for the $\langle 10\bar{1}0 \rangle$ -direction. As in the $\langle 1\bar{2}10 \rangle$ -direction the EAM potential of SM exhibits high values of stress at low strain.

spectively. However, at the maximum strain of 15% the charges take the values $+2.3e$ and $-1.53e$. Thus, a correct description of such stretched oxide structures is only possible, if a potential with variable charges is used. Note, that all graphs go through the origin if the simulation reproduces the lattice constant of the system correctly.

The TS potential showed to be appropriate for studying the crack propagation in alumina. Corresponding simulations have been successfully executed [34]. The EAM potential of SM with charge optimization has been also tested for this purpose. Unfortunately, the surface relaxation provided inadequate results for crack propagation.

Al/Al₂O₃-interface system

As mentioned before, one of the main issues of this work is the simulation of combined systems, like the Al₂O₃/Al interface in Fig. 3.7(b). Applying the

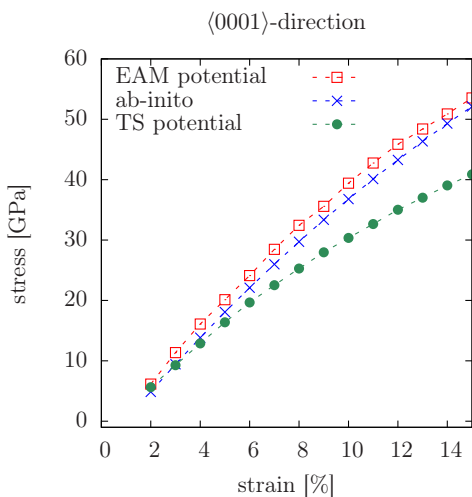


Figure 3.13: In this direction the EAM potential of SM including charge optimization matches much better with the ab-initio data, since the charge values change significantly.

EAM potential of SM on this structure instabilities after a few MD steps occur. The alumina Al-atoms (if Al-terminated) move from the interface into the oxide. As a result the interatomic distances become shorter, the interaction between the atoms stronger and finally the simulated system becomes unstable. This process is accelerated, if the charges are updated frequently.

Another approach has been tried by defining three atom types (Al (metal), Al (oxide), O) and thus three different potentials for the whole interface structure: The TS potential for the oxide, an EAM potential for the metal, while for the interaction of the interface atoms an additional MORSE-stretch potential has been assumed. The last one is a simple pair potential with its analytic form already presented in Sec. 2.3.4, since TS also used for the short-range pair interactions such a potential. Its parameters have been optimized with `potfit` not for the whole sample, but only for a box around the interface. For the interaction of the metal atoms two different EAM potentials have been tested, the one by SM and another one

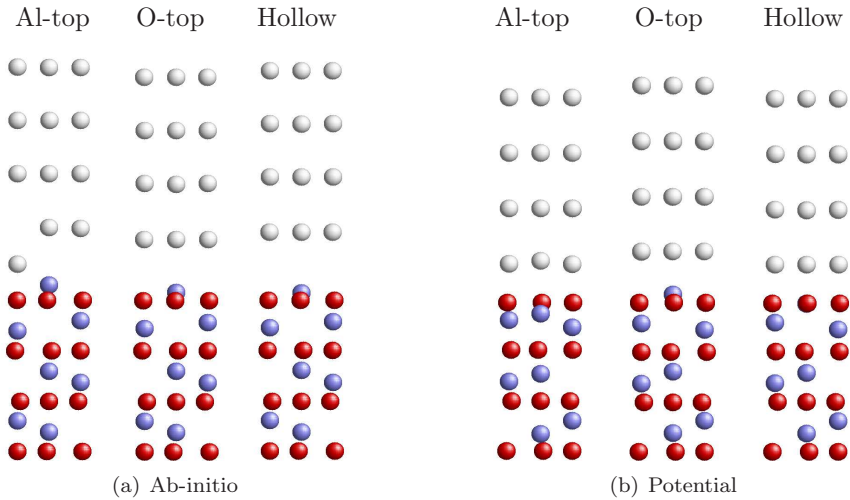


Figure 3.14: The relaxed interface structures $\text{Al}(111)/\text{Al}_2\text{O}_3(0001)$ which result from ab-initio calculations and MD simulations with the new developed potential. All three configurations differ on how the metal atoms are oriented orthogonal to the image plane. At Al-top they are on a vertical line over the Al(oxide)-atoms, at O-top over the O-atoms, while at hollow they are over the gap in between. Following color encoding was used: Al(metal)-atoms: grey, Al(oxide)-atoms: blue, O-atoms: red.

by Mishin *et al.* [57]. After some extensive trials and many parameter values, which have been created with `potfit` the combined system becomes stable. As a test of the best interface potential the work of separation was determined. It was in the same range as the values, which follow from ab-initio calculations. However, the interface potential does not describe the relaxed interface structures shown in Fig. 3.14 well. The Al-top configuration is the most stable one according to ab-initio computations, while from MD simulations with the obtained interface potential the hollow configuration results. Looking at the ab-initio outputs (left part of Fig. 3.14) every third metal Al-atom relaxes to the oxide side of the interface structure. It takes the atomic position under the first oxide layer (Al2). In case

of the created interface potential the Al(oxide)-atoms at the interface pass through the O-layer, thus changing the termination to a O-terminated one. For the configurations O-top and hollow the developed potential provided a better accordance with the ab-initio results, since the Al(metal)-layer at the interface remains planar.

Alternatively, for the interaction of the interface atoms instead of the MORSE-stretch potential an EAM potential has been chosen. The embedding functions for the Al(oxide)- and O-atoms have been also involved into the potential optimization process. Unfortunately, an improvement of the existing potential did not occur, concerning the work of separation and the description of the three different configurations of Fig. 3.14.

For comparison we also have simulated the interface structure with the many-body potentials COMB and ReaxFF, which were described in Sec. 2.3.3.

3.3.1 Simulations with ReaxFF

In [39] aluminium-water reactions have been studied with ReaxFF and the MD-code `lammmps`. The potential used there is also applicable to the Al/Al₂O₃-interface system. For the three structures Al-top, O-top and hollow the work of separation (adhesion energy) could be determined, since ReaxFF stabilizes the interface system without any difficulty. Problems occur with regard of the convergence behavior of the energy. The resulting energies depend on:

- Minimization algorithm (`cg` and also `quickmin` have been used),
- Initial interfacial distance (very sensitive, a different 5th decimal place made a difference of 0.3 in adhesion energy),
- Initial charge values,
- Frequency of charge update.

For the distance of 2.28Å the results are listed in Tab. 3.1. It can be seen, that the values, which follow from the ReaxFF method are comparable with the ones from ab-initio calculations. However, the order of the most stable configuration is not correct.

Method	Al-top	O-top	Hollow
ReaxFF	0.53 J/m ²	0.61 J/m ²	0.37 J/m ²
Ab-initio	0.7 J/m ²	0.5 J/m ²	0.2 J/m ²

Table 3.1: Adhesion energies of the three interface structures Al-top, O-top and hollow, determined by the ReaxFF method [39, 86] and ab-initio computations for the initial distance of 2.28 Å. The obtained values are about of the same order. Unfortunately, the most stable interface structure is Al-top (ab-initio) and not O-top (ReaxFF).

3.3.2 CuSiO₂ with COMB

The second alternative model for simulating interface structures is COMB from Sec. 2.3.3. It is also a many-body potential with charge optimization, which has been created until now for various elements (Si, Cu, Hf, Ti, O) and mixtures (their oxides and alloys), but not for the desired Al/Al₂O₃-interface system. For this reason we simulated a Cu/SiO₂ interface. For this purpose, a Cu/ α -quartz interface with different terminations (Si, O, OO) was created. The number of O-atoms indicates how oxygen-rich or lean the interface structure is.

Charge transfer across the interface

Similar to Shan et al. [69] and as a first test of COMB and our generated structures the charge transfer ΔQ perpendicular to the interface was determined. It is defined as

$$\Delta Q = Q_{\text{Cu/SiO}_2} - (Q_{\text{Cu}} + Q_{\text{SiO}_2}), \quad (3.73)$$

where Q_{Cu} and Q_{SiO_2} are the equilibrated charge values of the separated structures, while $Q_{\text{Cu/SiO}_2}$ stems from the combined system, respectively. Physically, ΔQ specifies the charge transfer if the single structures Cu and SiO₂ are merged to Cu/SiO₂. In the simulation the atoms of Cu and SiO₂ are kept fix and only the charges are equilibrated. After both single structures were combined, a full relaxation and charge equilibration was executed for Cu/SiO₂. In Fig. 3.15 ΔQ is illustrated for the four different

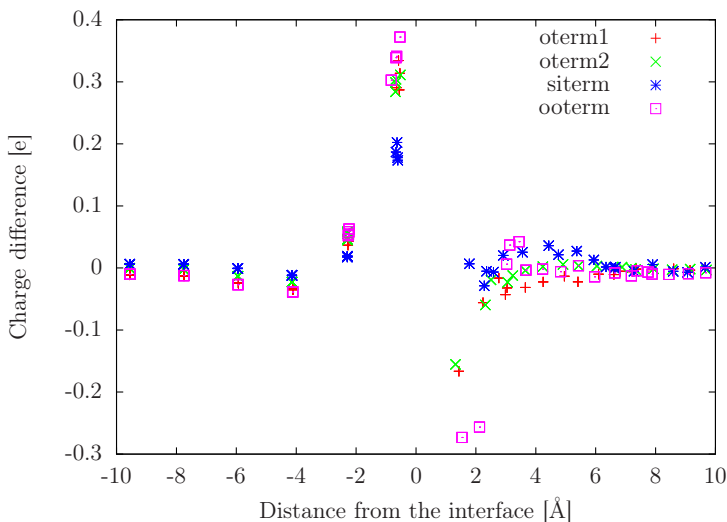


Figure 3.15: The change of charge in case of the Cu/ α -quartz interface. The highest charge transfer occurs for the OO-terminated structure, since a greater amount of O-atoms automatically effect a higher Cu oxidation.

terminations. The two types of O-termination depend on which O-atom is removed from its Wyckoff position. As one can see the charge difference becomes higher if the number of O-atoms at the interface is increased. More Cu-atoms are then bonded, which leads to a higher adhesion between both structures.

We computed also the adhesion energy of Cu/SiO₂. Unfortunately, we could not reproduce the values listed in [69], since the result depend also here on the initial distance of the interface structures.

3.3.3 Variable Charges for Dipoles

For bulk Al₂O₃ the Wolf-summed TS potential provided good simulation results. An obvious possibility for simulating alumina with variable charges is to take the dipole potential and to combine it with the charge optimization routine of the SM model. For this purpose some modifications of the

original TS method are necessary. First, one has to check how TS incorporated the atomic charges in their model. The answer is given by the short-range part of the dipoles from Eq. (2.92):

$$\mathbf{p}_i^{\text{sr}} = \alpha \sum_{j \neq i} \frac{q_j \mathbf{r}_{ij}}{r_{ij}^3} f_{ij}(r_{ij}). \quad (3.74)$$

The values of the q_i are not kept fixed in the simulation any more. They are determined by the optimization process of the SM method, as described in Sec. 2.3.2. As a second consequence of combining TS with SM an additional contribution to the electric field arises. The reason is the charge density ρ_i from Eq. (2.45). By modifying the electric field the induced part of the dipoles is affected, since it depends linearly on \mathbf{E} :

$$\mathbf{p}_i^{\text{ind}} = \alpha \mathbf{E} \left(\mathbf{r}_i; \left\{ \mathbf{p}_j^{n-1} \right\}_{j=1, N}, \left\{ \mathbf{r}_j \right\}_{j=1, N} \right). \quad (3.75)$$

The additional part of the electric field takes the following form:

$$\mathbf{E}^{\text{SM}} = - \sum_{j \neq i} \{q_j - \mathcal{Z}_j\} \nabla_j [j|f_i]', \quad (3.76)$$

with $[j|f_i]'$ being the nuclear attraction potential without the $1/r_{ij}$ -term, which is indicated by the prime.

As a first application of this new potential the crack propagation in alumina has been studied, for which the EAM potential of SM was not appropriate. Unfortunately, one has to make a compromise concerning the charge values. The potential parameters of the TS model D_{ij} , γ_{ij} , r_{ij}^0 , α , b and c are only determined optimally in `potfit`, if the valences of Al and O take the adjusted values of $+2.0e$ and $-1.4e$, respectively. The result is shown in Fig. 3.16. It can be seen by the color encoding, that the atomic charges change their values while the crack is propagating to the right. By using the visualization tool `MegaMol` [32] the fluctuations of the charges have been made visible (Fig. 3.17).

The main success of merging both methods is that they are about two orders of magnitude faster than the COMB potential or the ReaxFF method.

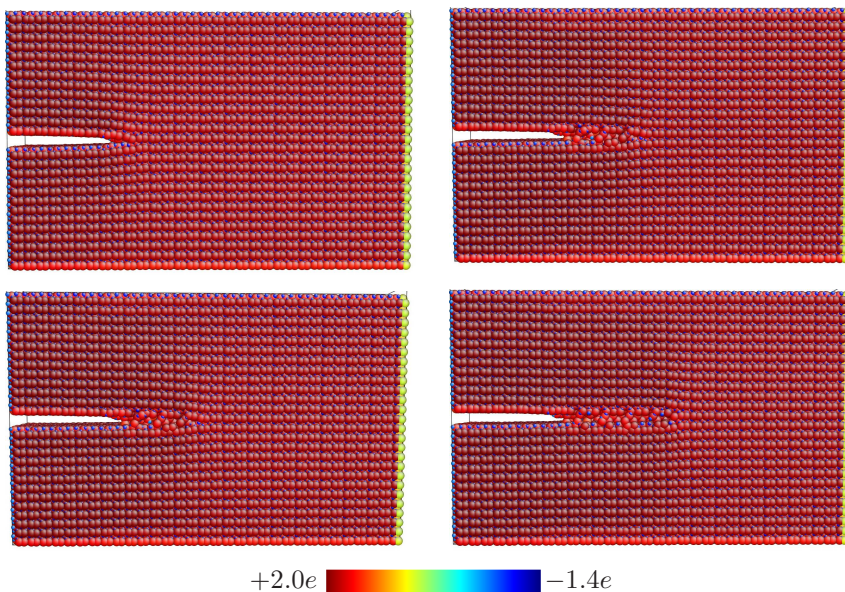


Figure 3.16: Adjusted charge values for bulk Al_2O_3 by combining the models of TS and SM. The crack propagates to the right and changes the charge values of the atoms.

Summary

The original version of the SM model has been modified in this work by using the Wolf summation method for the long-range terms within the interaction matrix \tilde{V}_{ij} (see Eq. (2.49)). As a second improvement, the system of linear equations for determining the valence charges is solved iteratively by the conjugate gradient method. Both developments result in a speed up of the charge computation by the factor 60.

For executing MD simulations with the SM model the charge optimization is combined with a non-electrostatic potential. SM proposed an EAM potential presented in Sec. 2.3.2. Simulations with pure alumina (Al_2O_3), like determining the stress-strain curves, were successful. However, the interface system $\text{Al}(111)/\text{Al}_2\text{O}_3(0001)$ became unstable. To get it stable three different atom types (Al (metal) Al (oxid), O) were defined. Also for

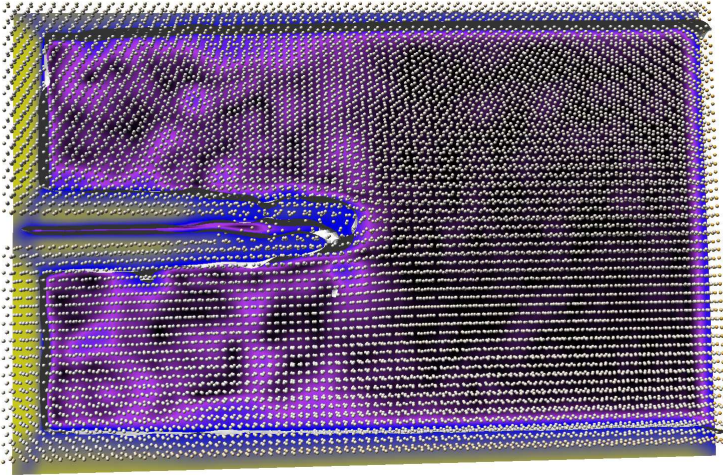


Figure 3.17: The crack propagation in Al_2O_3 with variable charges. In this picture the charge fluctuations of the Al atoms have been visualized with `MegaMol`. In the region of stress the charges are $q_{\text{Al}} = 2.0$ (black color), while smaller values appear in the crack region (colors purple, blue and yellow). The colors have been chosen in such a way to make the fluctuations visible.

the interactions three different potentials were chosen: For metallic Al the EAM potential of SM [78] and also occasionally the one of Mishin et al. [57], while for the oxide the force field of Höcker et al. [34] was applied. These potentials were not optimized with `potfit`. The third one for the Al- Al_2O_3 interaction was a MORSE-stretch potential. Its parameters were optimized in a box around the interface. The combined system became stable, but unfortunately the description of the three different interface structures (Al-top, O-top, Hollow) was not correct, compared to ab-initio calculations.

As an attempt of getting the interface structure stable the model of TS

and SM were combined. The charges of the atoms become variable and the oxygen atoms polarizable. In pure alumina a crack propagated successfully with fluctuating charge values (see Fig. 3.17). However, the combination of both models is only for adjusted charge values of Al and O possible.

Alternative methods for variable charges, but without dipoles, are the COMB potential and ReaxFF from Sec. 2.3.3. These potentials use many-body interactions and are in comparison with our approach above two orders of magnitude slower.

Chapter 4

Flexoelectricity

One application of the method of Tangney and Scandolo [81] from Sec. 2.3.4 was the study of crack propagation in α -alumina (Al_2O_3) done by Hocker *et al.* [34]. The effective potentials were created therefor by Beck *et al.* [6]. For the visualization of the simulation results the software package `MegaMo1` [32] was used. In the visualization of Grottel *et al.* [31] the oxygen ions were presented by arrows, indicating the direction of the induced dipole moment. Surprisingly, the simulations show regions in front of the crack tip with ferroelectric and antiferroelectric domains, although α -alumina is not piezoelectric (see Fig. 4.1). Such a phenomenon where ferroelectricity is caused not by strain, but by a strain *gradient* is called *flexoelectric* effect [41, 55].

In the following, the effect was observed in a more controlled way in the simple cubic oxide periclase, crystalline magnesia (MgO) with sodium chloride structure, where three well defined displacement modes were applied. Two of the three flexoelectric coefficients could be measured easily. The third one needed a special treatment.

First, however, a short introduction in the terms of piezo- and flexoelectricity is given.

The Term of Piezoelectricity

In 1880 Pierre and Jacques Curie discovered that a voltage emerges from the deformation of a material [16, 17]. In a microscopic view, oriented electrostatic dipole moments build up in dielectric materials due to external strain. In general, the linear piezoelectric coupling between polarization \mathbf{P} and strain ε can be expressed by a three-stage tensor d :

$$P_i = d_{ijk}\varepsilon_{jk}. \quad (4.1)$$

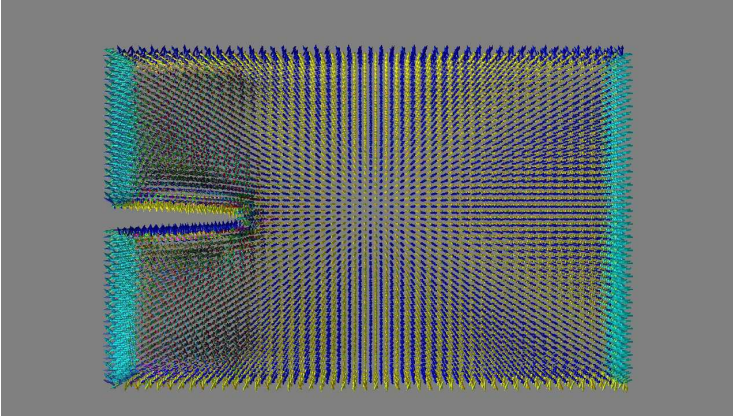


Figure 4.1: Crack propagation in Al_2O_3 . The dipole moments of the oxygen atoms are visualized with `MegaMol`. In front of the crack the dipoles are anti-parallel orientated, while below and above is no orientation.

The corresponding free energy density (with the electric field \mathbf{E}) can be written as

$$f_{\text{piezo}} = \frac{1}{2} \mathbf{E} \cdot \mathbf{P} = \frac{1}{2} E_i d_{ijk} \varepsilon_{jk}. \quad (4.2)$$

As upon inverting spatial coordinates the electric field \mathbf{E} changes sign, but not the strain tensor ε , the free energy (Eq. (4.2)) is not inversion-invariant, and piezoelectricity is forbidden in crystalline systems with inversion symmetry.

Flexoelectric Behavior

However, even in inversion-symmetric systems and thus in principle in all crystalline dielectrics a polarization can develop due to response to a strain *gradient* $\varepsilon_{jk,l}$ [72], or, as used in many publications and also in this thesis, as response to the second derivative of the displacement field $u_{j,kl}$ [10, 54] (for the relation between the two conventions see [37, 38]). The effect is denoted *flexoelectricity*. First predicted by Mashkevich and Tolpygo [55] and phenomenologically described by Kogan [41], flexoelectricity establishes a new material class for industrial products that are based on generating voltage

by deformation. In the bulk the flexoelectric effect is small, but it becomes important in nanocrystals or epitaxial thin films where the strain gradient can take large values [47]. With suitable geometries the flexoelectric effect can be used to produce piezoelectric metamaterials even with centrosymmetric compounds [80]. Recently, in a nanoscale volume of a ferroelectric film, polarization could be switched mechanically due to the stress gradient generated by the tip of an atomic force microscope [49]. Other phenomena, where flexoelectricity influences properties, are the modification of the dielectric constant in nanodevices [11, 12] and generally piezoelectric-like responses in devices made out of non-piezoelectric materials [51, 93].

In linear response flexoelectricity is described by a fourth-rank tensor μ :

$$P_i = \mu_{ijkl} u_{j,kl}. \quad (4.3)$$

In a crystal of cubic symmetry, the coupling tensor

$$\mu_{ijkl} = (\mu_{11} - \mu_{12} - 2\mu_{44})\delta_{ijkl} + \mu_{12}\delta_{ij}\delta_{kl} + \mu_{44}(\delta_{ik}\delta_{jl} + \delta_{il}\delta_{jk}), \quad (4.4)$$

(δ_{ijkl} is 1 for all indices equal and zero otherwise) has only three independent components [38, 54]. There is no piezoelectric coupling.

The flexoelectric coefficients are difficult to measure. In experiments [5, 10, 15, 30, 50, 94], as a rule only one or two can be determined. Numerical simulations are a useful supporting tool. Although the analytical description [53, 62, 64, 79] and ab-initio [35–37] studies have advanced, no molecular dynamics (MD) simulations have been performed yet. There exists one single atomistic approach [52], where an ab-initio based polarizable force field for barium titanate was adopted to model dipole orientation phenomena, with a focus on the dependence of polarization on the sample size.

4.1 MD Simulations

In this thesis MD simulations of the oxygen periclase are presented, performed with IMD [75]. For the ions of magnesia, the highly accurate, effective interaction force field by Beck *et al.* [6] has been applied. It is based on the TS model [81], which appreciably increases accuracy for collective phenomena in metal oxide systems [7, 33].

In ionic solids one has to discern two kinds of polarization: the *primary*

one, which results from the asymmetric displacement of the ionic charges due to the strain gradient after relaxation (“rigid ion contribution”), and an *induced* one due to the deformation of the electronic orbits (“shell contribution”). Oxygens are particularly appealing, because the O-atom is strongly polarizable and the relation between the two contributions is of interest.

In the literature different terms are used. In their first-principle studies of flexoelectricity Hong and Vanderbilt (HV) [37] differentiate between a pure *electronic* (or “frozen ion”) part, which depends on higher moments (octupole term) of the charge-density caused by atomic displacements [36] and a *lattice* (or “relaxed-ion”) part as a result of internal sublattice shifts after relaxation. Both terms of primary and lattice polarization are describing the same physical mechanism, only the realization done in this work with MD differs from the one of HV.

It should be mentioned that the long-range and the short-range part of the induced dipole moments in the TS model (Eqs. (2.92) and (2.94)) have correspondences in the shell model as employed e.g. by Askar *et al.* [4]. Both methods mimic a polarization caused by a macroscopic electric field and one by approaching ion cores. In the shell model calculations the polarization due to relative sublattice shifts and hence the primary polarization is not considered [54].

4.1.1 Displacement Modes

The three flexoelectric constants μ_{11} , μ_{12} and μ_{44} of periclase can be determined by applying three different inhomogeneous deformation modes to the ionic system of MgO along the cubic fourfold axes [10]. The displacement fields are chosen in such a way, that always one coefficient of μ_{ijkl} given by Eq. (4.4) remains. The corresponding analytical form of the displacements is:

$$(a) \quad u_z = k \frac{x^2}{2}; \quad P_z = P_3 = \mu_{3311} u_{3,11} = k \mu_{12} \quad (4.5)$$

$$(b) \quad u_z = k \frac{z^2}{2}; \quad P_z = P_3 = \mu_{3333} u_{3,33} = k \mu_{11} \quad (4.6)$$

$$(c) \quad u_x = kxz; \quad P_z = P_3 = \mu_{3113} u_{1,13} + \mu_{3131} u_{1,31} = 2k \mu_{44}, \quad (4.7)$$

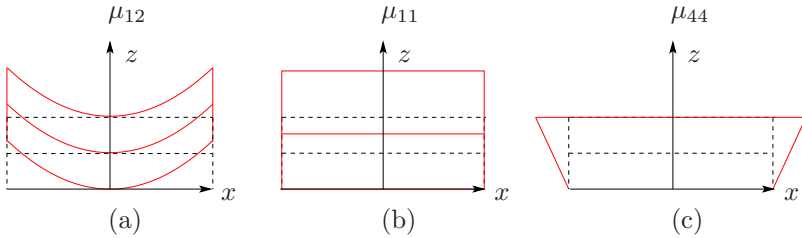


Figure 4.2: The undeformed samples (dashed lines) are blocks of $210.5 \times 42.1 \times 126.3 \text{ \AA}$ containing 120,000 Atoms. They are deformed by the displacement modes given by Eqs. (4.5), (4.6) and (4.7) (red lines). The coordinate system points along the cubic fourfold axes of the system. When applied to a periclase sample, they allow to determine the three superscribed flexoelectric constants. Sample (a) is continued periodically along the y - and z -, sample (b) along x - and y -directions and sample (c) along y -direction only. The open surfaces are neutral.

with the polarization calculated by Eq. (4.3). The constant k rules the strength of the displacement and its gradient. The corresponding geometries are illustrated in Fig. 4.2.

For the MD simulations a periclase sample of about 120,000 atoms is created. It is deformed by shifting all atoms by the above quadratic functions of their unperturbed positions. In case of the bending and shearing mode (a) and (c) the first surface layers are fixed. Upon relaxing the system the forced strain causes additional atomic shifts within the unit cell, which break the inversion symmetry and generate a global primary polarization (see Sec. 4.1.2). This method corresponds most closely to the experimental setup. However, in deformation mode (b) a surface stabilization of the artificially introduced bulk strain is not possible, since the atoms will relax to their equilibrium positions once a MD simulation is started.

4.1.2 Primary Polarization

The primary polarization is calculated as the sum of all dipole moments $\mathbf{p}_i = q_i \mathbf{r}_i$ within the volume V divided by V :

$$\mathbf{P}^P = \frac{1}{V} \sum_{i=1}^N \mathbf{p}_i = \frac{1}{V} \sum_{i=1}^N q_i \mathbf{r}_i, \quad (4.8)$$

with q_i being all ion charges and their positions \mathbf{r}_i after the deformation and V cubic volumes of different sizes inside the samples, avoiding surface charges.

Looking at the above expression analytically, \mathbf{P}^P can be expressed as

$$\mathbf{P}^P = \frac{1}{V} \sum_{i=1}^N q_i \mathbf{r}_i = \frac{1}{V} \sum_{i=1}^N q_i (\mathbf{r}_{0i} + \mathbf{u}_i) = \frac{1}{V} \sum_{i=1}^N \mathbf{u}_i q_i, \quad (4.9)$$

where \mathbf{r}_{0i} are the atomic positions of the undeformed sample and the \mathbf{u}_i functions of the unperturbed atomic coordinates given by the Eqs. (4.5), (4.6) and (4.7). The first sum vanishes, since in case of no shift the charges are arranged inversion symmetric. For deformation mode (a) \mathbf{u}_i in the remaining sum can be written as

$$\mathbf{u}_i = k \frac{x_{0i}^2}{2} \hat{\mathbf{e}}_z = \frac{k}{2} \left(\frac{a_0}{2} \right)^2 n_{xi}^2 \hat{\mathbf{e}}_z. \quad (4.10)$$

a_0 is the lattice constant of MgO, so that the x -position of atom i is identical to $x_{0i} = n_{xi}(a_0/2)$ with $n_{xi} \in \mathbb{N}$. Executing now the last part of the initial sum no primary polarization results:

$$\mathbf{P}^P = \frac{1}{V} \sum_{i=1}^N \mathbf{u}_i q_i = \frac{k}{2V} \left(\frac{a_0}{2} \right)^2 \hat{\mathbf{e}}_z \sum_{i=1}^N q_i n_{xi}^2 = 0 \quad (4.11)$$

Since the square of the undeformed x -positions n_{xi}^2 is always positive and the charge values q_i alternate in sign, the above sum over the undeformed lattice is also equal zero. For the modes (b) and (c) the same result follows: With the deformation fields from Eq. (4.5) to (4.7) the local inversion symmetry is not broken and thus no primary polarization occurs. Numerically, a single initial MD step has been executed to confirm the analytic evaluation. This apparent contradiction is resolved if one looks at the real cause

of the primary polarization.

As already mentioned in the previous definition of the terms primary and induced polarization, the first contribution is a result of internal sublattice shifts within the unit cell, which follow after relaxation, while the initial uniform strain is preserved [37, 54]. There is no unique approach in the literature of how to maintain the applied strain gradient and how to execute the relaxation for getting the desired sublattice shifts. HV [37] introduced for the lattice (or “relaxed-ion”) polarization, which corresponds to the primary one here, artificial forces for the atoms of the unit cell after the induced displacements occurred. Such “force patterns” can be chosen differently. A mass-weighted choice seems to be most reasonable one. The dependence of the flexoelectric constants of the chosen “force pattern” is discussed in this article.

In this thesis three steps have been executed to gain a non-vanishing primary polarization for the modes (a) and (c) by the use of MD:

1. In contrast to the ab-initio work of HV, where the unit cell as a whole is shifted and all atoms within obtain the same displacement, here all atoms of the sample are displaced differently by the quadratic functions of their former lattice position given by the Eqs. (4.5) and (4.7).
2. The inhomogeneous strain is kept by locking the surface atoms, simulating in such a way the same conditions as in the experiment. For mode (b) such a surface stabilization is not possible.
3. A relaxation with fixed surface layers is performed, which leads to the formation of a global and homogeneous polarization field within the bulk.

For the relaxation a microconvergence integrator (mik) is used, since the deformed sample represents a non-equilibrium state and needs some time for relaxation. If the velocity of an atom passes the minimum in the potential landscape, it is reset to zero after each step [75]. A finite homogeneous polarization comes up, however, only close to 0 K. After finally 60,000 MD steps the primary polarization converges to a fixed value (see Fig. 4.3). The same procedure has been executed for different k -values of the displacement fields. As expected a linear dependence of polarization and strain from Eq. (4.3) follows, which is shown in Fig. 4.7(a). From the slope of

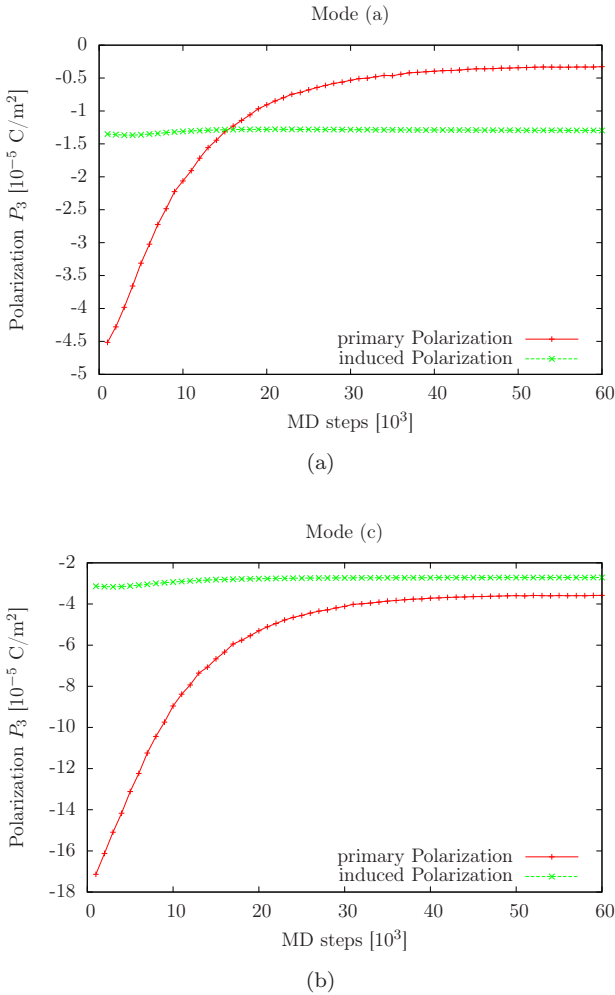


Figure 4.3: The primary polarization converges after 60,000 MD steps by using the microconvergence integrator (mik) in IMD. However, the induced polarization reaches its fixed value from the beginning. Both modes (a) and (c) are illustrated for $k = 1.35 \cdot 10^6/\text{m}$.

the lines the primary part of the flexoelectric constants μ_{12}^p and μ_{44}^p can be extracted:

$$\mu_{12}^p = -2.2 \frac{\text{pC}}{\text{m}} \quad (4.12)$$

$$\mu_{44}^p = -10.1 \frac{\text{pC}}{\text{m}}. \quad (4.13)$$

μ_{44}^p is about four times bigger than μ_{12}^p . One reason for this difference is the larger change of the atomic layer distances if the sample is sheared, instead of being bent. The missing value of the flexoelectric constant μ_{11} is determined in Sec. 4.2 by a slightly modified approach.

4.1.3 Induced Polarization

The induced polarization, denoted as \mathbf{P}^{TS} is calculated by the Eqs. (2.94) and (2.92). As in the case of the primary polarization, it points after applying the deformation modes (a), (b) and (c) also along the three-axis.

Since the short range induced dipole moments \mathbf{p}_i^{sr} of Eq. (2.92) turn out to be one magnitude less than the long-range ones, the sign of the total induced moments depends essentially on the sign of the electric field at the oxygen positions. This sign is made plausible by the displacement of already nearest neighbor Mg^{2+} charges in Fig. 4.5. In case (a) it is negative, in case (b) positive. The notation Mg^{2+} is used although the effective valence charge determined in [6] is about $1.23e$.

The induced polarization is extracted from the same relaxation process as for the primary one. The resulting linear dependence is illustrated in part (b) of Fig. 4.7. The corresponding induced contributions to the flexoelectric coefficients μ_{12}^{TS} and μ_{44}^{TS} take the values:

$$\mu_{12}^{\text{TS}} = -9 \frac{\text{pC}}{\text{m}} \quad (4.14)$$

$$\mu_{44}^{\text{TS}} = -6.6 \frac{\text{pC}}{\text{m}}. \quad (4.15)$$

Both are of same order and sign.

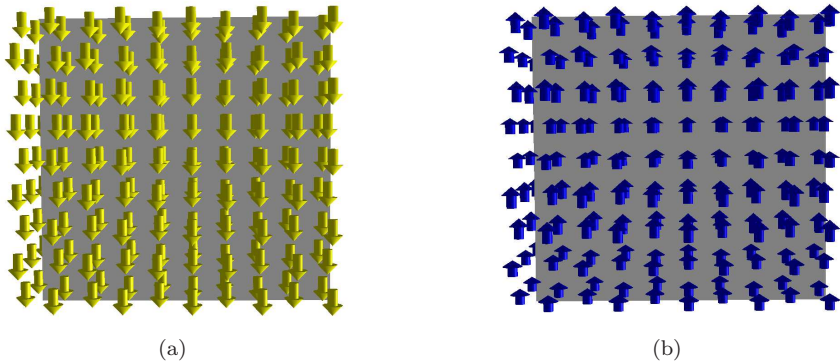


Figure 4.4: The induced dipoles of the oxygen atoms are oriented in case of displacement (a) along the negative z -direction, while for displacement (b) they point along the positive z -axis. This is in accordance with the direction of electric field, as illustrated in Fig. 4.5. The color coding done by MegaMol visualizes the orientation of the arrows.

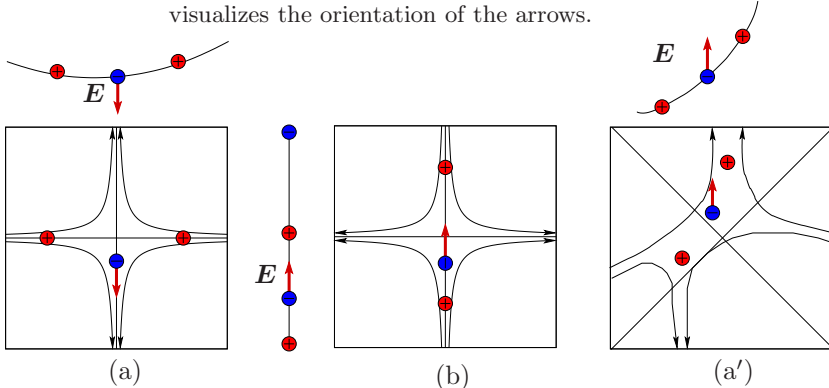


Figure 4.5: The direction of the dipoles in the TS model is essentially given by the electric field E as the long-range induced polarization (see Eqs. (2.94) and (2.92)) dominates the short-range one. Why the dipoles in Fig. 4.4 are oriented oppositely, can be understood by considering the electric field of two Mg^{2+} -atoms (red) at the position of the polarizable O^{2-} -atom (blue) in between. On the left side the bending case (a) of Fig. 4.2 is shown in one plane. The E -field points downwards. However, for the stretching displacement (b) from Eq. (4.5) (right) it points upwards. In case of mode (a') (see Sec. 4.2 and Eq. (4.18)) the E -field points also upwards.

4.2 The Flexoelectric Constant μ_{11}

The three steps mentioned above for determining the primary polarization are unfortunately not applicable to deformation mode (b), because of the second point: The strain gradient cannot be kept by fixing the surface during relaxation, since the atoms fall down immediately to their unshifted positions. Another approach was tried by restricting the movement of one atom type (Mg or O). In such a way the initial inhomogeneous strain was preserved and a primary polarization could have occurred by relaxation of the other atom type. But, also this trying failed and returned no reasonable results.

An alternative method to obtain the missing constant μ_{11} is to set up a new experiment. The aim is to express analytically the new flexoelectric constant, which follows from this different approach by all other ones: μ_{12} , μ_{11} and μ_{44} . Since the values μ_{12} and μ_{44} are already known, the missing one μ_{11} can be then easily extracted. As a first step of the alternative experiment the sample is regarded in a new coordinate system, which is rotated to the older one by $\pi/4$. The corresponding rotation matrix takes the form:

$$\mathbf{R} = \begin{pmatrix} 1/\sqrt{2} & 0 & 1/\sqrt{2} \\ 0 & 1 & 0 \\ -1/\sqrt{2} & 0 & 1/\sqrt{2} \end{pmatrix}. \quad (4.16)$$

The crystal surface still remains neutral as in the former, unrotated case. In a second step the deformation mode (a) is executed:

$$u'_{z'} = k \frac{x'^2}{2}, \quad (4.17)$$

where the prime indicates the new coordinate system and mode (a) is thus renamed to mode (a'). As by Eq. (4.5) the resulting polarization points along the z' -direction:

$$P'_{3'} = \mu'_{3'3'1'1'} k, \quad (4.18)$$

with $\mu'_{3'3'1'1'}$ being the flexoelectric constant in the rotated system. The notation μ'_{12} can be also used, since it is the same deformation mode. By use of Eq. (4.16) it is possible to write $\mu'_{3'3'1'1'}$ as a function of the non-primed components:

$$\mu'_{3'3'1'1'} = \mu_{ijkl} R_{i3'} R_{j3'} R_{k1'} R_{l1'}. \quad (4.19)$$

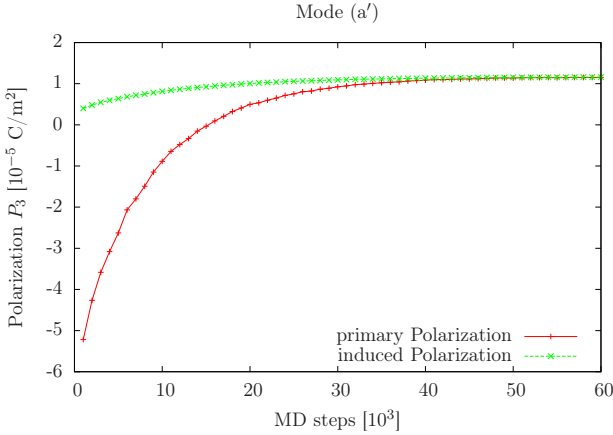


Figure 4.6: The primary and induced polarization in case of mode (a'). It also converges after 60,000 MD steps using mik. Both contributions reach nearby the same value and differ slightly. The strength of the strain gradient is here also given by the same value: $k = 1.35 \cdot 10^6 / \text{m}$.

For μ_{ijkl} Eq. (4.4) is still valid. The detailed calculation is listed in App. C, here only the final result is presented:

$$\mu'_{3'3'1'1'} = \frac{1}{2} \left\{ \mu_{11} + \mu_{12} - 2\mu_{44} \right\}. \quad (4.20)$$

In the simulation the three steps of Sec. 4.1.2 are performed: Displacement of all atoms by Eq. (4.17), fixing the surface layers and relaxation. Primary and induced polarization have been determined once again for different strengths of the strain gradient given by k . All plots are summarized in Fig. 4.7, while in Fig. 4.6 the convergence behavior of both types of polarization for mode (a') is shown. $\mu'_{3'3'1'1'}$ takes finally the following value:

$$\mu'_{3'3'1'1'} = \mu'_{12} = (7.8 + 7.6) \frac{\text{pC}}{\text{m}} = 15.4 \frac{\text{pC}}{\text{m}},$$

where the first entry results from the primary polarization, while the second one from the induced contribution. Compared to μ_{12} , its prime version is of the same order. However, primary and induced part are nearby identical

and of positive sign. The change of sign can be understood by looking again at the induced polarization and the immediate connection of the induced dipole moment and electric field at the oxygen position given by Eq. (2.94). In Fig. 4.5 the left picture is rotated by $\pi/4$, shown separately on the right. The displacement (a') causes an electric field vector, which points along the positive z' -direction. Thus, the induced polarization points in the same direction.

4.3 The Resulting Flexoelectric Constants

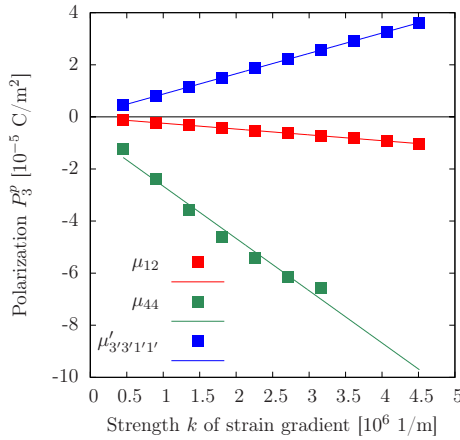
In summary, in Fig. 4.7 the magnitude $P = |\mathbf{P}|$ of the polarization (boundary atoms omitted) scales linearly with the strain gradient. Such a linear dependence has been observed in recent experiments by Cross [15] for different ionic bulk materials and Baskaran and He for polyvinylidene fluoride films [5]. All flexoelectric constants of periclase with both parts have been determined successfully from Fig. 4.7:

$$\mu_{12} = -(2.2 + 9.0) \frac{\text{pC}}{\text{m}} = -11.2 \frac{\text{pC}}{\text{m}} \quad (4.21)$$

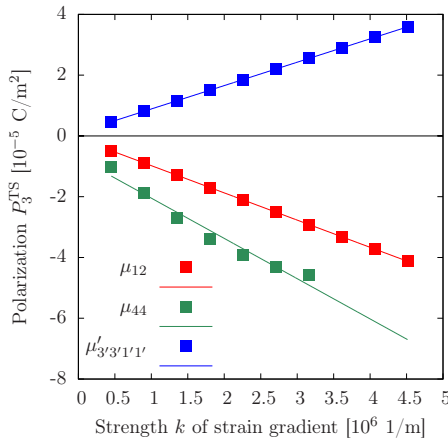
$$\mu_{11} = -(2.4 - 11) \frac{\text{pC}}{\text{m}} = 8.6 \frac{\text{pC}}{\text{m}} \quad (4.22)$$

$$\mu_{44} = -(10.1 + 6.6) \frac{\text{pC}}{\text{m}} = -16.7 \frac{\text{pC}}{\text{m}}, \quad (4.23)$$

where the first entry in the bracket results from the primary, the second from the induced polarization. μ_{11} was calculated from $\mu'_{3'3'1'1'}$ via μ_{12} and μ_{44} . The induced part is at μ_{12} and μ_{11} bigger than the primary one. Except μ_{11} all coefficients are in total of the same order, differing also in sign compared to the other two. This results by the larger positive induced contribution of μ_{11} . Why μ_{11}^{TS} is positive is explained by Fig. 4.5.



(a)



(b)

Figure 4.7: In Fig. (a) the primary polarization P_3^P is plotted against the strength k of the applied strain gradient, while in Fig. (b) the induced polarization P_3^{TS} obtained by the TS model is illustrated. Each point follows after a relaxation of 60,000 MD steps using the microconvergence integrator (mik) in IMD. As expected, in all deformation modes (a), (c) and (a') the polarization is a linear function of the strength of the strain gradient. For μ_{11} the $\pi/4$ -rotated sample was also deformed by mode (a). From the slope of the lines the flexoelectric constants μ_{12} , μ_{44} and $\mu'_{3'3'1'1'}$ are derived.

For periclase flexoelectric constants were determined in [36, 37]. However, only in the latter publication of HV [37] both parts of the polarization and, thus, of the flexoelectric constants are regarded. In cubic materials the components of the flexoelectric tensor decompose in a longitudinal and transverse part. In [37] only the longitudinal components have been calculated by first-principles. They take the following values:

$$\mu_{L1}^{HV} = -(5.7 + 111.7) \frac{\text{pC}}{\text{m}} = 117.4 \frac{\text{pC}}{\text{m}} \quad (4.24)$$

$$\mu_{L2}^{HV} = (50.5 - 164.8) \frac{\text{pC}}{\text{m}} = -114.3 \frac{\text{pC}}{\text{m}}, \quad (4.25)$$

with $\mu_{L1}^{HV} = \mu_{11}$ and $\mu_{L2}^{HV} = \mu_{12} + 2\mu_{44}$ expressed by the constants used here. The first entry above is the lattice part of the polarization, while the second entry the electronic part. The lattice or relaxed-ion contribution, which corresponds to the term of primary polarization, is in that description the minor part. μ_{L1} and μ_{L2} are re-computed with the values of μ_{12} , μ_{11} and μ_{44} determined in this chapter:

$$\mu_{L1} = \mu_{11} = -(2.4 - 11) \frac{\text{pC}}{\text{m}} = 8.6 \frac{\text{pC}}{\text{m}} \quad (4.26)$$

$$\mu_{L2} = -(22.4 + 22.2) \frac{\text{pC}}{\text{m}} = -44.6 \frac{\text{pC}}{\text{m}}. \quad (4.27)$$

In total μ_{L1}^{HV} and μ_{L2}^{HV} are 1-2 order bigger than the above results of μ_{L1} and μ_{L2} . Generally, it is difficult to compare values of flexoelectric constants, which have been computed by different methods: Here, for the first time from MD simulations and HV by executing ab-initio calculations. The main reason for the above discrepancy results from the dependence of the lattice part and thus of the total flexoelectric coefficients by the choice of the force pattern for maintaining the stress gradient within the unit cell [37]. In their previous publication [36] HV determined only the electronic part of μ_{11} by summing up the third moments of the charge-density distortions and it takes a different value and also sign as in [37]:

$$\mu_{L1}^{HV, \text{el}} = \mu_{11}^{HV, \text{el}} = -95.6 \frac{\text{pC}}{\text{m}}. \quad (4.28)$$

As mentioned above the transverse part of the flexoelectric tensor μ_T was not determined by HV in [37]. μ_T is written with the constants used here

as $\mu_T = \mu_{12} - \mu_{44}$.

For the chlorides NaCl and KCl, isostructural to MgO, flexoelectric constants have been calculated also with the shell model [54]. They are same in magnitude with the ones here for induced polarization (see Tab. 4.1). The constants for the piezoelectric cubic semiconductors GaAs, GaP and ZnS are larger by about a factor 5 [54]. All these systems are weak flexoelectrics compared with the high dielectric perovskites BaTiO₃ and SrTiO₃ in their cubic phase, where ab-initio calculations [54] and experiments [50, 94] report values between 15 and $10^6 \cdot 10^{-13}$ C/cm. The above flexoelectric constants for periclase and also some values of other cubic systems mentioned in the above paragraph are summarized in Tab. 4.1.

In general, theoretical and experimental values of flexoelectric constants are usually not comparable, since all experiments are done at room temperature, while first-principle calculations and also the MD simulations here are executed at 0 K. In Experiment also surface effects are included, which is here and in the ab-initio studies of HV is not the case.

	MD prim.+induced	Ab-initio		Shell-model	Experiment		
		el.	ld.+el.				
pC/m	Thesis here	HV [36]	HV [37]	Hong [35]	Maranganti [54]	Ma [50]	Zubko[94]
	MgO		SrTiO ₃		NaCl	BaTiO ₃	SrTiO ₃
μ_{L1}	-2.4+11	-95.6	-5.7-111.7				
μ_{L2}	-22.4-22.2		50.5-164.8				
μ_{12}	-2.2-9.0				-1.22	100	-9000
μ_{11}	-2.4+11	-95.6	-5.7-111.7	1380	4.12		4000
μ_{44}	-10.1-6.6				-2.3		3000

Table 4.1: The flexoelectric constants μ_{12} , μ_{11} and μ_{44} for different cubic materials determined by MD (in this thesis), ab-initio calculations and experiment.

Conclusion

The flexoelectric response of an inhomogeneously strained periclase sample by molecular dynamics has been shown. For the three flexoelectric coupling coefficients μ_{12} , μ_{11} and μ_{44} three different deformation modes (a), (b) and (c) have been applied. Both direction of collective dipole orientation and linearity of the material's response, namely primary and induced polarization, have been calculated for the bending and shearing mode and are in agreement with theory. The constant μ_{44} needed a special treatment: After regarding the sample in a rotated coordinate system and executing once again mode (a) it was possible to compute μ_{11} from the new flexoelectric constant $\mu'_{3'3'1'1'}$ by knowledge of the other two constants μ_{12} and μ_{44} . In conclusion, with this simple model, it has been able to determine all three flexoelectric constants μ_{12} , μ_{11} and μ_{44} from MD simulations.

Chapter 5

Conclusion and Outlook

In the present thesis molecular simulations (MD) of oxides were performed. For this purpose existing methods have been developed further and implemented in the simulations package IMD. The long-range interactions, which occur in oxides were handled by the summation technique of Wolf. Unlike the method of EWALD it scales linearly with the number of particles and no periodic boundary conditions are needed any more, since the reciprocal space term is omitted. Especially for systems with a large number of atoms a significant speed up in computing time is achieved.

The charge transfer model of Streitz and Mintmire (SM) introduces variable valencies for the atoms, which are determined during MD by minimizing the electrostatic energy. Contrary to the original approach, for solving the corresponding linear system of equations the iterative conjugate gradient (CG) method was executed, while for the long-range terms the Wolf summation instead of EWALD was applied. Also for the computation of the charge values the computing time is by the factor 60 less, by differing only about 1.2%.

The charge optimization is connected to MD by a non-electrostatic force field. For the aluminium-alumina (Al-Al₂O₃) system SM proposed an EAM potential. By performing tensile tests on pure alumina with this potential, including charge computation the resulting stress-strain behavior is in good agreement with ab-initio data, especially for high stresses. However, the surface relaxation of bulk Al₂O₃ provided inadequate results for crack propagation. Also the simulation of the Al-Al₂O₃-interface structure failed with this potential. A different approach was used to get the Al(111)-Al₂O₃(0001) system stable by introducing three different potentials for the interactions of the three atom types (metal Al, oxide Al, O). The resulting potential stabilizes the combined system, but it does not describe the relaxed interface structures (Al-top, O-top, hollow) correctly.

A different description of oxides in the simulation has been introduced

by TS and presented also in this work. In this model the oxygen atoms are polarizable and therefore exhibit a dipole moment. Studying the crack propagation in AlO was possible and successful.

By combining both models of Tangney and Scandolo (TS) and SM the same cracks in AlO could be simulated with variable charges. In contrast to methods like COMB or ReaxFF it is of two orders of magnitude faster.

As a result of visualizing the cracks in alumina an orientated alignment of the dipole moments could be observed. Such a flexoelectric behavior was reproduced for the simple cubic system of periclase (MgO) by applying three different kinds of deformations. The applied deformation was kept by fixing the surface. After a long relaxation time a global primary and induced polarization occur. In that way all three flexoelectric constants of the system were determined. However, the third one has been extracted from the other two after the sample has firstly been regarded in a new coordinate system, which is $\pi/4$ -rotated compared to the older one.

Appendix A

The Software Package IMD

IMD stands for ITAP Molecular Dynamics with ITAP being the shortcut of the Institute of Theoretical and Applied Physics at the University of Stuttgart [75]. It is a powerful tool for the simulation of different interactions between the atoms, like a simple pairwise one or in the case of metals of an EAM potential (see Sec. 2.2). Also many-body potentials are implemented, e.g. the one of Tersoff [83] for covalent materials or the force field proposed by Stillinger-Weber [77]. IMD provides a wide range of simulation options. Beginning from the usual integrators for the thermodynamic ensembles, different relaxators and shear options exist. The latter ones can be used for deforming the sample during the simulation. Additionally, the laser ablation of metals can be simulated. Therefore, a hybrid model has been implemented in IMD, the so-called *Two-Temperature Model* (TTM) [3]. Laser ablation simulations of about 60 million atoms have been carried out with it [73]. Large numbers of particles can be handled by IMD without any problems, since it is parallelized applying the *Message Passing Interface* (MPI). In this context IMD won a prize and holds a world record [66].

Recently, the models of TS and SM have been successfully implemented in IMD. In the first one, the oxygen atoms have an additional property, namely the polarizability, while in the charge transfer model of SM the atomic charge is not a fixed value anymore, but is determined by minimizing the electrostatic energy (see Sec. 2.3.2) [78, 81]. Two different implementations of the minimization process have been realized as already mentioned in Sec. 3.1.2. In one of them the electronegativity χ_i and the interaction matrix \tilde{V}_{ij} are built up by neighbor lists. For the long-range term $1/r_{ij}$ within the SM model both the EWALD and the Wolf summation technique have been used.

Appendix B

Interactions Integrals

In the model of SM in Sec. 2.3.2 the electronegativity of an atom is determined by the terms of nuclear attraction and COULOMB repulsion. The interaction matrix in Eq. (2.49) is also described completely by the repulsive potential $[f_i|f_j]$. A detail and rich examination of all kind of such interaction integrals and their solutions is given in the article of Roothaan [65]. For the SLATER $1s$ -orbitals used in this work the correspond potentials take the form:

$$[j|f_i] = \frac{1}{r_{ij}} \left[1 - (1 + \zeta_i r_{ij}) e^{-2\zeta_i r_{ij}} \right], \quad (\text{B.1})$$

and

$$[f_i|f_j] = \begin{cases} \frac{1}{r_{ij}} \left\{ 1 - (1 - \tau)^2 \frac{1}{4} [2 + \tau + \zeta_i r_{ij}] e^{-2\zeta_i r_{ij}} \right. \\ \quad \left. - (1 + \tau)^2 \frac{1}{4} [2 - \tau + \zeta_i r_{ij}] e^{-2\zeta_i r_{ij}} \right\}, & \zeta_i \neq \zeta_j \\ \frac{1}{r_{ij}} \left\{ 1 - \left[1 + \frac{11}{8} (\zeta_i r_{ij}) + \frac{3}{4} (\zeta_i r_{ij})^2 + \frac{1}{6} (\zeta_i r_{ij})^3 \right] \right. \\ \quad \left. \times e^{-2\zeta_i r_{ij}} \right\}, & \zeta_i = \zeta_j, \end{cases} \quad (\text{B.2})$$

where τ is defined as

$$\tau = \frac{\zeta_i^2 + \zeta_j^2}{\zeta_i^2 - \zeta_j^2}. \quad (\text{B.3})$$

Since $[f_i|f_j] = [f_j|f_i]$ the COULOMB repulsive potential is symmetric. In contrast, $[j|f_i]$ depends only on the type of atom i , so that $[j|f_i] \neq [i|f_j]$ for $\zeta_i \neq \zeta_j$.

Appendix C

Transformation of the Flexoelectric Tensor

The relation between two orthonormal basis is given by following expression:

$$e'_{i'} = e_i R_{ii'}, \quad (\text{C.1})$$

with $R_{ii'}$ being the transformation matrix, while the prime indicates the transformed coordinate. Analogous, the components of the position vector x_i and of any vector can be written as

$$x'_{i'} = x_i R_{ii'} \quad \text{and} \quad x_i = R_{ii'} x'_{i'}, \quad (\text{C.2})$$

in case of the reverse transformation. Using the last equation the derivatives transform in a similar way:

$$\frac{\partial}{\partial x'_{i'}} = \frac{\partial x_i}{\partial x'_{i'}} \frac{\partial}{\partial x_i} = \frac{\partial}{\partial x_i} R_{ii'}. \quad (\text{C.3})$$

The primed version of the polarization from Eq. (4.3):

$$P'_{i'} = \mu'_{i'j'k'l'} \frac{\partial}{\partial x'_{k'}} \frac{\partial}{\partial x'_{l'}} u'_{j'}, \quad (\text{C.4})$$

can be expressed with Eqs. (C.2) and (C.3) as

$$\begin{aligned} P_i R_{ii'} &= \mu'_{i'j'k'l'} R_{kk'} \frac{\partial}{\partial x_k} R_{ll'} \frac{\partial}{\partial x_l} u_j R_{jj'} \mid \times R_{mi'} \\ P_i R_{ii'} R_{mi'} &= R_{mi'} R_{jj'} R_{kk'} R_{ll'} \mu'_{i'j'k'l'} u_{j,kl}. \end{aligned} \quad (\text{C.5})$$

By shifting the index $m \rightarrow i$ above equation takes the form:

$$P_i = \mu_{ijkl} u_{j,kl}, \quad (\text{C.6})$$

with

$$\mu_{ijkl} = R_{ii'}R_{jj'}R_{kk'}R_{ll'}\mu'_{i'j'k'l'}, \quad (\text{C.7})$$

or back transformed:

$$\mu'_{i'j'k'l'} = \mu_{ijkl}R_{ii'}R_{jj'}R_{kk'}R_{ll'}. \quad (\text{C.8})$$

For the deformation in the rotated coordinate system:

$$u'_{z'} = k \frac{x'^2}{2}, \quad (\text{C.9})$$

the resulting polarization as already mentioned in Sec. 4.2 points along the z' -direction:

$$P'_{3'} = \mu'_{3'3'1'1'}k. \quad (\text{C.10})$$

$\mu'_{3'3'1'1'}$ can be expressed with Eq. (C.8) as a sum of the non-primed components of the flexoelectric tensor:

$$\begin{aligned} \mu'_{3'3'1'1'} &= \mu_{ijkl}R_{i3'}R_{j3'}R_{k1'}R_{l1'} \\ &= \mu_{1111}R_{13'}R_{13'}R_{11'}R_{11'} + \mu_{3333}R_{33'}R_{33'}R_{31'}R_{31'} \\ &\quad + \mu_{1133}R_{13'}R_{13'}R_{31'}R_{31'} + \mu_{3311}R_{33'}R_{33'}R_{11'}R_{11'} \\ &\quad + \mu_{1313}R_{13'}R_{33'}R_{11'}R_{31'} + \mu_{3131}R_{33'}R_{13'}R_{31'}R_{11'} \\ &\quad + \mu_{1331}R_{13'}R_{33'}R_{31'}R_{31'} + \mu_{3113}R_{33'}R_{13'}R_{11'}R_{11'}, \end{aligned} \quad (\text{C.11})$$

where Eq. (4.4) has been applied:

$$\mu_{ijkl} = (\mu_{11} - \mu_{12} - 2\mu_{44})\delta_{ijkl} + \mu_{12}\delta_{ij}\delta_{kl} + \mu_{44}(\delta_{ik}\delta_{jl} + \delta_{il}\delta_{jk}). \quad (\text{C.12})$$

Finally, with the rotation matrix from Eq. (4.16):

$$\mathbf{R} = \begin{pmatrix} 1/\sqrt{2} & 0 & 1/\sqrt{2} \\ 0 & 1 & 0 \\ -1/\sqrt{2} & 0 & 1/\sqrt{2} \end{pmatrix}, \quad (\text{C.13})$$

$\mu'_{3'3'1'1'}$ reduces to Eq. (4.20):

$$\mu'_{3'3'1'1'} = \frac{1}{2} \left\{ \mu_{11} + \mu_{12} - 2\mu_{44} \right\}. \quad (\text{C.14})$$

Bibliography

- [1] Albe, K., Nord, J., and Nordlund, K.: Dynamic charge-transfer bond-order potential for gallium nitride. *Philosophical Magazine*, **89** (34-36), 3477–3497, 2009.
- [2] Allen, M. and Tildesley, D.: *Computer Simulation of Liquids* (Oxford Science Publications, 1987).
- [3] Anisimov, S. I., Kapeliovich, B. L., and Perel'man, T. L.: Electron emission from metal surfaces exposed to ultra short laser pulses. *JETP Lett.*, **39** (2), 1974.
- [4] Askar, A., Lee, P. C. Y., and Cakmak, A. S.: Lattice-dynamics approach to the theory of elastic dielectrics with polarization gradient. *Phys. Rev. B*, **1**, 3525–3537, 1970.
- [5] Baskaran, S. and He, X.: Strain gradient induced electric polarization in α -phase polyvinylidene fluoride films under bending conditions. *J. Appl. Phys.*, **111**, 014109, 2012.
- [6] Beck, P., Brommer, P., Roth, J., and Trebin, H.-R.: Ab initio based polarizable force field generation and application to liquid silica and magnesia. *J. Chem. Phys.*, **135**, 234512, 2011.
- [7] Beck, P., Brommer, P., Roth, J., and Trebin, H.-R.: Influence of polarizability on metal oxide properties studied by molecular dynamics simulations. *J. Phys.: Condens. Matter*, **24**, 485401, 2012.
- [8] Brommer, P., Beck, P., Chatzopoulos, A., Gähler, F., Roth, J., and Trebin, H.-R.: Direct wolf summation of a polarizable force field for silica. *J. Chem. Phys.*, **132**, 194109, 2010.
- [9] Brommer, P. and Gähler, F.: Potfit: effective potentials from ab-initio data. *Model. Simul. Mater. Sci. Eng.*, **15** (3), 295–304, 2007.

-
- [10] Bursian, E. V. and Trunov, N. N.: Nonlocal piezoelectric effect. *Sov. Phys. – Solid State*, **16**, 760, 1974.
- [11] Catalan, G., Noheda, B., McAneney, J., Sinnamón, L. J., and Gregg, J. M.: Strain gradients in epitaxial ferroelectrics. *Phys. Rev. B*, **72**, 020102, 2005.
- [12] Catalan, G., Sinnamón, L. J., and Gregg, J. M.: The effect of flexoelectricity on the dielectric properties of inhomogeneously strained ferroelectric thin films. *Journal of Physics: Condensed Matter*, **16** (13), 2253, 2004.
- [13] Chenoweth, K., van Duin, A. C., and Goddard, W. A.: Reaxff reactive force field for molecular dynamics simulations of hydrocarbon oxidation. *The Journal of Physical Chemistry A*, **112** (5), 1040–1053, 2008.
- [14] Coey, J., Ariando, n., and Pickett, W.: Magnetism at the edge: New phenomena at oxide interfaces. *MRS Bulletin*, **38**, 1040–1047, 2013.
- [15] Cross, L. E.: Flexoelectric effects: Charge separation in insulating solids subjected to elastic strain gradients. *J. Mater. Sci.*, **41**, 53, 2006.
- [16] Curie, J. and Curie, P.: Development, via compression, of electric polarization in hemihedral crystals with inclined faces. *Bulletin de la Société minéralogique de France*, **3**, 90–93, 1880.
- [17] Curie, J. and Curie, P.: Contractions and expansions produced by voltages in hemihedral crystals with inclined faces. *Comptes Rendus*, **93**, 1137–1140, 1881.
- [18] Daw, M. S. and Baskes, M. I.: Semiempirical, quantum mechanical calculation of hydrogen embrittlement in metals. *Phys. Rev. Lett.*, **50**, 1285–1288, 1983.
- [19] Daw, M. S. and Baskes, M. I.: Embedded-atom method: Derivation and application to impurities, surfaces, and other defects in metals. *Phys. Rev. B*, **29**, 6443–6453, 1984.

- [20] Daw, M. S., Foiles, S. M., and Baskes, M. I.: The embedded-atom method: a review of theory and applications. *Materials Science Reports*, **9** (7-8), 251 – 310, 1993.
- [21] Devine, B., Shan, T.-R., Cheng, Y.-T., McGaughey, A. J. H., Lee, M., Phillpot, S. R., and Sinnott, S. B.: Atomistic simulations of copper oxidation and Cu/Cu₂O interfaces using charge-optimized many-body potentials. *Physical Review B*, **84** (12), 125308, 2011.
- [22] Elsener, A.: *An atomistic simulation method for oxygen impurities in aluminium based on variable charge molecular dynamics*. Ph.D. thesis, Ecole Polytechnique Fédérale, Lausanne, 2010.
- [23] Elsener, A., Politano, O., Derlet, P. M., and Van Swygenhoven, H.: A local chemical potential approach within the variable charge method formalism. *Modelling and Simulation in Materials Science and Engineering*, **16** (2), 025006, 2008.
- [24] Ercolessi, F. and Adams, J. B.: Interatomic Potentials from First-Principles Calculations: The Force-Matching Method. *EPL (Europhysics Letters)*, **26**, 583–588, 1994.
- [25] Ewald, P. P.: Die Berechnung optischer und elektrostatischer Gitterpotentiale. *Ann. Phys. (Leipzig)*, **64**, 253–287, 1921.
- [26] Finnis, M. W. and Sinclair, J. E.: A simple empirical n-body potential for transition metals. *Philosophical Magazine A*, **50** (1), 45–55, 1984.
- [27] Foiles, S. M., Baskes, M. I., and Daw, M. S.: Embedded-atom-method functions for the fcc metals Cu, Ag, Au, Ni, Pd, Pt, and their alloys. *Phys. Rev. B*, **33**, 7983–7991, 1986.
- [28] Gaetani, G. A., Asimow, P. D., and Stolper, E. M.: Determination of the partial molar volume of SiO₂ in silicate liquids at elevated pressures and temperatures: A new experimental approach. *Geochim. Cosmochim. Acta*, **62**, 2499, 1998.
- [29] Granozio, F. M., Koster, G., and Rijnders, G.: Functional oxide interfaces. *MRS Bulletin*, **38**, 1017–1023, 2013.
- [30] Gregg, J. M.: Stressing ferroelectrics. *Science*, **336**, 41, 2012.

- [31] Grottel, S., Beck, P., Müller, C., Reina, G., Roth, J., Trebin, H.-R., and Ertl, T.: Visualization of electrostatic dipoles in molecular dynamics of metal oxides. *IEEE Trans. Vis. Comp. Graph.*, **18** (12), 2061, 2012.
- [32] Grottel, S., Reina, G., and Ertl, T.: Megamol: A visualization middleware of point-based molecular data sets, 2012. <http://www.visus.uni-stuttgart.de/megamol/>.
- [33] Herzbach, D., Binder, K., and Muser, M. H.: Comparison of model potentials for molecular-dynamics simulations of silica. *J. Chem. Phys.*, **123** (12), 124711, 2005.
- [34] Hocker, S., Beck, P., Roth, J., Schmauder, S., and Trebin, H.-R.: Simulation of crack propagation in alumina with ab initio based polarizable force field. *J. Chem. Phys.*, **136**, 084707, 2012.
- [35] Hong, J., Catalan, G., Scott, J. F., and Artacho, E.: The flexoelectricity of barium and strontium titanates from first principles. *J. Phys. Cond. Mat.*, **22**, 112201, 2010.
- [36] Hong, J. and Vanderbilt, D.: First-principles theory of frozen-ion flexoelectricity. *Phys. Rev. B*, **84**, 180101, 2011.
- [37] Hong, J. and Vanderbilt, D.: First-principles theory and calculation of flexoelectricity. *Phys. Rev. B*, **88**, 174107, 2013.
- [38] Indenbom, V. L., Loginov, E. B., and Osipov, M. A.: The flexoelectric effect and the structure of crystals. *Kristallografiya*, **26**, 1157, 1981.
- [39] Jr., M. F. R., Li, R., Mench, M., and van Duin, A. C.: Molecular dynamic simulation of aluminum-water reactions using the reaxff reactive force field. *International Journal of Hydrogen Energy*, **36** (10), 5828 – 5835, 2011.
- [40] Kittel, C.: *Einführung in die Festkörperphysik* (Oldenbourg, 2006).
- [41] Kogan, S. M.: Piezoelectric effect during inhomogeneous deformation and acoustic scattering of carriers in crystals. *Sov. Phys. Solid State*, **5**, 2069, 1964.

- [42] Kolafa, J. and Perram, J. W.: Cutoff errors in the ewald summation formulae for point charge systems. *Molecular Simulation*, **9** (5), 351–368, 1992.
- [43] Kresse, G. and Furthmüller, J.: Efficiency of ab-initio total energy calculations for metals and semiconductors using a plane-wave basis set. *Computational Materials Science*, **6** (1), 15 – 50, 1996.
- [44] Kresse, G. and Furthmüller, J.: Efficient iterative schemes for ab initio total-energy calculations using a plane-wave basis set. *Phys. Rev. B*, **54**, 11169–11186, 1996.
- [45] Kresse, G. and Hafner, J.: Ab initio molecular dynamics for liquid metals. *Phys. Rev. B*, **47** (1), 558, 1993.
- [46] Kresse, G. and Hafner, J.: Ab initio molecular-dynamics simulation of the liquid-metal-amorphous-semiconductor transition in germanium. *Phys. Rev. B*, **49**, 14251–14269, 1994.
- [47] Lee, D., Yoon, A., Jang, S. Y., Yoon, J.-G., Chung, J.-S., Kim, M., Scott, J. F., and Noh, T. W.: Giant flexoelectric effect in ferroelectric epitaxial thin films. *Phys. Rev. Lett.*, **107**, 057602, 2011.
- [48] Liang, T., Shin, Y. K., Cheng, Y.-T., Yilmaz, D. E., Vishnu, K. G., Verners, O., Zou, C., Phillpot, S. R., Sinnott, S. B., and van Duin, A. C.: Reactive potentials for advanced atomistic simulations. *Annual Review of Materials Research*, **43** (1), 109–129, 2013.
- [49] Lu, H., Bark, C.-W., Esque de los Ojos, D., Alcalá, J., Eom, C. B., Catalan, G., and Gruverman, A.: Mechanical writing of ferroelectric polarization. *Science*, **336** (6077), 59–61, 2012.
- [50] Ma, W. and Cross, L. E.: Flexoelectricity of barium titanate. *Appl. Phys. Lett.*, **88**, 232902, 2006.
- [51] Majdoub, M. S., Sharma, P., and Cagin, T.: Dramatic enhancement in energy harvesting for a narrow range of dimensions in piezoelectric nanostructures. *Phys. Rev. B*, **78**, 121407, 2008.
- [52] Majdoub, M. S., Sharma, P., and Cagin, T.: Enhanced size-dependent piezoelectricity and elasticity in nanostructures due to the flexoelectric effect. *Phys. Rev. B*, **77**, 125424, 2008.

-
- [53] Maranganti, R., Sharma, N. D., and Sharma, P.: Electromechanical coupling in nonpiezoelectric materials due to nanoscale nonlocal size effects: Green's function solutions and embedded inclusions. *Phys. Rev. B*, **74**, 014110, 2006.
- [54] Maranganti, R. and Sharma, P.: Atomistic determination of flexoelectric properties of crystalline dielectrics. *Phys. Rev. B*, **80**, 054109, 2009.
- [55] Mashkevich, V. S. and Tolpygo, K. B.: *Sov. Phys. JETP*, **5**, 435, 1957.
- [56] Meister, A.: *Numerik linearer Gleichungssysteme* (Vieweg, 2008).
- [57] Mishin, Y., Farkas, D., Mehl, M. J., and Papaconstantopoulos, D. A.: Interatomic potentials for monoatomic metals from experimental data and *ab initio* calculations. *Phys. Rev. B*, **59**, 3393–3407, 1999.
- [58] Nosé, S.: A unified formulation of the constant temperature molecular dynamics methods. *J. Chem. Phys.*, **81** (November 1983), 511–519, 1984.
- [59] Nosé, S.: A molecular dynamics method for simulations in the canonical ensemble. *Molecular Physics*, **100** (1), 191–198, 2002.
- [60] Plimpton, S.: Fast parallel algorithms for short-range molecular dynamics. *Journal of Computational Physics*, **117** (1), 1 – 19, 1995.
- [61] Press, W. H., Teukolsky, S. A., Vetterling, W. T., and Flannery, B. P.: *Numerical Recipes in C: The Art of Scientific Computing* (Academic Press, Cambridge, 2007), 3. edition.
- [62] Quang, H. L. and He, Q.-C.: The number and types of all possible rotational symmetries for flexoelectric tensors. *Proc. R. Soc. London, Ser. A*, **467**, 2369, 2011.
- [63] Rappe, A. K. and Goddard, W. A.: Charge equilibration for molecular dynamics simulations. *The Journal of Physical Chemistry*, **95** (8), 3358–3363, 1991.
- [64] Resta, R.: Towards a bulk theory of flexoelectricity. *Phys. Rev. Lett.*, **105**, 127601, 2010.

- [65] Roothaan, C. C. J.: A study of two-center integrals useful in calculations on molecular structure. i. *The Journal of Chemical Physics*, **19** (12), 1445–1458, 1951.
- [66] Roth, J., Gähler, F., and Trebin, H.-R.: A molecular dynamics run with 5.180.116.000 particles. *Int. J. Mod. Phys. C.*, **11**, 317, 2000.
- [67] Sakurai, J. J.: *Modern Quantum Mechanics* (Addison Wesley Longman, 1994).
- [68] Shan, T.-R., Devine, B. D., Hawkins, J. M., Asthagiri, A., Phillpot, S. R., and Sinnott, S. B.: Second-generation charge-optimized many-body potential for Si/SiO₂ and amorphous silica. *Physical Review B*, **82** (23), 235302, 2010.
- [69] Shan, T.-R., Devine, B. D., Phillpot, S. R., and Sinnott, S. B.: Molecular dynamics study of the adhesion of Cu/SiO₂ interfaces using a variable-charge interatomic potential. *Physical Review B*, **83** (11), 115327, 2011.
- [70] Shewchuk, J. R.: An introduction to the conjugate gradient method without the agonizing pain, 1994.
- [71] Shin, Y. K., Shan, T.-R., Liang, T., Noordhoek, M. J., Sinnott, S. B., van Duin, A. C., and Phillpot, S. R.: Variable charge many-body interatomic potentials. *MRS Bulletin*, **37**, 504–512, 2012.
- [72] Shu, L., Wei, X., Yao, X., and Wang, C.: Symmetry of flexoelectric coefficients in crystalline medium. *J. Appl. Phys.*, **110**, 104106, 2011.
- [73] Sonntag, S., Trichet, C., Roth, J., and Trebin, H.-R.: Molecular Dynamics Simulations of Cluster Distribution from Femtosecond Laser Ablation in Aluminum. *submitted*, 2010.
- [74] Spaldin, N. A. and Ramesh, R.: Electric-field control of magnetism in complex oxide thin films. *MRS Bulletin*, **33**, 1047–1050, 2008.
- [75] Stadler, J., Mikulla, R., and Trebin, H.-R.: IMD: a software package for molecular dynamics studies on parallel computers. *Int. J. Mod. Phys. C.*, **8** (5), 1131–1140, 1997.

- [76] Stemmer, S. and Millis, A. J.: Quantum confinement in oxide quantum wells. *MRS Bulletin*, **38**, 1032–1039, 2013.
- [77] Stillinger, F. H. and Weber, T. A.: Computer simulation of local order in condensed phases of silicon. *Physical Review B*, **31** (8), 5262–5271, 1985.
- [78] Streitzi, F. H. and Mintmire, J. W.: Electrostatic potentials for metal-oxide surfaces and interfaces. *Phys. Rev. B*, **50** (16), 11996–12003, 1994.
- [79] Tagantsev, A. K.: Piezoelectricity and flexoelectricity in crystalline dielectrics. *Phys. Rev. B*, **34** (8), 5883, 1986.
- [80] Tagantsev, A. K. and Yurkov, A. S.: Flexoelectric effect in finite samples. *J. Appl. Phys.*, **112** (4), 044103, 2012.
- [81] Tangney, P. and Scandolo, S.: An ab initio parametrized interatomic force field for silica. *J. Chem. Phys.*, **117** (19), 8898–8904, 2002.
- [82] Tebano, A., Fabbri, E., Pergolesi, D., Balestrino, G., and Traversa, E.: Room-temperature giant persistent photoconductivity in srtio3/laalo3 heterostructures. *ACS Nano*, **6** (2), 1278–1283, 2012.
- [83] Tersoff, J.: Modeling solid-state chemistry: Interatomic potentials for multicomponent systems. *Physical Review B*, **39** (8), 5566–5568, 1989.
- [84] Trave, A., Tangney, P., Scandolo, S., Pasquarello, A., and Car, R.: Pressure-induced structural changes in liquid SiO₂ from ab initio simulations. *Phys. Rev. Lett.*, **89**, 245504, 2002.
- [85] van Beest, B. W. H., Kramer, G. J., and van Santen, R. A.: Force fields for silicas and aluminophosphates based on ab initio calculations. *Phys. Rev. Lett.*, **64** (16), 1955–1958, 1990.
- [86] van Duin, A. C. T., Dasgupta, S., Lorant, F., and Goddard, W. A.: Reaxff: A reactive force field for hydrocarbons. *The Journal of Physical Chemistry A*, **105** (41), 9396–9409, 2001.
- [87] Wang, J., Neaton, J. B., Zheng, H., Nagarajan, V., Ogale, S. B., Liu, B., Viehland, D., Vaithyanathan, V., Schlom, D. G., Waghmare, U. V., Spaldin, N. A., Rabe, K. M., Wuttig, M., and Ramesh, R.: Epitaxial

- bifeo3 multiferroic thin film heterostructures. *Science*, **299** (5613), 1719–1722, 2003.
- [88] Wolf, D., Keblinski, P., Phillpot, S. R., and Eggebrecht, J.: Exact method for the simulation of Coulombic systems by spherically truncated, pairwise $1/r$ summation. *J. Chem. Phys.*, **110** (17), 8254–8282, 1999.
- [89] Yasukawa, A.: Using an extended tersoff interatomic potential to analyze the static-fatigue strength of SiO_2 under atmospheric influence. *JSME Int. J. A*, **39**, 313–320, 1996.
- [90] Yu, J., Sinnott, S. B., and Phillpot, S. R.: Charge optimized many-body potential for the si/sio₂ system. *Phys. Rev. B*, **75**, 085311, 2007.
- [91] Zhou, X. W. and Doty, F. P.: Embedded-ion method: An analytical energy-conserving charge-transfer interatomic potential and its application to the La-Br system. *Phys. Rev. B*, **78**, 224307, 2008.
- [92] Zhou, X. W., Wadley, H. N. G., Filhol, J.-S., and Neurock, M. N.: Modified charge transfer-embedded atom method potential for metal/metal oxide systems. *Phys. Rev. B*, **69**, 035402, 2004.
- [93] Zhu, W., Fu, J. Y., Li, N., and Cross, L.: Piezoelectric composite based on the enhanced flexoelectric effects. *Applied Physics Letters*, **89** (19), 192904, 2006.
- [94] Zubko, P., Catalan, G., Buckley, A., Welche, P. R. L., and Scott, J. F.: Strain-gradient-induced polarization in SrTiO_3 single crystals. *Phys. Rev. Lett.*, **99**, 167601, 2007.

List of Publications

- [95] Chatzopoulos, A., and Trebin, H.-R.: Hydrodynamic structure factor of quasicrystals. *Phys. Rev. B*, **81**, 064205, 2010.
- [96] Brommer, P., Beck, P., Chatzopoulos, A., Gähler, F., Roth, J., and Trebin, H.-R.: Direct wolf summation of a polarizable force field for silica. *J. Chem. Phys.*, **132**, 194109, 2010.
- [97] Chatzopoulos, A., Ishii, Y., and Trebin, H.-R.: Hydrodynamic structure factor for two-dimensional decagonal quasicrystals. *Phys. Status Solidi B*, **250**, 291-304, 2013.
- [98] Roth, J., Beck, P., Brommer, P., Chatzopoulos, A., Gähler, F., Hocker, S., Schmauder, S., and Trebin, H.-R.: Molecular dynamics simulations with long-range interactions. *High Performance Computing in Science and Engineering '13*, eds. Nagel, W. E., Kröner, D. B., Resch, M. M., Springer, Heidelberg, 2013

Danksagung

An erster Stelle möchte ich mich besonders bei Prof. Dr. Hans-Rainer Trebin bedanken, der mir noch vor Beendigung der Diplomarbeit, die luxuriöse Doktorandenstelle im SFB 716 anbot, mir immer helfend zur Seite stand und auch in schwierigen Zeiten Verständnis gezeigt hat. Die Bezeichnung *Doktorvater* trifft hier voll und ganz zu.

Prof. Dr. Christian Holm danke ich für die freundliche Übernahme des Mitberichts und Prof. Dr. Jörg Wrachtrup dafür, dass er sich bereit erklärt hat den Prüfungsvorsitz zu übernehmen.

PD Dr. Johannes Roth war erste Anlaufstation für technische Probleme jeder Art. Ein Danke deshalb an ihm für seine Hilfe in all den Jahren, aber auch für die interessanten Gespräche auf Dienstreisen.

Mein Dank geht besonders an Dr. Andreas Elsener, der den weiten Weg aus Zürich auf sich nahm, um am Anfang der Arbeit seine Erfahrung und sein Wissen auf dem Gebiet der Simulation von Metalloxiden an mich und damit auch an die gesamten Gruppe weiterzugeben.

Den Mitarbeitern des ITAPs, mit denen ich während der Promotion zusammen gearbeitet habe, vorwiegend bei der Betreuung von Übungen, danke ich für ihre nette und hilfsbereite Art.

Die Zuvorkommenheit des Sekretariats, bestehend aus Ulrike Mergenthaler, Marietta Köstler und Simone Blümlein bereichert das ITAP und hat es entscheidend geprägt. Ein Danke an die Damen für die netten Unterhaltungen während der Kaffeerrunde.

Dr. Steffen Sonntag war während seiner ITAP-Zeit mein Mentor und ist auch heute noch mein alltäglicher Gesprächspartner. Ich danke ihm für seine Hilfe in den vergangenen Jahren, die mittlerweile legendären Nachsit-

zungen im Zimmer 6.346, das Aufrechterhalten der Achse auch längst nach seinem Ausscheiden aus dem ITAP und das Teilen gemeinsamer Interessen.

Mit Thomas Nikolakis hab ich mich in den vergangenen eineinhalb Jahren am liebsten unterhalten. Von den kleinen alltäglichen Sorgen bis hin zu gesellschaftspolitischen Themen wurde alles während er seiner Arbeit im meinem Zimmer nachging oft einfach nur zu kurz diskutiert. Für die daraus entstandene Freundschaft danke ich ihm sehr.

Drei Kinder in der Fremde aufzuziehen, während man in gegensätzlicher Schicht arbeitet, stellt einer der größten Leistungen überhaupt dar. Für ihre aufopfernde und bedingungslose Unterstützung all die Jahre gebührt meinen Eltern ein ganz herzliches Dankeschön. Dieser Dokortitel sei ihnen gewidmet.

Ehrenwörtliche Erklärung

Hiermit erkläre ich, dass ich die vorliegende Arbeit selbständig verfasst und nur die angegebenen Quellen und Hilfsmitteln verwendet habe.

Stuttgart, im Februar 2015

Andreas Chatzopoulos